Exploring B – L Gauge Models at the LHC and Beyond

Wei Liu

A dissertation submitted in partial fulfillment
of the requirements for the degree of
Doctor of Philosophy
of
University College London.

Department of High Energy Physics
University College London

March 5, 2020

I, Wei Liu, confirm that the work presented in this thesis is my own. Where information has been derived from other sources, I confirm that this has been indicated in the work.

Abstract

Although the Standard Model of particle physics is regarded as one of the most successful physical theories, there is strong evidence indicating the existence of physics beyond the Standard Model. This includes the dark matter and dark energy problems, the matter and antimatter asymmetry problem, and the observation of neutrino mixing and masses. In this thesis, we study some of the consequence of one example of a beyond the Standard Model theory. Namely, we discuss a model based on a spontaneously broken $B-L$ gauge symmetry. It can explain the light neutrino masses via a Type-I seesaw mechanism with heavy neutrinos. The model predicts processes which can make additional contributions to the Large Hadron Collider (LHC) measurements such as the Higgs signal strengths, and contains processes with exotic particles which can lead to multi-lepton final states in LHC searches. Besides, from the limits on the light neutrinos masses due to double beta decay experiments and cosmological observations together with the seesaw relation, the heavy neutrinos present in the model are likely to be weakly mixed to the light neutrinos thus leading to potential displaced vertex signals at the LHC. We summarise the existing limits on the model parameters, and perform three studies using LHC measurement results, the recasting of the prompt lepton final states searches and displaced vertex searches to explore the model further. These studies are able to show competitive or even better sensitivities to the current limits for certain regions of the parameter space. For example, displaced vertex searches can reach active-sterile mixing strengths of order $V_{\mu N} \approx 10^{-6}$, compatible with light neutrino mass generation through the seesaw mechanism for heavy neutrinos with masses around $1-100$ GeV.

Impact Statement

This thesis analyzes the $B-L$ gauge model and the heavy neutrino inside it. We have introduced three studies to probe all of the parameters of the model. We show that this can improve the current limits under certain scenarios. We have demonstrated that the tool called `CONTUR` [1] can be used to study the Beyond the Standard Model (BSM) using the LHC measurements, thus exploit the data of these measurements. This, as an example, encourages more work to be done using this tool. Recasting of prompt final states is an alternative way to interpret LHC searches. As we do not understand the new physics BSM, different possibilities need to be explored. Displaced vertices have raised a lot of attention in the particle physics community, so we have explored their potential to look for heavy neutrinos at several proposed detectors as well as the LHC. The results show that the sensitivity of these detectors can improve the current limits by an order of magnitude. This is helpful for the experimental community to evaluate the physics potential of their proposed detector, and even improve their designs. For the theoretical community, we present an example to show what new physics can be reached or even discovered after the construction of these new facilities. It can inspire the search for other particles, as they can lead to signatures of displaced vertices as well. At Run 3 of the LHC, one of these detectors, FASER, is already decided to be built. Moreover, we developed and updated a `FeynRules` [2] model file and its `UFO` [3] output for the $B-L$ gauge model, which enables other scholars to use it to study any tree level processes they want. Outside academia, this research involves people from different countries, and I am supported by Chinese Scholarship Council, thus enhancing the international collaboration, and the communications between them.

Acknowledgements

First of all, let me express my greatest gratitude to my supervisor Prof. Frank Deppisch, who gave me the opportunity to be a part of this research. With his expert guidance and horizon, this thesis became possible. His patience and carefulness helped me to write this thesis. In addition, I would like to thank Professor Jon Butterworth, Dr. Suchita Kulkarni and Dr. Manimala Mitra for becoming such great collaborators who made the research much easier for me.

Also, thanks to all my colleagues and friends at University College London, who gave me a friendly environment where to work and live. Especially to Dr. Lukas Graf who helped me get through the first year, Dr. David Yallup who helped me a lot at learning coding and Fang Xie for letting me meet my fiancée Xin Gao. To Lifeng Ye and Ming Zhang for the friendships and companion all along.

I would also like to acknowledge the support from my parents, Renzhi Liu and Xiufen Qu, and my sister, Kailing Liu. Finally, thanks for becoming so lucky to meet my fiancée Xin Gao during my PhD. She gave me the strength and let me see the light of how my life is going to be and makes me a better man. Thanks for being so patient and accompanying me even in such a long distance.

Contents

Chapter 1

Introduction

The Standard Model (SM) of particle physics is regarded as one of the most successful theories in physics. It describes the elementary structure of the universe, explains the fundamental forces from symmetry considerations and introduces how mass is created through the Higgs mechanism. The SM has been tested in numerous experiments and its particle content has now all been discovered, culminating in the discovery of the Higgs boson. Among the experiments, the LHC, started in 2008, has tested the SM at the highest energy frontier, and it is searching for exotic physics beyond it, but no BSM signal has been seen so far.

In spite of this success, the SM still fails to explain several experimental facts. In the SM, neutrinos are regarded as massless fermions and there is no neutrino mixing. Therefore, the observation of light neutrino masses and mixing in neutrino oscillation experiments [4–18] indicates the existence of physics beyond the Standard Model. To explain neutrino masses, the seesaw mechanism [19–21] is regarded as one of the most elegant methods. Many BSM theories can implement the seesaw mechanism with the presence of right-handed (RH) neutrinos. A simple ultraviolet (UV) complete model, the baryon number B minus lepton number L ($B-L$) gauge model [22] is among the minimal choices. In the SM, B and L are conserved separately at the perturbative level, whereas $B+L$ is broken as a quantum anomaly and $B-L$ remains conserved in instanton and sphaleron processes. The $B-L$ model adds an Abelian $U(1)_{B-L}$ factor to the SM gauge group, $SU(3)_C \times SU(2)_L \times U(1)_Y \times U(1)_{B-L}$. It contains three generations of RH neutrinos that are sterile under the SM gauge groups, but have a $B-L$ charge. Their presence not only allows to incorporate the seesaw mechanism, but it also ensures that the model is free from quantum anomalies.

The $U(1)_{B-L}$ part of the gauge group is broken spontaneously via an exotic Higgs singlet χ, giving rise to an exotic heavy Z' gauge boson. These exotic BSM particles can be searched for directly, and in addition they can potentially mix with their SM counterparts, the SM Higgs H and the Z boson, opening up new channels in H and Z decays. A term $\overline{\nu_R^c}\chi\nu_R$ is allowed in the model and after the $B-L$ symmetry breaking, it will generate Majorana neutrino masses. The light neutrino masses are then generated via the seesaw mechanism.

The $B-L$ model has been studied in numerous works both in theory and experiment, see for example [23–44]. The free parameters of the $B-L$ model can be classified into three categories: a gauge sector with the mass of the Z' and the $B-L$ gauge coupling g_{B-L}. Here, and as noted later, we omit the possible kinematic mixing between the SM Z and the $B-L$ Z' as a minimal choice to simplify the model. However, the kinematic mixing will arise in loop level eventually, so hence the no mixing assumption is set at the electroweak scale only; a scalar sector with the mass of the exotic Higgs and the Higgs mixing strength $\sin\alpha$; and a neutrino sector with the heavy neutrino masses m_{N_i} $(i = 1,2,3)$ and their mixing strengths to the light neutrinos V_{lN_i} $(l = e,\mu,\tau)$.

From theoretical considerations, we must ensure that the model is perturbative and consistent. Namely, we require the scalar potential to meet the condition of vacuum stability, the couplings to be perturbative at the electroweak (EW) scale and the additional W boson mass contribution via the radiative effects of the extra exotic Higgs [45,46] to meet the experimental value. We can further demand the model to be a UV complete theory by matching parameters at the EW scale, evolving them according to the renormalisation group equations (RGEs) [40,47], and requiring the model to be perturbative and consistent up to the Planck scale. However, some of these considerations are subject to bias, such as assuming the $B-L$ model is the only BSM physics up to the Planck scale.

The model contains additional particles which can result in final states to which LHC searches for BSM particles are sensitive. Searches for these extra particles from certain final states, and their non-observation set limits on the parameter space. For example, resonance searches for the exotic gauge boson Z' dilepton final states at the Tevatron [41,48–50], LEP-II [51–53], LHC [54–59], and in non-collider experiments [60–70] have been performed. The exotic Higgs has been searched for via direct and indirect searches for extra scalars at the LHC [27, 45, 46, 71–79]. Direct searches for heavy neutrinos also have been carried at the LHC [80–89].

While current limits are mostly derived from dedicated BSM searches, undertaking this for all possible signatures and scenarios is formidable. As there is a large library of SM precision measurements at the LHC, and a BSM model can potentially make additional contributions to many of these, the precision measurement data can be used to constrain the model as well. Recently, a tool called ‘Constraints On New Theories Using Rivet’ (CONTUR) [1], which utilizes precision measurements at the LHC, was developed. It uses model-independent information on particle-level differential measurements in fiducial regions of the phase space. Thus, by comparing the BSM signatures with measurements, we can look for effects of BSM theories.

On the other hand, we can exploit LHC searches and look for special signatures from the $B-L$ model. For example, there are numerous studies at the LHC looking for prompt lepton final states from an exotic gauge boson which could be the Z' in the $B-L$ model (see Ref. [31] and references therein). If not already studied within the $B-L$ model, such limits can be recast into it, e.g. using `Darkcast` [31], assuming standard production of Z' via direct Drell-Yan and decay to two leptons. However, in the $B-L$ model, once the Higgs mixing is large, the exotic gauge boson Z' can potentially be additionally pair-produced via the SM-like Higgs decays, leading to four-lepton final states. Considering such processes, LHC searches for four-lepton final states can yield additional limits on the gauge sector of the model.

The heavy neutrinos in the $B-L$ model can potentially produce distinct signatures as well. The LHC is typically sensitive to heavy neutrinos in a mass range

$1-100$ GeV. As the heavy neutrino masses and sterile-active mixing strengths are constrained by the light neutrino masses in the Type-I seesaw relation $m_\nu \approx V_{lN}^2 m_N$, the mixing is expected to be small, $V_{lN} \approx 10^{-6}$ for heavy neutrinos with $m_N \sim 1-100$ GeV [80–83, 88, 89]. Adding sterile neutrinos to the SM, such a mixing is not testable as the cross section of the main heavy neutrino production process $pp \to W^\pm \to Nl^\pm$ is not sufficient to achieve a significant number of events. However, in the $B-L$ model, the heavy neutrinos are charged under $B-L$ and can be produced via the exotic Higgs, the SM-like Higgs [90] and the exotic Z' [91], independent of the active-sterile mixing. As the heavy neutrinos only decay via the active-sterile mixing, they can have long decay lengths, possibly in the range of centimeters to meters, thus are likely long-lived, leading to distinctive signatures with displaced vertices. Therefore, searches for displaced vertices from heavy neutrinos can yield limits on the neutrino sector of the model.

This thesis is organised in the following way. After this introduction, we first provide a brief overview of the SM and physics beyond the SM in Chapter 2. We introduce the $B-L$ gauge model in Chapter 3, and the LHC, its properties and the potential LHC phenomenology of the model are summarised in Chapter 4. In Chapter 5, we discuss current experimental constraints. Chapter 6 introduces the CONTUR framework and its application to the $B-L$ model. Chapter 7 covers analyses of prompt lepton final state searches to constrain the gauge sector of the model. Our studies of heavy neutrinos from either the SM-like Higgs or the exotic Z' using displaced vertex signatures are discussed in Chapter 8. We give a conclusion and future outlook in the final Chapter 9.

Chapter 2

The Standard Model and Beyond

In this chapter, we will introduce the SM of particles physics. The SM is a major step towards understanding the rules governing the universe, such as the nature of matter in the universe, how the particles interact and how mass is created. We will introduce it following a heuristic way, by answering the questions above. It is, however, not expected to be the final theory, as there are several experimental observations for which it lacks an explanation, thus leaving room for physics beyond the SM.

2.1 The SM as a gauge theory

The final goal of physics is to describe the rules of the universe in the most elegant and unified ways. The first great breakthrough to achieve this was Newtonian physics, which introduces the notion of force or interaction to unify the phenomena on the Earth and in the sky. In the 1950s, the physics community came to realise that there are four fundamental forces governing the physical world, the electromagnetic force, the weak force, the strong force and the gravitational force.

It the meantime, there is a challenge to describe the forces incorporating the breakthrough of quantum mechanics and relativity. Dirac and others proposed Quantum Electrodynamics (QED) to answer this challenge for the electromagnetic force. This theory is the first relativistic quantum field theory, and is also a gauge theory, an Abelian gauge theory with $U(1)_{EM}$ being the gauge group and the photon as the gauge boson to mediate the electromagnetic force.

The weak force is responsible for the radioactive decays of nuclei. The most important phenomenon involving the weak force is beta decay, $n \to p + e^- + \bar{\nu}_e$. The first theory to describe this process was proposed by Fermi [92] with an assumption of a simple contact interaction of 4 fermions,

$$\mathscr{L}_{Fermi} = -G_F(\bar{e}\gamma^{\mu}\nu)(\bar{p}\gamma_{\mu}n) + h.c., \tag{2.1}$$

where G_F is the Fermi constant, with unit of GeV^{-2}. This theory, despite of its success in predicting processes at low energy, is however non-renormalisable, as this term is of mass dimension 6, where a mass dimension $d \leq 4$ is required for it being renormalisable [93].

In order to describe the weak force in the same fashion as the electromagnetic force, Yang and Mills proposed a non-Abelian gauge theory [94], [1] thus paving the way to the so-called SM. This theory, however, remained unnoticed at first, as all the particles in this theory do not possess masses, which contradicts experiments. Following the later development of the introduction of mass via the spontaneous symmetry breaking mechanism in particle physics by Anderson [95], Higgs [96], Englert and Brout [97] and others [98, 99] (also known as the Higgs mechanism), a theory which can unify the electromagnetic and weak forces is finally possible. It was Glashow who combined the electromagnetic and weak forces into the same gauge theory, and Weinberg and Salam who incorporated the Higgs mechanism into it under the $SU(2)_L \times U(1)_Y$ gauge group, where L and Y are the quantum numbers for left-handed chirality and weak hypercharge, respectively [100–102].

The theory for the strong force to describe the interaction between quarks and gluons can be proposed in a similar way, via the $SU(3)_C$ gauge group, where C is the quantum number for colour. This theory is however not as simple as the other forces, due to the non-perturbative nature resulting from the large gauge coupling. For example, an isolated quark is not observable in experiments due to colour confinement. With contributions from many bright minds, the parton model [103, 104]

---

[1] The original theory was actually aimed to describe the strong force based on a non-Abelian $SU(2)$ gauge theory for the isospin doublet of protons and neutrons.

and Quantum Chromodynamics (QCD) can successfully describe the strong force with the discovery of asymptotic freedom [105, 106].

The Glashow-Salam-Weinberg model together with QCD make up the SM to describe and unify the electromagnetic, weak, and strong forces via the $SU(3)_C \times SU(2)_L \times U(1)_Y$ gauge group.

The quantum theory for gravitational force is however not renormalisable, so the development of quantum gravity is still very much a work in progress.

2.2 SM particle content and Lagrangian

The SM of particle physics is a Quantum Field Theory (QFT) on a four-dimensional Minkowski spacetime under the symmetry group $SU(3)_C \times SU(2)_L \times U(1)_Y$. There is only the left-handed $SU(2)_L$ group, as parity is violated in experiments [107]. Therefore, the left-handed component of a fermion is expressed as the fundamental representation of $SU(2)$, while the right-handed component as a singlet. The particle content of the SM is expressed in Tab. 2.1. Under the chiral projection, i.e. $f_{R/L} = (1 \pm \gamma^5) f$, fermions become left-handed or right-handed Weyl fields. The conjugate of the left-handed Weyl fields are defined as $f^c = C\bar{f_R}^T$, where C is the charge conjugation matrix.

The dynamics of the theory is encoded in its Lagrangian,

$$\mathscr{L}_{\text{SM}} = \mathscr{L}_{\text{gauge}} + \mathscr{L}_{\text{fermion}} + \mathscr{L}_{\text{scalar}} + \mathscr{L}_{\text{Yukawa}}. \tag{2.2}$$

The gauge sector of the Lagrangian describes how the forces are mediated by the gauge bosons, i.e. the kinetic terms of the SM gauge fields. It can be expressed as

$$\mathscr{L}_{\text{SM gauge}} = -\frac{1}{4} G^a_{\mu\nu} G^{\mu\nu a} - \frac{1}{4} W^i_{\mu\nu} W^{\mu\nu i} - \frac{1}{4} F_{\mu\nu} F^{\mu\nu}, \tag{2.3}$$

ψ	$SU(3)_C$	$SU(2)_L$	$U(1)_Y$
$q_{iL} \equiv \begin{pmatrix} u_L^r & u_L^g & u_L^b \\ d_L^r & d_L^g & d_L^b \end{pmatrix}^i$	3	2	$\frac{1}{6}$
$(u_R^r, u_R^g, u_R^b)^i$	$\bar{3}$	1	$-\frac{2}{3}$
$(d_R^r, d_R^g, d_R^b)^i$	$\bar{3}$	1	$\frac{1}{3}$
$l_{iL} \equiv \begin{pmatrix} \nu_L \\ l_L \end{pmatrix}^i$	1	2	$-\frac{1}{2}$
l_R^i	1	1	1
G	8	1	0
W	1	3	0
B	1	1	0
H	1	2	$\frac{1}{2}$

Table 2.1: The fermionic and bosonic particle content and the respective charge or representation in the SM. The weak hypercharge is given by $Y = Q - T_3$, where Q is the electric charge and T_3 the third component of isospin. The indices $\{r, g, b\}$ of the quarks are their colours, and the i index represents the generation such that $u^i \in \{u, c, t\}$ and $d^i \in \{d, s, b\}$. The symbol i for leptons denotes flavour, i.e. $l_i \in \{e, \mu, \tau\}$.

where the field strength tensors are defined by

$$G^a_{\mu\nu} = \partial_\mu G^a_\nu - \partial_\nu G^a_\mu + g_s f^{abc} G^b_\mu G^c_\nu, \tag{2.4}$$

$$W^i_{\mu\nu} = \partial_\mu W^i_\nu - \partial_\nu W^i_\mu + g \varepsilon^{ijk} W^j_\mu W^k_\nu, \tag{2.5}$$

$$F_{\mu\nu} = \partial_\mu B_\nu - \partial_\nu B_\mu. \tag{2.6}$$

Here, g_s and g are the corresponding gauge couplings for strong ($SU(3)_C$) and weak ($SU(2)_L$) forces, and G, W, B are the corresponding gauge bosons for the $SU(3)_C$, $SU(2)_L$ and $U(1)_Y$ groups, respectively.

The structure constants ε^{ijk} and f^{abc} for the $SU(2)_L$ and $SU(3)_C$ groups are defined through

$$[\tau^i, \tau^j] = i\varepsilon^{ijk}\tau^k, \tag{2.7}$$

$$[\lambda^a, \lambda^b] = i f^{abc}\lambda^c, \tag{2.8}$$

where τ^i and λ^a are the generators for the $SU(2)_L$ and $SU(3)_C$ groups. Actually, ε^{ijk} is just the Levi-Civita tensor with $\varepsilon^{123} = 1$ and antisymmetry under exchange of indices.

The fermion sector of the Lagrangian contains the fermionic kinetic terms after symmetry breaking, and it can be expressed as

$$\begin{aligned}\mathscr{L}_{\text{SM fermion}} = & \sum_{k=1}^{3} (i\overline{q_{kL}}\gamma_\mu D^\mu q_{kL} + i\overline{u_{kR}}\gamma_\mu D^\mu u_{kR} + i\overline{d_{kR}}\gamma_\mu D^\mu d_{kR}) \\ & + \sum_{j=e,\mu\tau} (i\overline{l_{jL}}\gamma_\mu D^\mu l_{jL} + i\overline{l_{jR}}\gamma_\mu D^\mu l_{jR}),\end{aligned} \tag{2.9}$$

where the covariant derivatives of the model are defined as

$$D_\mu = \partial_\mu + ig_s\lambda_a G^a_\mu + ig\tau_i W^i_\mu + ig_1 Y B_\mu. \tag{2.10}$$

Here, Y is the weak hypercharge of the corresponding particle. Also, the τ_i and λ_a terms only apply to $SU(2)_L$ doublets and $SU(3)$ triplets, respectively. q_L is the left-handed quark doublet, u_R is the right-handed up-quark singlet, d_R is the right-handed down-quark singlet, l_L is the left-handed lepton doublet, and l_R is the right-handed lepton singlet. g_1 is the gauge coupling for the $U(1)_Y$ group.

The scalar sector of the Lagrangian contains information on how the masses are generated via the spontaneous symmetry breaking of the Higgs field H,

$$\begin{aligned}\mathscr{L}_{\text{SM scalar}} &= (D_\mu H)^\dagger (D^\mu H) - V(H), \\ V(H) &= -\mu^2 H^\dagger H + \lambda (H^\dagger H)^2.\end{aligned} \tag{2.11}$$

Details of the Higgs mechanism will be discussed in the next subsection.

Finally, the Yukawa sector of the Lagrangian can be expressed as

$$\begin{aligned}\mathscr{L}_{\text{SM Yukawa}} = & \sum_{i,j=1}^{3} (-y^d_{ij}\overline{q_{Li}} H d_{Rj} - y^u_{ij}\overline{q_{Li}}\tilde{H} u_{Rj}) \\ & - \sum_{j=e,\mu,\tau} (y^l \overline{l_{jL}} H l_{jR}) + +h.c.,\end{aligned} \tag{2.12}$$

where $\tilde{H} = i\tau_2 H^*$.

2.3 Spontaneous electroweak symmetry breaking

In the SM introduced so far, we have not found any mass terms. For the gauge bosons, this is because they have to be massless to maintain gauge invariance. As already mentioned, the question of masses is resolved via spontaneous EW symmetry breaking, i.e., the Higgs mechanism.

We start with a simple example of the breaking of a $U(1)$ symmetry instead of the breaking of $SU(2)_L \times U(1)_Y \to U(1)_{EM}$. For a complex scalar field Φ with a Lagrangian invariant under a local $U(1)$ gauge transformation,

$$\Phi \to \Phi' = e^{-iq\theta}\Phi, \tag{2.13}$$

where $\theta = \theta(x)$ is space and time dependent as the gauge is local. In order to introduce a Lagrangian invariant under this transformation, a massless gauge field A_μ is added, so we generally have a Lagrangian (in analogy to Electrodynamics),

$$\mathscr{L} = [(\partial_\mu - iqA_\mu)\Phi^\dagger][(\partial_\mu + iqA_\mu)\Phi] - \frac{1}{4}F_{\mu\nu}F^{\mu\nu} - V(\Phi^\dagger\Phi), \tag{2.14}$$

where $F_{\mu\nu} = \partial_\mu A_\nu - \partial_\nu A_\mu$.

The so-called scalar potential $V(\Phi^\dagger\Phi)$ is given by

$$V(\Phi^\dagger\Phi) = -\mu^2(\Phi^\dagger\Phi) + \lambda(\Phi^\dagger\Phi)^2 + C, \tag{2.15}$$

where C stands for a constant. If $\mu^2 < 0$ and $\lambda > 0$, there is only a minimum at $\Phi = 0$, but for $\mu^2 > 0$ and $\lambda > 0$, there are two minima at $\Phi = \pm\sqrt{\frac{\mu^2}{2\lambda}} \equiv \pm\phi_0$.[2] We can then write the potential as

$$V(\Phi^\dagger\Phi) = \frac{\mu^2}{2\phi_0^2}[\Phi^\dagger\Phi - \phi_0^2]^2. \tag{2.16}$$

We can do an expansion about the minimum, $\Phi'(x) = \phi_0 + h(x)/\sqrt{2}$, where

---

[2] We here implicitly choose the complex phase of Φ such that ϕ_0 is on the real axis.

$h(x)$ is real, and we obtain the Lagrangian

$$\begin{aligned}\mathscr{L} =& -\frac{1}{4}F'_{\mu\nu}F'^{\mu\nu} + [(\partial_\mu - iqA'_\mu)(\phi_0 + h/\sqrt{2})][(\partial_\mu + iqA'_\mu)(\phi_0 + h/\sqrt{2})] \\ & -\frac{\mu^2}{2\phi_0^2}[\sqrt{2}\phi_0 h + \frac{1}{2}h^2]^2.\end{aligned} \tag{2.17}$$

Now the Lagrangian is not manifestly gauge invariant anymore, i.e. the $U(1)$ symmetry is broken at the minimum.

Observing the terms above, we find two mass terms $\mu^2 h^2$ and $q^2\phi_0^2 A_\mu A^\mu$, thus we have a single scalar field $h(x)$ corresponding to a spinless boson of mass $\sqrt{2}\mu$, and a vector field A_μ corresponding to a massive spin one boson with mass $\sqrt{2}q\phi_0$. From QED, we understand a massless vector field has two independent components, while a massive vector field has three. Therefore, the complex field Φ which has two components, is replaced by the massive scalar field h with one component which we call the physical Higgs field, and the additional longitudinal polarised state of the vector field A_μ.

In the SM, due to the breaking of $SU(3)_C \times SU(2)_L \times U(1)_Y$ into $SU(3)_C \times U(1)_{EM}$, the breaking leads to three massive gauge bosons, $W^\pm$ and Z. Similarly, we expand the Higgs doublet at its minimum $v \equiv \sqrt{\frac{\mu^2}{2\lambda}}$,

$$H = \begin{pmatrix} 0 \\ \frac{1}{\sqrt{2}}(h+v) \end{pmatrix}. \tag{2.18}$$

Therefore, the scalar sector of the Lagrangian in Eqn. (2.11) will become

$$\begin{aligned}\mathscr{L}_{\text{scalar}} =& \frac{1}{2}\partial_\mu h \partial^\mu h - \lambda v^2 h^2 - \lambda v h^3 - \frac{1}{4}\lambda h^4 \\ & + \frac{1}{8}(h+v)^2[g^2 W_\mu^1 W^{1\mu} + g^2 W_\mu^2 W^{2\mu} \\ & + (gW_\mu^3 - 2g_1 Y B_\mu)(gW^{3\mu} - 2g_1 Y B^\mu)] \\ & + SU(3)_C\ part,\end{aligned} \tag{2.19}$$

where we have diagonalized the quadratic terms of the gauge fields inside the bracket. We can transform the gauge fields to the physical intermediate vector bosons,

$$W_\mu^\pm = \frac{1}{\sqrt{2}}(W_\mu^1 \mp W_\mu^2),\ Z_\mu = \frac{1}{\sqrt{g^2+g_1^2}}(gW_\mu^3 - g_1 B_\mu). \tag{2.20}$$

Thus they acquire masses as $m_W = \frac{1}{2}g\nu$ and $m_Z = \frac{1}{2}\sqrt{g^2+g_1^2}\nu$. The combination of W_μ^3 and B_μ gives the remaining gauge boson responsible for the electromagnetic interaction, also known as the photon,

$$A_\mu = \frac{1}{\sqrt{g^2+g_1^2}}(g_1 W_\mu^3 + gB_\mu), \tag{2.21}$$

which stays massless.

We can define the Weinberg angle θ_W to describe the weak mixing for these bosons,

$$\sin\theta_W = \frac{g_1}{\sqrt{g^2+g_1^2}}, \tag{2.22}$$

and thus

$$A_\mu = \sin\theta_W W_\mu^3 + \cos\theta_W B_\mu, \quad Z_\mu = \cos\theta_W W_\mu^3 - \sin\theta B_\mu. \tag{2.23}$$

The Higgs mechanism explains how gauge bosons acquire masses without losing overall gauge symmetry. The origin of the masses of the fermions is due to the Yukawa terms $-y\bar{f}_L H f_R$ as shown in Eqn. (2.12). After spontaneous symmetry breaking, it gives $-\frac{y\nu}{\sqrt{2}}\bar{F}_L F_R$, so the charged fermions acquire masses via the mass matrix $\frac{y\nu}{\sqrt{2}}$.

The mass matrices for quarks $y_{ij}^{d,u}$ and leptons y_{ij}^{l} are not diagonal in general. To get physical massive fermions, the mass matrices are diagnolized using a bi-unitary transformation, with independent rotations for left-handed and right-handed quarks as well as the leptons as

$$M_u = U_L^u \cdot \mathrm{diag}(m_u, m_c, m_t) \cdot U_R^u, \tag{2.24}$$

where $\mathrm{diag}(m_u, m_c, m_t)$ are real, diagonal matrices corresponding to the physical masses of up-type quarks. Thus, the eigenstates of quarks in the weak interaction q^i can be expressed via their mass eigenstates q^m,

$$u_L^i = \sum_{m=1,2,3} [U_L^u]_{im} u_L^m, \;\; u_R^i = \sum_{m=1,2,3} [U_R^u]_{im} u_R^m. \tag{2.25}$$

Similarly, we can diagonalise the mass matrices for the down-type quarks and the leptons as well.

Under these transformations, the terms in the fermion Lagrangian describing the weak interaction of charged currents for quarks will give

$$\begin{aligned} \mathscr{L}_{\text{Fermion}} &\supset \frac{g}{\sqrt{2}} W_\mu^+ \bar{u}_L^i \gamma^\mu d_{Li} + h.c. \\ &= \frac{g}{\sqrt{2}} W_\mu^+ [U_L^u U_L^{d\dagger}]_{m,m'} \bar{u}_L^m \gamma^\mu d_L^{m\prime} + \text{h.c.}, \end{aligned} \tag{2.26}$$

where the combination $[U_L^u U_L^{d\dagger}]$ is also called the Cabibbo-Kobayashi-Maskawa (CKM) mixing matrix,

$$V_{CKM} \equiv U_L^u U_L^{d\dagger} = \begin{pmatrix} V_{ud} & V_{us} & V_{ub} \\ V_{cd} & V_{cs} & V_{cd} \\ V_{td} & V_{ts} & V_{tb} \end{pmatrix}. \tag{2.27}$$

The CKM mixing matrix can be parameterized by four parameters, three quark mixing angles $\Theta_{12}, \Theta_{13}, \Theta_{23} \in [0, \frac{\pi}{2}]$ and one complex CP phase $\alpha_{CP} \in [0, \frac{\pi}{2}]$. The standard parametrisation is

$$V_{CKM} = \begin{pmatrix} c_{12}c_{13} & s_{12}c_{13} & s_{13}e^{-i\alpha_{CP}} \\ -s_{12}c_{23} - c_{12}s_{13}s_{23}e^{i\alpha_{CP}} & c_{12}c_{23} - s_{12}s_{13}s_{23}e^{i\alpha_{CP}} & c_{13}s_{23} \\ s_{12}s_{23} - c_{12}s_{13}c_{23}e^{i\alpha_{CP}} & -c_{12}s_{23} - s_{12}s_{13}c_{23}e^{i\alpha_{CP}} & c_{13}c_{23} \end{pmatrix}, \tag{2.28}$$

where $s_{ij} \equiv \sin\Theta_{ij}$, $c_{ij} \equiv \cos\Theta_{ij}$. The complex CP phase α_{CP} indicates the violation of CP symmetry, as observed in experiments. This can lead to an asymmetry between matter and antimatter, which will be discussed in detail in the following section. In the meantime, there are two other parameterisation including the Kobayashi and Maskawa parameterisation, and Wolfenstein parameterisation (see Refs. [108, 109]).

Under the same procedure, the eigenstates of leptons in weak interactions can be expressed via their mass eigenstates. However, as neutrinos are massless in the SM, one can always redefine $U_L^l l_L^m \equiv l_L^{m'}$ to make the mass term diagonal, so the masses for leptons are simply $m_l = \frac{1}{\sqrt{2}} y^l v$. However, once neutrinos acquire masses as discussed in the next subsection, the charged currents for leptons would no longer be diagonal in the mass eigenstates, and the combination of $[U_L^{\nu} U_L^{l\dagger}]$ is the lepton mixing matrix.

2.4 Physics beyond the Standard Model

The SM is one of the most successful physical theories, describing the electromagnetic, weak and strong interactions which account for most of the phenomena of the universe, in the same framework. It provides a detailed picture of the basic building blocks from which all the known physical substance is made of. It is renormalisable and Lorentz invariant, and has a great predictive power tested in experiments. Since the days it was proposed and developed, it successfully predicted the existence of particles like the weak bosons, $W^{\pm}$ and Z, and accommodated the different flavours of quarks and other particles as confirmed in the experiments. Being the last undiscovered particle in the SM, of tremendous importance in explaining the origin of the mass, the Higgs boson was finally discovered at the LHC of the European Organisation for Nuclear Research (CERN) [110, 111]. So far, the SM shows great consistency with the experimental data of the LHC, as no physics exceeding the SM has been discovered yet.

In spite of its success, the SM is widely considered as an effective field theory at the EW scale, of a more fundamental ultraviolet theory. It can not incorporate the gravitational force. This is due to the fact that there is no known way to treat gravity in a quantum field theory. While the SM is consistent with most of the experimental data, it is often seen to be quite *ad hoc*, as its gauge group and particle content seem arbitary. It also lacks an explanation for having three generations of leptons and quarks. Another shortcoming of the SM is the hierarchy problem [112]: At the Planck scale, $\Lambda_{Pl} \approx 10^{19}$ GeV, the effects of gravity become important and must be taken into account. If the SM is regarded as an effective theory, and the Planck scale is its cut-off, the radiative correction to the Higgs mass $\propto \Lambda_{Pl}^2 H^\dagger H$ diverge quadratically. Although this can be resolved by tuning the bare Higgs mass, this would, however, require an extremely accurate cancellation to yield the experimental Higgs mass, generally known as fine tuning. This problem led to the belief that there must be new physics just above the EW scale, which would avoid large radiative corrections.

Moreover, there are several obvious disagreements with experimental data in cosmology and neutrino experiments such as the existence of dark matter and dark energy, the asymmetry between matter and antimatter, and the observation of neutrino mass and its mixing in neutrino oscillation experiments. Explaining these phenomena should finally give rise to physics beyond the SM. We will, however, emphasise the neutrino masses, as they are crucial for the following discussion in this thesis. In the following, we summarise the evidence regarding the dark matter and dark energy, the matter and antimatter asymmetry, as well as neutrino mixing and mass.

Dark matter and dark energy Although the SM seems to explain all the basic building blocks of matter, there are discoveries from cosmological observations that there are additional gravitational effects that cannot be accounted by normal matter via the accepted gravity theory. For example, the observed stellar populations only make a small contribution to the rotation curves of low-surface-brightness galaxies [113]. This fact points toward the existence of an additional content of matter. As it is not incorporated in the SM, it is believed that it does not interact via SM interactions but gravity. Therefore, it is called dark matter [114].

The observation of the accelerating expansion of the universe points towards the existence of dark energy. The Hubble Space Telescope observed that the universe was actually expanding faster than it was before, not slowed down by gravity as expected otherwise [115]. The existence of dark energy is generally considered to be the explanation. It will contribute to the energy density of the universe thus accelerating the expansion of the universe. One form of dark energy can be from the cosmological constant in General Relativity [116], which will introduce an energy density homogeneously over space.

By fitting theoretical models for the composition of the universe including the above assumptions of the existence of dark matter and dark energy with the combined observations, it is found that the matter and energy of the universe roughly consists of 68% dark energy, 27% dark matter, and 5% normal matter. In other words, the SM cannot explain 95% of the matter and energy of the universe [117, 118].

Matter and antimatter asymmetry In everyday life, we obviously observe a universe dominated by matter rather than anti-matter. This is confirmed from the observation of the smallness of the ratio of baryons to photons in the Cosmic Microwave Radiation Background [119], giving rise to the matter-antimatter asymmetry problem. The imbalance of baryonic to antibaryonic matter requires specific ingredients in a fundamental theory. In order to generate such an asymmetry, there are three necessary conditions as proposed by Sakharov [120]: baryon number B violation, charge conjugation C and CP violation and the simultaneous presence of interactions out of thermal equilibrium. Then additional baryons over anti-baryons are produced via B violating processes which are not cancelled by processes that produce anti-baryons over baryons due to C violation. CP violation is also needed, otherwise an equal numbers of left-handed baryons and right-handed anti-baryons would be produced, as well as equal numbers of left-handed anti-baryons and right-handed baryons. Finally, the rate of baryogenesis must be less than the rate of expansion of the universe, so the pair annihilation of the particles and their corresponding antiparticles is reduced by the rapid expansion, so that they do not achieve thermal equilibrium. Otherwise CPT symmetry would assure compensation between processes increasing and decreasing the baryon number [121].

Baryogenesis can in principle be incorporated in the SM, as it does include B, C and CP violation and EW breaking could occur out of equilibrium. However, the amount of CP violation in SM does not sufficiently account for the matter-antimatter asymmetry from the observation and the observed Higgs mass $m_{h_{SM}} \approxeq 125$ GeV points towards a thermally equilibrated EW symmetry breaking. If neutrinos had masses, as indicated by experiments discussed below, there can be additional CP violating phases in the neutrino mixing matrix in analogy to the CKM matrix.

Neutrino mixing and mass Another puzzle for the SM is that it cannot explain the presence of tiny masses of neutrinos and their mixings in the neutrino oscillation experiments. A great deal of evidence, for neutrino oscillation has been collected from various sources. The first being the observation of the disappearance of solar neutrinos in Ray Davis' Homestake experiment [4–6]. It was later confirmed by the Sudbury Neutrino Observation that such a deficit is due to a neutrino flavour change, i.e. neutrino oscillations [11]. Later, such oscillation effects have also been detected by other experiments from other sources of neutrinos including atmospheric neutrinos [14–16], reactor neutrinos [17] as well as the collider neutrinos [18]. These experiments indicate that neutrinos oscillate between different flavours, which arises from the mixing between the flavour and mass eigenstates. Their masses can be constrained by beta decay experiments such as KATRIN [122] from tritium decay, neutrinoless double beta ($0\nu\beta\beta$) decay experiments [123] and cosmological observations such as by the Planck satellite [124]. Therefore, neutrinos do have masses but they are tiny $m_\nu \lesssim 0.1$ eV as indicated by experiments [124–127]. In the following discussion, we will introduce the major properties of these experimental discoveries for the neutrinos in detail.

Once the neutrinos had masses, the mixing between the flavour and mass eigenstates is described by a unitary matrix, known as the Pontecorvo-Maki-Nakagawa-Sakata (PMNS) matrix matrix,

$$\begin{pmatrix} \nu^e \\ \nu^\mu \\ \nu^\tau \end{pmatrix} = U_{PMNS} \begin{pmatrix} \nu^1 \\ \nu^2 \\ \nu^3 \end{pmatrix} = \begin{pmatrix} U_{e1} & U_{e2} & U_{e3} \\ U_{\mu 1} & U_{\mu 2} & U_{\mu 3} \\ U_{\tau 1} & U_{\tau 2} & U_{\tau 3} \end{pmatrix} \begin{pmatrix} \nu^1 \\ \nu^2 \\ \nu^3 \end{pmatrix}. \tag{2.29}$$

In analogy to the quark CKM matrix, the PMNS matrix can be conveniently parameterized by three mixing angles θ_{12}, θ_{23} and θ_{13} and a phase δ related to Dirac *CP* violation. Two additional phases ρ and σ are present if the neutrinos are Majorana fermions [128, 129]. The PMNS mixing matrix is then

$$U_{PMNS} = \begin{pmatrix} c_{12}c_{13} & s_{12}c_{13} & s_{13}e^{-i\delta} \\ -s_{12}c_{23} - c_{12}s_{13}s_{23}e^{i\delta} & c_{12}c_{23} - s_{12}s_{13}s_{23}e^{i\delta} & c_{13}s_{23} \\ s_{12}s_{23} - c_{12}s_{13}c_{23}e^{i\delta} & -c_{12}s_{23} - s_{12}s_{13}c_{23}e^{i\delta} & c_{13}c_{23} \end{pmatrix} \tag{2.30}$$
$$\times \begin{pmatrix} 1 & 0 & 0 \\ 0 & e^{i\rho} & 0 \\ 0 & 0 & e^{i\sigma} \end{pmatrix}$$

where the short-hand notation $s_{ij} \equiv \sin\theta_{ij}$ and $c_{ij} \equiv cos\theta_{ij}$ is used.

The only experimental proof of lepton mixing is through the observation of neutrino oscillations. Starting at time $t = 0$, one can expand a neutrino flavour eigenstate in terms of neutrino mass eigenstates using the above PMNS mixing matrix,

$$|\nu(t=0)\rangle \equiv |\nu^l\rangle = \sum_i U^*_{li}|\nu^i\rangle, \tag{2.31}$$

where the complex conjugation of the mixing matrix elements comes from the fact that the corresponding states are created by conjugate fields $\bar{\nu}^i$ acting on the vacuum. The mass eigenstates are eigenstates of the Hamiltonian in vacuum and they evolve in time as

$$|\nu(t)\rangle = \sum_i U^*_{li} e^{-iE_i t} |\nu^i\rangle, \tag{2.32}$$

where $E_i = \sqrt{p^2 + m_i^2}$ is the energy of the mass eigenstates ν^i, and m_i and p are its mass and momentum, respectively.

We can express the flavour eigenstates for a given time t as a superposition of flavour eigenstates as well,

$$|\nu(t)\rangle = \sum_i U^*_{li} e^{-iE_i t} \sum_{l'} U_{l'i} |\nu^{l'}\rangle, \tag{2.33}$$

where l' is the flavour of the neutrino detected after time t. Thus, the probability of the neutrino flavour changing between eigenstates l and l' can be expressed as

$$\begin{aligned} P(\nu^l \to \nu^{l'}) &= |\langle \nu^{l'} | \nu(t) \rangle|^2 \qquad (2.34) \\ &= |\sum_i U^*_{li} U_{l'i} e^{-iE_i t} \langle \nu^{l'} | \nu^{l'} \rangle|^2 = \sum_{i,j} U^*_{li} U_{l'i} U_{lj} U^*_{l'j} e^{-i(E_i - E_j)t}. \end{aligned}$$

In the ultra-relativistic limit, we approximately have

$$\sqrt{p^2 + m_i^2} \approx p + \frac{m_i^2}{2p} + p\mathscr{O}\left(\frac{m_i^4}{p^4}\right). \tag{2.35}$$

Therefore, in this limit we can obtain the probability [130]

$$\begin{aligned} P(\nu^l \to \nu^{l'}) = \delta_{ll'} &- 4\sum_{i<j} Re[U^*_{li} U_{l'i} U_{lj} U^*_{l'j}] \sin^2\left(\frac{\triangle m^2_{ij} L}{4E}\right) \qquad (2.36) \\ &+ 2\sum_{i<j} Im[U^*_{li} U_{l'i} U_{lj} U^*_{l'j}] \sin\left(\frac{\triangle m^2_{ij} L}{2E}\right), \end{aligned}$$

where $p \approx E$ and $t \approx L$ for an ultra-relativistic neutrino, L is the distance between neutrino production and detection, and $\triangle m^2_{ij} \equiv m_i^2 - m_j^2$ is the difference between the square of the masses for state i and j.

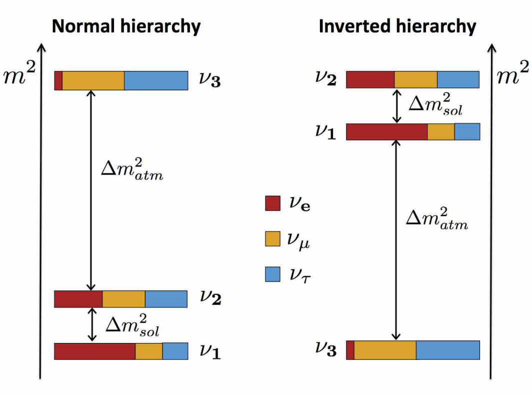

Figure 2.1: Normal (left) and inverted (right) hierarchy of neutrino mass eigenstates taken from Ref. [131]. The colour bands indicate the components of individual flavour eigenstates within a particular mass eigenstate.

This formula describes neutrino oscillations for the case of three flavours $i, j = e, \mu, \tau$. However the two-flavour scenario is found to be important, as it gives a good description of many neutrino oscillation experiments, such as the oscillation between ν_e and ν_μ in Ray Davis's Homestake experiment [4–6]. In case of two neutrino flavours, the corresponding mixing matrix is real (i.e. there is no CP-violating phase) and can be parameterized by a single angle θ

$$U_{PMNS}^{(N_f=2)} = \begin{pmatrix} \cos\theta & -\sin\theta \\ \sin\theta & \cos\theta \end{pmatrix}. \tag{2.37}$$

Therefore, the oscillation probability ($l \neq l'$) reads

$$P(\nu^l \to \nu^{l'}) = \sin^2(2\theta)\sin^2\left(\frac{\triangle m_{ij}^2 L}{2E}\right), \tag{2.38}$$

where θ is the mixing angle between two flavour. We can obtain the values of these parameters from the data of neutrino oscillation experiments. The mass eigenstates of neutrinos are defined as $\nu_{1,2,3}$ for the eigenstates with largest to smallest component of ν_e flavour, respectively. Therefore, the Solar neutrino oscillation experiments give the angle θ_{12} in Eqn. (2.30) and the mass difference $\triangle m^2_{\text{sol}} \equiv \triangle m^2_{21} = m_2^2 - m_1^2$ [4–10]. The atmospheric or long-baseline accelerator neutrino oscillation experiments yield the angle θ_{23} and mass difference

$\triangle m^2_{\text{atm}} \equiv \triangle m^2_{23} = m^2_2 - m^2_3$ [14–16, 18]. The angle and mass difference between the first and third generation θ_{13} and $\triangle m^2_{31}$ are determined by the short-baseline reactor neutrino oscillation experiments, or from long-baseline $\nu_\mu \to \nu_e$ oscillations [17]. The approximate values of the mass differences are given as $\triangle m^2_{\text{sol}} \equiv \triangle m^2_{21} \approx 10^{-5}$ eV^2 $\ll \triangle m^2_{31} \simeq \triangle m^2_{32} \equiv |\triangle m^2_{\text{atm}}| \approx 10^{-3}$ eV^2, while the actual values of all mixing parameters via a global fit of experimental oscillation data can be found in Ref. [132]. As the sign of $|\triangle m^2_{\text{atm}}|$ is not measured yet, there are two different orderings of the neutrino mass eigenstates. If ν_1 represents the neutrino with largest ν_e component and ν_3 with the smallest one (see Fig. 2.1), then the three masses can be ordered either as $m_1 < m_2 < m_3$ with $\triangle m^2_{\text{atm}} > 0$, or $m_3 < m_1 < m_2$ with $\triangle m^2_{\text{atm}} < 0$. The first ordering is as known as the *normal hierarchy* (NH), and the second as the *inverted hierarchy* (IH). The two scenarios are shown in Fig. 2.1. Therefore we can express the two larger mass eigenstates of the neutrino for the two orderings from the observables and the lightest one as

$$m_2(\text{NH}) = \sqrt{m_1^2 + \triangle m^2_{\text{sol}}}, \;\; m_2(\text{IH}) = \sqrt{m_3^2 + \triangle m^2_{\text{sol}} + |\triangle m^2_{\text{atm}}|}, \tag{2.39}$$

$$m_3(\text{NH}) = \sqrt{m_1^2 + \triangle m^2_{\text{sol}} + |\triangle m^2_{\text{atm}}|}, \;\; m_1(\text{IH}) = \sqrt{m_3^2 + |\triangle m^2_{\text{atm}}|}. \tag{2.40}$$

For the absolute neutrino mass scales, we could determine them by measurements of the energy distribution of electrons in beta decay, as the non-zero neutrino mass would impact the kinematical endpoint [122, 133]. The formula of the spectrum is approximately expressed as

$$\frac{dN_e}{dE_e} \propto (E_e - Q)\sqrt{(E_e - Q)^2 - m^2_\beta}, \tag{2.41}$$

where Q is the energy released in the decay, E_e is the energy for the electron and m_β is the neutrino mass parameter

$$m_\beta = \sqrt{\sum |U_{ei}|^2 m^2_{\nu_i}}, \tag{2.42}$$

which can be obtained from the curve. The current upper limit on the absolute neutrino mass from the tritium decays is m_β <1.1 eV at 90% C.L. from KATRIN [133]. In the near future, it is expected to be more sensitive, reaching $m_\beta \approx 0.2$ eV at 90% C.L. and a potential discovery of $m_\beta = 0.35$ eV at 5 σ.

Another possibility to probe absolute neutrino masses is to search for neutrinoless double beta decay. Generally, nuclear double beta decay is the process

$$\begin{aligned} (A,Z) &\to (A,Z+2)+2e^-(+\text{missing energy}), \qquad (2.43)\\ \text{or } (A,Z) &\to (A,Z-2)+2e^+(+\text{missing energy}), \end{aligned}$$

where a nucleus with A nucleons and Z protons transitions to another one with two more protons and the same nucleon number by emission of two electrons and possibly other light particles, or to another one with two less protons and the same nucleon number by emission of two positrons and possibly other light particles. In the standard case, the light particles are two antineutrinos and the process is simply a ‘double copy’ of the standard beta decay, and is referred to as two-neutrino double beta ($2\nu\beta\beta$) decay. However, as to be mentioned in the following discussion that the neutrino can be Majorana particles, i.e., they are their own antiparticles, the two antineutrinos in the final states can annihilate so there are no neutrinos produced in the process. This is referred to as $0\nu\beta\beta$ decay. Searches for this process have been carried out in many experiments, see Ref. [123] for a summary of the existing experiments and their limits. The observable in the experiments is the inverse decay half-life

$$[T_{1/2}^{0\nu\beta\beta}]^{-1} = G_{0\nu}|\mathscr{M}|^2\left(\frac{m_{\beta\beta}}{m_e}\right)^2, \qquad (2.44)$$

which is dependent on the effective neutrino mass,

$$m_{\beta\beta} = \left|\sum_{i=1}^{3} U_{ei}^2 m_{\nu_i}\right|. \qquad (2.45)$$

Here, $G_{0\nu}$ is the so-called phase space factor, $\mathscr{M}$ is the nuclear matrix element calculable in nuclear physics and U_{ei} is the neutrino mixing element between the

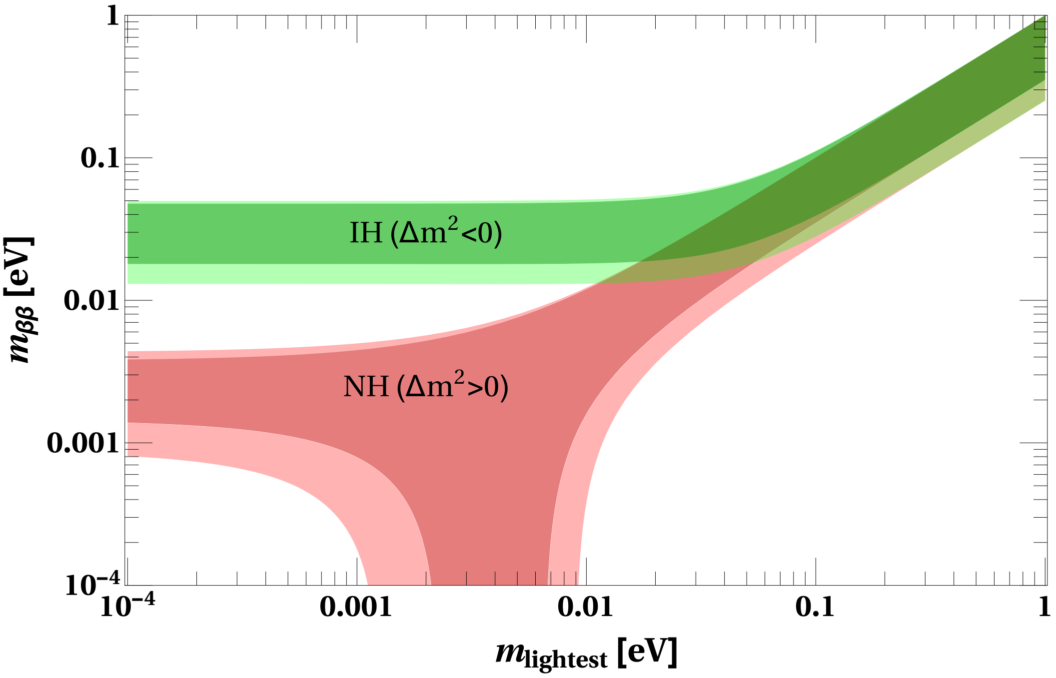

Figure 2.2: Effective neutrino mass as a function of the lightest neutrino mass shown in the logarithmic scale both for normal ($\triangle m^2_{atm} > 0$) and inverted ($\triangle m^2_{atm} < 0$) hierachy. Figure from Ref. [134].

electron neutrino and ith ($i = 1,2,3$) mass eigenstate. As mentioned earlier, neutrino mixing can contain additional complex phases if neutrinos are Majorana particles, and Eqn. (2.45) can be rewritten as

$$m_{\beta\beta} = \left| \sum_{i=1}^{3} e^{i\alpha_i} |U_{ei}|^2 m_{\nu_i} \right| , \tag{2.46}$$

where $\alpha_1 = 0$, and $\alpha_2 = 2\rho, \alpha_3 = 2\sigma$. Here, ρ and σ are the Majorana phases defined in Eqn. (2.30). Having not observed this process so far sets a lower limits on its half life, and thus an upper limit on $m_{\beta\beta}$. The current limits on the neutrino mass from the $0\nu\beta\beta$ experiments depends on the ordering of neutrino masses, as summarised in Fig. 2.2. Since the *CP* violating Majorana phases in Eqn. (2.46) cannot be probed by oscillation experiments, the allowed region for $m_{\beta\beta}$ is obtained letting them vary freely. Therefore, we get bands between the maximum and minimum values for $m_{\beta\beta}$ due to the phase variation. Here the maximum and minimum values are given by $m^{\max}_{\beta\beta} = \sum_{i=1}^{3} |U_{ei}|^2 m_{\nu_i}$, and $m^{\min}_{\beta\beta} = \max\{2|U_{ei}|^2 m_{\nu_i} - m^{\max}_{\beta\beta}, 0\}$ $i = 1,2,3$

[134].

The existence of neutrino masses can also have an impact on different astrophysical and cosmological observations. Therefore, we can constrain neutrino masses from astrophysics and cosmology, in particular from their effects in cosmic structure formation. The sensitive observable is the total sum of masses of all active neutrinos, $\sum m_i$. Such limits have been set by the Planck collaboration via their Cosmic Microwave Background (CMB) data yielding $\sum m_i \lesssim 0.23$ eV [124]. Besides, upper bounds can also be set from large scale structure surveys, Hubble constant measurements, high-redshift Type-I supernovae observations and baryon acoustic oscillations measurements. Combining a number of these effects, a recent thorough analysis [135] is able to set the upper limit at $\sum m_i \lesssim 0.17$ eV.

In the following discussion of the thesis, we assume neutrino masses approximately in the range 0.01 eV $< m_\nu <$ 0.3 eV from the current limits aforementioned, taking 0.01 eV from $\sqrt{\triangle m^2_{\text{solar}}} \approx \sqrt{10^{-5}\text{eV}^2}$.

From the above discussion, neutrino masses are much smaller compared to the masses of other fermions which might suggest a different nature for their origin. Generally speaking, there are two types of mass terms in gauge theories which are Lorentz invariant, one being the Dirac mass term $m\psi\bar{\psi}$, and the other being the Majorana mass term $m\psi^T C^{-1}\psi$. In the SM, we only have the Dirac mass term for fermions, such as the $m\bar{\psi}_L\psi_R$ terms in the Yukawa part of the Lagrangian. As there is no RH neutrino in the SM, it predicts massless neutrinos, which contradicts oscillation experiments. In order to fix this, the seesaw mechanism [19,21,136–138] is believed to be the most elegant way to explain finite neutrino masses via adding additional RH neutrinos.

There are generally three different types of seesaw mechanisms at tree level depending on the underlying mediator, naming a fermion singlet (Type-I), scalar triplet (Type-II), and fermion triplet (Type-III) or even higher multiplets [19, 21, 136–140]. We will here sketch the basic idea for the Type-I seesaw. After adding the Dirac mass term $y^\nu \bar{l}_L \tilde{H} \nu_R$ (see Eqn. (2.12) for the definition of $\bar{l}_L$ and$\tilde{H}$) and Majorana mass term $M_R \overline{\nu^c_R} \nu_R$ which are allowed once three RH neutrino fields $\nu_R \equiv$

$(\nu_{R1}, \nu_{R2}, \nu_{R3})$ are added to the SM, the mass matrix for neutrinos can be written as

$$\mathscr{M} = \begin{pmatrix} 0 & M_D \\ M_D^T & M_R \end{pmatrix}, \tag{2.47}$$

where $\mathscr{M}_{LL} = 0$ as there is no such mass term as $\bar{\nu}_L \nu_L$ is not a SM gauge-singlet, M_D is the Dirac mass term of neutrinos given by $y_\nu v/\sqrt{2}$, and M_R is the Majorana mass matrix of the RH neutrinos. Neglecting the flavour structure and taking only one generation of ν_L and one of ν_R, the eigenvalues for the resulting 2 × 2 matrix are

$$m_N \approx \frac{M_R + \sqrt{M_R^2 + 4M_D^2}}{2}, \quad m_\nu \approx \frac{M_R - \sqrt{M_R^2 + 4M_D^2}}{2}. \tag{2.48}$$

When $M_R \gg M_D$, the larger eigenvalue is approximately equal to M_R, while the smaller one is approximately

$$m_\nu = -\frac{M_D^2}{M_R}. \tag{2.49}$$

From this, we have two eigenvalues, with the smaller one having an inverse relation to the larger one. Thus, we can explain the tiny neutrino masses as the smaller eigenvalue with a much heavier states N.

The RH neutrinos are often referred to as the sterile neutrinos as they do not directly interact with the SM particles. Once the neutrinos have masses, there will be mixing between the active and sterile neutrinos as

$$\begin{pmatrix} \nu_l^c \\ \nu_R \end{pmatrix} = \begin{pmatrix} V_{ll} & V_{lR} \\ V_{Rl} & V_{RR} \end{pmatrix} \begin{pmatrix} \nu^c \\ N \end{pmatrix}. \tag{2.50}$$

Here, $V_{ll} \approx U_{\text{PMNS}}$ in Eqn. (2.30) (apart from small non-unitarity corrections and if a diagonal charged lepton mass matrix is assumed) where U_{PMNS} is the charged current lepton mixing from the observed values at the oscillation experiments. For only one generation of light and heavy neutrino, this mixing reduces to the $SO(2)$

transformation,

$$\begin{pmatrix} \nu_l^c \\ \nu_R \end{pmatrix} = \begin{pmatrix} \cos\theta_\nu & -\sin\theta_\nu \\ \sin\theta_\nu & \cos\theta_\nu \end{pmatrix} \begin{pmatrix} \nu^c \\ N \end{pmatrix}. \tag{2.51}$$

Therefore, applying Eqn. (2.50) to the Lagrangian yields

$$\begin{aligned} \mathscr{L}_{\text{neutrino mass}} = & (M_D V_{ll}^* V_{Rl} + M_R V_{Rl}^* V_{Rl}) \bar{\nu}\nu \\ & + (M_D V_{lR}^* V_{RR} + M_R V_{RR}^* V_{RR}) NN + \text{h.c.}. \end{aligned} \tag{2.52}$$

As $M_D \ll M_R$, $m_N \approx M_R$ and $V_{Rl} = -V_{lR}$ from Eqn. (2.51), and we have the Type-I seesaw relation,

$$m_\nu \approx V_{lN}^2 m_N, \tag{2.53}$$

with $V_{lN} \equiv V_{Rl} \equiv \sin\theta_\nu \approx \frac{M_D}{M_R} \approx \frac{m_\nu}{m_N}$ in the one-generation case.

The seesaw mechanism can be incorporated in the SM, by adding additional heavy neutrinos. They can be produced from their mixing to light neutrinos, e.g., through $pp \to W^* \to Nl^\pm$ at the LHC. Searches for such processes have been performed at the LHC with upper limits on the active-sterile mixing as a function of the mass of the heavy neutrino. The limits can also be set from other experiments including EW precision tests, meson decays, and beam dump experiments. Details of these experiments and their limits will be discussed in Sec. 5.3. However, as indicated from the limits summarised in Fig. 5.4, these experiments fail to reach the seesaw regime of the parameter space, as shown in Eqn. (2.53), with $m_\nu \approx \sqrt{\triangle m_{\text{solar}}^2} \approx 10^{-2}$ eV and heavy neutrinos at the LHC scale $m_N \sim 1-100$ GeV would require $V_{lN} \approx 10^{-6}$. This is due to the fact that the cross section of these processes will be reduced as the square of the active-sterile mixing. Therefore, there is not sufficient cross section for the parameter space within the seesaw regime. This problem can be resolved if additional interactions were added, such as the $B-L$ gauge interaction to be discussed here. The cross section of the heavy neutrino production then do not directly depend on the active-sterile mixing.

Chapter 3

The Minimal $B-L$ Gauge Model

In the previous chapter, we have learned that the SM lacks an explanation for a series of observations, such as dark matter and dark energy, the matter antimatter asymmetry as well as neutrino masses and their mixings. Thus, a model with an extra $U(1)_{B-L}$ group, called the $B-L$ gauge model, is considered. It can generate neutrino masses via the breaking of the $U(1)_{B-L}$ group and the presence of three adding additional RH neutrinos. In this chapter, we will introduce the $B-L$ gauge model with its particle content, its full Lagrangian and its symmetry breaking pattern. We will also discuss some theoretical considerations for its parameter space.

It is worth mentioning that the full implementation of the Lagrangian including its gauge-fixing term have been developed as part of this thesis, based on Ref. [44]. This has been done by using `FeynRules`, which is a `MATHEMATICA`-based package, through implementing the particle physics model with the specified list of fields, parameters and Lagrangian. The output is a Universal FeynRules Output (UFO) [3] which can be fed to high-energy physics event generators such as `CALCHEP` [141], `FEYNARTS` [142], `SHERPA` [143], `WHIZARD` [144], `MADGRAPH` [145], `MadGraph5_aMC@NLO` [146], and `Herwig` [147] to perform Monte Carlo simulation [2]. The corresponding UFO file for the $B-L$ gauge model is available in the `FeynRules` model database at `https://feynrules.irmp.ucl.ac.be/wiki/B-L-SM` [44, 90, 148]. In Appendix A we illustrate the `FeynRules` model file, which has been developed based on the `FeynRules` model file for the SM [2] and an existing file for the $B-L$ gauge model [44]. Com-

ψ	q_L	u_R	d_R	l_L	l_R	ν_R	G	W	B	B'	H	χ
$U(1)_{B-L}$	$\frac{1}{3}$	$\frac{1}{3}$	$\frac{1}{3}$	-1	-1	-1	0	0	0	0	0	2

Table 3.1: The $B-L$ charge for the particle content of the $B-L$ model.

pared to the previously existing file, we have written this file using the syntax of `FeynRules` version v.1.6.2 and above, enabling it to output an UFO file. This model file and its output UFO file will be implemented for a full Monte Carlo simulation in this thesis.

3.1 Particle content and Lagrangian of the $B-L$ gauge model

The $B-L$ gauge model, compared to the particle content of the SM, has an additional Abelian gauge field B'_μ, a singlet scalar filed χ and three RH neutrinos ν_{iR}. It obeys the local symmetry of $SU(3)_C \times SU(2)_L \times U(1)_Y \times U(1)_{B-L}$ where the $B-L$ charge of the SM fermions is defined through their baryon numbers minus lepton numbers. The SM bosons G, W, B and H are uncharged under $B-L$, while the $B-L$ charge of the additional exotic particles are given by $Y_{B-L}(\chi) = 2$, $Y_{B-L}(B') = 0$ and $Y_{B-L}(\nu_{iR}) = -1$ as summarised in Tab. 3.1.

The SM quantum numbers are defined as before, with all exotic fields being singlets under the SM gauge fields. In the following discussion, we list the full Lagrangian of the model [22, 149],

$$\begin{aligned}
\mathscr{L}_{\text{B-L}} =& \mathscr{L}_{\text{SM}} \\
& - \frac{1}{4} F'^{\mu\nu} F'_{\mu\nu} \\
& + \sum_{j=e,\mu\tau} \left(i\overline{\nu_{jR}} \gamma_\mu D^\mu \nu_{jR} \right) \\
& + (D^\mu \chi)^\dagger (D_\mu \chi) + m_\chi^2 |\chi|^2 - \lambda_2 |\chi|^4 - \lambda_3 H^\dagger H |\chi|^2 \\
& + \sum_{i,j=e,\mu,\tau} \left(-y^\nu_{ij} \overline{l_{iL}} \tilde{H} \nu_{jR} - y^M_{ij} \overline{(\nu_{iR})^c} \chi \nu_{jR} \right) + h.c.,
\end{aligned} \tag{3.1}$$

where $F'^{\mu\nu}F'_{\mu\nu}$ is the additional $B-L$ kinetic term for the gauge sector,

$$F'_{\mu\nu} = \partial_\mu B'_\nu - \partial_\nu B'_\mu. \tag{3.2}$$

We assume the kinematic mixing term $F'^{\mu\nu}F_{\mu\nu}$ to vanish as discussed below.

The term $\sum_{j=e,\mu\tau}(i\overline{\nu_{jR}}\gamma_\mu D^\mu \nu_{jR})$ represents the fermion Lagrangian of the $B-L$ model, containing an additional term for the RH neutrinos and the additional Abelian gauge field B'_μ. The covariant derivative D_μ of the model is defined as

$$D_\mu = D_{\mu,\mathrm{SM}} + i(\tilde{g}Y + g_{B-L}Y_{B-L})B'_\mu, \tag{3.3}$$

where B'_μ is the gauge field for the additional $U(1)_{B-L}$ group with gauge coupling g_{B-L} and the $B-L$ quantum number Y_{B-L}.

As we do not require gauge unification at some specific energy scale, the gauge couplings $\tilde{g}$ and g_{B-L} are free parameters. In the rest of the thesis, we however focus on the $B-L$ gauge coupling g_{B-L}, i.e. a minimal scenario with $\tilde{g} = 0$ at the EW scale. It is important to highlight that this condition holds at a given scale only: The running of $\tilde{g}$ due to quantum effects will necessarily introduce small loop-suppressed corrections in this case [149, 150]. If the $\tilde{g}$ is not fixed to zero, the introduction of the kinetic mixing will introduce changes to the EW precision observables, therefore it is constrained as $\tilde{g} \lesssim 10^{-2}$ from the EW precision tests (EWPT) at the Large Electron-Positron collider (LEP) [151–153].

Compared to the SM, the scalar sector of the $B-L$ model Lagrangian adds additional terms for the singlet scalar χ,

$$\mathscr{L}_{\text{B-L scalar}} = (D^\mu H)^\dagger (D_\mu H) + (D^\mu \chi)^\dagger (D_\mu \chi) - V(H,\chi). \tag{3.4}$$

Here, H is the SM Higgs doublet and the scalar potential $V(H,\chi)$ is expressed by

$$\begin{aligned} V(H,\chi) &= -\mu^2 H^\dagger H - m_\chi^2|\chi|^2 + \begin{pmatrix} H^\dagger H & |\chi|^2 \end{pmatrix} \begin{pmatrix} \lambda_1 & \frac{\lambda_3}{2} \\ \frac{\lambda_3}{2} & \lambda_2 \end{pmatrix} \begin{pmatrix} H^\dagger H \\ |\chi|^2 \end{pmatrix} \\ &= -\mu^2 H^\dagger H - m_\chi^2|\chi|^2 + \lambda_1 (H^\dagger H)^2 + \lambda_2 |\chi|^4 + \lambda_3 H^\dagger H |\chi|^2. \end{aligned} \tag{3.5}$$

Finally, the last line of Eqn. (3.1) gives the additional Yukawa terms for the neutrino fields

$$\mathscr{L}_{\text{B-L Yukawa}} = \mathscr{L}_{\text{SM Yukawa}} + \sum_{i,j=e,\mu,\tau} \left(-y^\nu_{ij}\overline{l_{iL}}\tilde{H}\nu_{jR} - y^M_{ij}\overline{(\nu_{iR})^c}\chi\nu_{jR}\right) + h.c.. \tag{3.6}$$

3.2 Spontaneous $B-L$ breaking

We have shown the full Lagrangian of the $B-L$ model in the previous section. Similar to the SM, the scalar potential V can be spontaneously broken in its vacuum $\langle\chi\rangle \equiv \frac{\tilde{x}}{\sqrt{2}}$. After diagonalization of the mass matrix, two mass eigenstates $h_{1,2}$ and the Higgs mixing angle $\sin\alpha$ are obtained, and the kinetic term for χ will generate a mass for the Z'. A Majorana mass term for the RH neutrinos ν_{iR} after the breaking of $B-L$ symmetry, and the Dirac mass term after EW symmetry breaking will be generated, giving rise to a seesaw mechanism for the light neutrinos.

We start with expanding the scalar fields around their minimum in the Feynman gauge,

$$H = \frac{1}{\sqrt{2}} \begin{pmatrix} -i(w^1 - iw^2) \\ h + v + iz \end{pmatrix}, \quad \chi = \frac{h' + \tilde{x} + iz'}{\sqrt{2}}, \tag{3.7}$$

where $v \simeq 246$ GeV [132] and $\tilde{x} \sim$ TeV as we focus on scenarios where the $B-L$ symmetry breaking is still accessible at the LHC. Here, $w^{1,2}, z$, and z' are the Nambu-Goldstone bosons [154, 155] corresponding to the generators of $SU(2)_L$ and $U(1)_{B-L}$, which are later 'eaten' by the gauge fields, as they are transformed into the longitudinal components of the vector bosons to give them masses.

In the unitary gauge, Eqn. (3.7) simplifies to

$$H \equiv \begin{pmatrix} 0 \\ \frac{h+v}{\sqrt{2}} \end{pmatrix}, \qquad \chi \equiv \frac{h' + \tilde{x}}{\sqrt{2}}. \tag{3.8}$$

In order for spontaneous symmetry breaking to happen, the minimum of the potential V should be away from zero, $\frac{\partial V}{\partial \chi} = 0$ for $\chi \neq 0$. Also, V should be bounded from below, i.e. $V(H,\chi)$ increases for $H, \chi \to \infty$. This can be trivially achieved by requiring $-m_\chi^2 < 0$ and $\lambda_{1,2,3} > 0$. However, we can extend the parameter space by diagonalising the quartic terms and requiring all couplings after diagonalization to be above zero. This simply means that the matrix in the first line of Eqn. (3.5) is positive-definite such that

$$\begin{aligned} 4\lambda_1\lambda_2 - \lambda_3^2 &> 0, \\ \lambda_1, \lambda_2 &> 0. \end{aligned} \tag{3.9}$$

This condition does not necessarily satisfy the requirement of physical values of v and $\tilde{x}$, such that v and $\tilde{x}$ are real and positive, therefore $v^2 > 0$ and $\tilde{x}^2 > 0$. In order to get physical solutions, from the requirement of non-zero extrema of V to exist, by definition

$$\frac{\partial V}{\partial H}\bigg|(v,\tilde{x}) = v\left(-\mu^2\lambda_1 v^2 + \frac{\lambda_3^2}{2}\tilde{x}^2\right) = 0, \tag{3.10}$$

$$\frac{\partial V}{\partial \chi}\bigg|(v,\tilde{x}) = \tilde{x}\left(-m^2\lambda_2 \tilde{x}^2 + \frac{\lambda_3^2}{2}v^2\right) = 0. \tag{3.11}$$

The above equations yield

$$v^2 = \frac{\lambda_2\mu^2 - \frac{\lambda_3}{2}m_\chi^2}{\lambda_1\lambda_2 - \frac{\lambda_3^2}{4}}, \tag{3.12}$$

$$\tilde{x}^2 = \frac{\lambda_1 m_\chi^2 - \frac{\lambda_3}{2}\mu^2}{\lambda_1\lambda_2 - \frac{\lambda_3^2}{4}}. \tag{3.13}$$

As the denominators are always positive from Eqn. (3.9), the numerators are forced to be positive in order to guarantee a positive-definite non-vanishing real solution for v and $\tilde{x}$.

We can obtain the masses of the Higgs fields after symmetry breaking by diagonalising the mass matrix of H and χ in the scalar potential as shown in Eqn. (3.5),

$$m^2_{h_{1(2)}} = \lambda_1 v^2 + \lambda_2 \tilde{x}^2 - (+)\sqrt{(\lambda_1 v^2 - \lambda_2 \tilde{x}^2)^2 + (\lambda_3 \tilde{x} v)^2}. \tag{3.14}$$

Here we choose $m_{h_1} < m_{h_2}$, and h_1 is the SM-like Higgs state such that $m_{h_1} = m_{h_{SM}} \approx 125$ GeV, and h_2 is the additional heavy Higgs state.

The mass eigenstates h_1, h_2 are related to the gauge states (H, χ) by a simple $SO(2)$ transformation,

$$\begin{pmatrix} h_1 \\ h_2 \end{pmatrix} = \begin{pmatrix} \cos\alpha & -\sin\alpha \\ \sin\alpha & \cos\alpha \end{pmatrix} \begin{pmatrix} H \\ \chi \end{pmatrix}. \tag{3.15}$$

The Higgs mixing angle $-\frac{\pi}{2} < \alpha < \frac{\pi}{2}$ is given by

$$\tan 2\alpha = \frac{\lambda_3 \tilde{x} v}{\lambda_1 v^2 - \lambda_2 \tilde{x}^2}. \tag{3.16}$$

Thus the scalar couplings $\lambda_1, \lambda_2, \lambda_3$ can be expressed in terms of the Higgs mixing angle α, the Higgs masses m_{h_1}, m_{h_2} and the VEVs $\tilde{x}, v$ following Eqn. (3.14) and (3.16),

$$\begin{aligned} \lambda_1 &= \frac{1}{4v^2}[(m^2_{h_1} + m^2_{h_2}) - \cos 2\alpha (m^2_{h_2} - m^2_{h_1})] = \frac{m^2_{h_1}}{2v^2}\cos^2\alpha + \frac{m^2_{h_2}}{2v^2}\sin^2\alpha, \\ \lambda_2 &= \frac{1}{4\tilde{x}^2}[(m^2_{h_1} + m^2_{h_2}) + \cos 2\alpha (m^2_{h_2} - m^2_{h_1})] = \frac{m^2_{h_1}}{2\tilde{x}^2}\sin^2\alpha + \frac{m^2_{h_2}}{2\tilde{x}^2}\cos^2\alpha, \\ \lambda_3 &= \frac{1}{2v\tilde{x}}[\sin 2\alpha (m^2_{h_2} - m^2_{h_1})]. \end{aligned} \tag{3.17}$$

For the gauge bosons masses, we expand the scalar kinetic terms around the minimum. In addition to the SM case in Eqn. (2.19), there is a term corresponding to the Z' mass,

$$(D^{\mu}\chi)^{\dagger}(D_{\mu}\chi) = \frac{1}{2}\partial^{\mu}h'\partial_{\mu}h' + \frac{1}{2}(h'+\tilde{x})^2(g_{B-L}2B'^{\mu})^2. \tag{3.18}$$

So that it is trivial to derive

$$m_{Z'} = 2\tilde{x}g_{B-L}. \tag{3.19}$$

As we assume no mixing between Z and Z', the tree-level masses of $A, Z, W^{\pm}$ are not affected,

$$m_A = 0, \tag{3.20}$$

$$m_W = \frac{gv}{2}, \tag{3.21}$$

$$m_Z = \frac{v}{2}\sqrt{g^2+g_1^2}. \tag{3.22}$$

The masses of neutrinos will be generated in the Yukawa sector of the Lagrangian after the spontaneously symmetry breaking. The mass matrix in Eqn. (2.47) will then contain the terms $M_R = y^M\tilde{x}$ and $M_D = y^{\nu}v/\sqrt{2}$. The light neutrino masses will be generated accompanying the additional heavy neutrinos via a Type-I seesaw as shown in Eqn. (2.49).

As neutrinos are no longer massless, the mass matrix for the leptons are not diagonal in general. We take no mixing among flavours for simplicity, and the generations decouple. Therefore, according to the Type-I seesaw mechanism Eqn. (2.53), $m_{\nu_{l_i}}$ is related to the neutrino mixing and the heavy neutrino mass by $m_{\nu_{l_i}}$=$V_{lN_i}^2 m_{N_i}$, as there are no off-diagonal terms. We thus obtain a diagonal Yukawa coupling matrix and we can express it as (i =1, 2, 3)

$$y_{ii}^{\nu} = \frac{\sqrt{2m_{N_i}m_{\nu_i}}}{v} = \frac{\sqrt{2}m_{N_i}V_{lN_i}}{v}, \tag{3.23}$$

via Eqn. (2.49) and (2.53), where V_{lN_i} is the active-sterile mixings for a given generation, i.e. V_{eN_1}, $V_{\mu N_2}$ and $V_{\tau N_3}$. In the rest of the thesis, we will however concentrate on the second generation and omit N_i as N, i.e. we only consider $V_{\mu N}$.

3.3 Theoretical considerations for the parameter space

After the $B-L$ gauge model is introduced, there are conditions on its parameter space from theoretical considerations. We require the vacuum to be stable and the couplings to be perturbative at the EW scale and possibly higher scales by running the Renormalisation Group Equations (RGEs). Additional constraints can come from W boson mass corrections in next-to-leading order (NLO).

Vacuum stability and perturbativity constraints: From Eqn. (3.9), we have already given the condition for the vacuum to be stable. Perturbativity further requires $|\lambda_i| < 1$ or $\frac{|\lambda_i|}{4\pi} < 1$ [45], $i = 1,2,3$, and similarly for other couplings as well, $y^M \equiv \frac{m_{N_i}}{\tilde{x}} < 1$ and $g_{B-L} < 1$ [156].

Besides, perturbative unitarity also gives a much weaker limit on the exotic Higgs mass [149],

$$m_{h_2} < 2\sqrt{\frac{2}{3}}\frac{m_W}{\sqrt{\alpha_W}\sin\alpha}, \tag{3.24}$$

with a relatively large Higgs mixing such as $\sin\alpha \gtrsim 0.1$, and $\alpha_W = \frac{m_W^2}{\pi v^2}$. We omit this limit in the following theoretical constraints as it is too weak compared to other limits.

Renormalization group evolution: In quantum field theory, renormalization is introduced to address the problem of infinities. The procedure cancels out the infinities of the bare and counter terms to renormalize the physical parameters. However, the renormalized parameters then depend on the energy scale of a given process. This behaviour is described by the so-called RGEs.

By matching the parameters at the EW scale, then evolving them according to the renormalization group equations of the $B-L$ model (see Appendix B), we can calculate the maximal scale $Q > Q_{\text{EW}}$ for the model to sustain the vacuum stability and pertubativity conditions. Although, this also means that we assume the $B-L$

model to be the only new physics beyond the SM. We use this condition to indicate the interesting parameter space albeit with strong theoretical bias.

W **boson mass:** New physics will introduce corrections to the SM via quantum corrections, specifically corrections for the W boson mass from radiative effects of the exotic Higgs. The general radiative effect is indicated by the parameter Δr characterised by the Fermi constant G_F, the fine structure constant α_{EW} and the EW renormalised gauge boson masses m_W and m_Z [46],

$$m_W^2 \left(1 - \frac{m_W^2}{m_Z^2}\right) = \frac{\pi \alpha_{\text{EM}}}{\sqrt{2} G_F}(1 + \Delta r). \tag{3.25}$$

The radiative effect from the SM is Δr = 0.038 which gives m_W = 80.360 GeV [46], compared to the tree level value m_W^{tree} = 80.94 GeV [46] and the theoretical uncertainty is 4 MeV [157], mainly from the top mass uncertainty [158]. However, there is some small discrepancy between theory and experiment possibly, as m_W^{exp} = (80.385 ± 0.015) GeV [159–161], therefore $\left|m_W^{\text{exp}} - m_W\right| \approx 20$ MeV $>$ 15 + 4 MeV.

This could be reconciled in new physics scenarios with additional mass corrections of the W boson mass at the loop level. This gives an additional shift,

$$\Delta m_W = -\frac{1}{2} m_W \frac{\sin^2 \theta_W}{\cos^2 \theta_W - \sin^2 \theta_W} \delta(\Delta r), \tag{3.26}$$

where $\delta(\Delta r)$ is dependent on m_{h_2} and $\sin\alpha$ in our model [46]. Both scenarios such as $m_{h_1} = m_{h_{\text{SM}}} \approx 125$ GeV $< m_{h_2}$ and $m_{h_1} < m_{h_2} = m_{h_{\text{SM}}} \approx 125$ GeV can resolve the discrepancy [46]. We omit the latter possibility and use the former condition, requiring the calculated m_W is within 2σ of the experimental value to yield a constraint on the m_{h_2} and $\sin\alpha$ parameter space. On the other hand, although omitted in this thesis, the $m_{h_1} < m_{h_2} = m_{h_{\text{SM}}} \approx 125$ condition is interesting as it can lead to processes such as $h_1 \to h_2 h_2$ when this process is kinematical possible, and this condition is constrained by the LEP experiment [162].

In Chapter 6, we will discuss the numeric impact of the above theoretical considerations for some benchmark scenarios to give the interesting parameter space.

Chapter 4

LHC Phenomenology of the $B-L$ Model

After the introduction and theoretical considerations of the $B-L$ gauge model, it is interesting to search for its signals. There are a variety of experiments which can constrain the parameter space of the model as will be discussed in Chapter 5. Among them, the LHC, at which the highest energy searches are performed, provides one of the best approaches to probe BSM scenarios such as the $B-L$ model under consideration. In this chapter, we will briefly introduce the LHC and its properties regarding beam acceleration, detectors and analysis, followed by the potential phenomenology for the $B-L$ gauge model at the LHC.

4.1 The LHC and its properties

The LHC at CERN is the world's largest and most powerful particle collider. It has a 27 kilometre ring of superconducting magnets inside a tunnel which lies as deep as 175 metres beneath the surface with a number of accelerating structures to boost the particles inside it [163].

The collider has two beams travelling in opposite directions inside two adjacent parallel beamlines. The beams intersect at four points around the ring where the partons in protons collide, the so-called interaction points (IPs). Initially, the LHC ran with an energy of 3.5 TeV per beam. After upgrades, it reached 6.5 TeV per beam or equivalently 13 TeV total collision energy. It will finally reach 14 TeV of total collision energy [163].

Currently, the LHC has seven detectors in total, the CMS (Compact Muon Solenoid) [164] and ATLAS (A Toroidal LHC ApparatuS) [165] detectors for general purpose physics, the LHCb (LHC-beauty) detector for B-physics *CP* violation measurements [166], the ALICE (A Large Ion Collider Experiment) detector for the study of the quark-gluon plasma [167], and three smaller detectors, TOTEM (Total Cross Section, Elastic Scattering and Diffraction Dissociation) [168], MoEDAL (Monopole and Exotics Detector At the LHC) [169] and LHCf (LHC-forward) [170] for specialised research. We focus on the CMS, ATLAS and LHCb detectors in the following. CMS and ATLAS have a similar physics purpose, both built as a backup and cross-check for each other, designed by independent teams making different compromises. As a result, the two detectors differ somewhat in their capabilities. They have similar structures, containing a vertex detector, tracker, electromagnetic calorimeter (ECAL), hadronic calorimeter (HCAL), magnets and muon chambers in a shell configuration [171,172]. The vertex detector is used to measure the particle trajectories close to the IP to precisely separate primary and secondary vertices. The tracker is used to determine the momentum of a particle by tracking its path through a magnetic field. The ECAL and HCAL are used to measure the energies of electrons and photons, and hadrons, respectively. The muon chambers are designed to identify muons and measure their momenta. It is placed at the very edge of the experiment where muons are the only particles likely to register a signal. ATLAS uses liquid Argon for the ECAL, while CMS uses crystal PbWO4. The resolution of the HCAL at ATLAS is better, while CMS wins on the ECAL [164,165]. The geometry of the CMS and ATLAS detectors with their layers of different subsystems can be simplified for our discussion as shown in Fig. 4.1. The regions defined in the figure are for the purpose of detecting the signatures of displaced vertex which will be introduced later.

The LHCb detector consists of a vertex locator (VELO), ring imaging Cherenkov detectors (RICH-I and RICH-2) for tracking, ECAL and HCAL, and muon system, each with similar function as that in CMS and ATLAS [173].

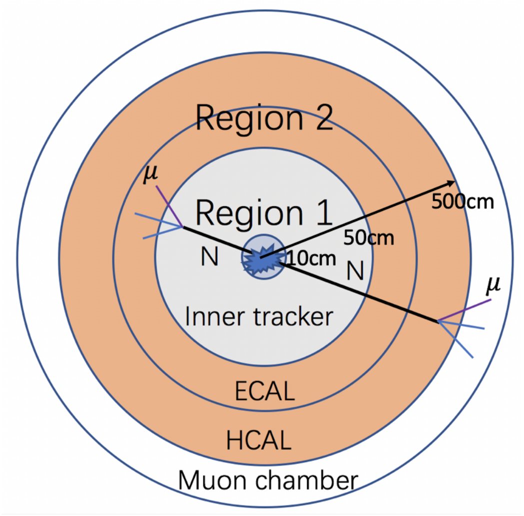

Figure 4.1: Illustration of the simplified geometry of a typical detector we consider in the thesis. The innermost dark grey region is the vertex detector. The silicon tracker in light grey defines Region 1. The electromagnetic calorimeter (ECAL) and hadronic calorimeter (HCAL) outside the inner tracker and inside the muon chamber define Region 2.

The detectors measure the individual hits and energy in the calorimeter system. The LHC has been colliding proton bunches every 25 ns and the detectors have been collecting data at a rate of 40 MHz. Due to the large computing resources required to process and store each event, it is not possible to record all events. The trigger system comes to rescue for this problem. It only collects the key information, and reduces the event rate to a manageable order. Then the data will be processed for event reconstruction, to reconstruct the triggered data into lists of particles which actually passed through the detector.

The trajectory of charged particles that pass through the vertex detector can be reconstructed using hits. The momentum of the charged particle can be determined from the magnitude of the track curvature caused by the solenoid magnet. The jets, b-jets, electrons and muons are reconstructed by the corresponding algorithms using the information in the calorimeter system. For example, jets are built using jet reconstruction algorithms [174] from the topological clusters of energy deposits in calorimeter cells at ATLAS [175]. Each jet constructed by the algorithm has a well defined four-momentum and set of constituents. From the conservation of momentum, the vectorial sum of the momentum in the transverse plane of the detector should be to zero. An imbalance of momentum in this plane is known as missing transverse momentum, and can arise from neutrinos, detector acceptance effects and mis-measured or unreconstructed objects.

The reconstructed events contain information such as the object ID such as electrons, muons, jets and missing transverse energy and the associated four-momentum vector. From the four-momentum vector, E which is the total energy, $p_T \equiv \sqrt{p_x^2 + p_y^2}$ which is the transverse momentum, $\eta \equiv \ln[\tan(\frac{\theta}{2})]$ which is the pseudorapidity reflecting the angle to the beamline θ, and ϕ the azimuthal angle is used to characterise events. The p_T information is important as the momentum along the beamline is affected by the unknown boost due to the parton distribution functions (PDFs) of quark and gluons.

We can derive information like the isolation $\triangle R \equiv \sqrt{(\triangle\phi)^2 + (\triangle\eta)^2}$ of a particle, where $\Delta\phi$ and $\Delta\eta$ are the differences between the azimuthal angle, and the pseudo-rapidity of a certain particle identified by the trigger and that of the reconstructed particle, respectively. Requiring the isolation to be small ensures the observed particle is related to the particle identified by the trigger. The invariant mass for a particle system, such as $M[jj]$ for the invariant dijet mass is also useful to identify the parent particle.

These data are used to perform a huge range of analyses, such as precision measurements of the SM parameters and processes, and searches for events with a certain signature which might lead to the discovery of new particles. A BSM model can potentially contribute to changes in measured SM quantities, and they are thus sensitive to new physics. In Chapter 6, we will use the LHC measurements to constrain the $B-L$ model. BSM models usually contain new particles which can lead to signatures containing certain final states, e.g. with high p_T which might come from the decay of a heavy BSM particle. When the final states are mostly leptons and they are originating from the main collision in the event, this is referred to as a prompt lepton search in the rest of the thesis. We will later see that the $B-L$ Z' boson can produce such a signal in Chapter 7.

A new particle might be weakly interacting with SM particles. It can then

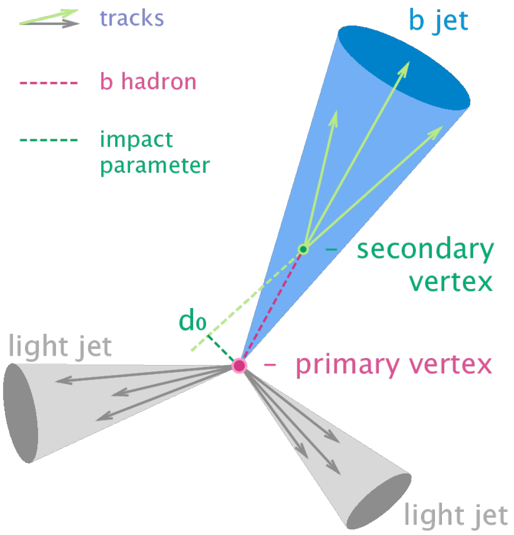

Figure 4.2: Schematic view a secondary vertex and displaced tracks, signature of a b-jet. Tracks are represented by arrows and the circles mark the primary (grey/blue) and secondary (dark grey/red) vertices. The impact parameter transverse distance d_0 which characterise the secondary vertex are indicated by green dashed lines. Take a b-jet as an example. Figure made by Nazar Bartosik (`https://commons.wikimedia.org/wiki/File:B-tagging_diagram.png`), `https://creativecommons.org/licenses/by/4.0/legalcode` [176].

be long-lived and decay at a distance from the IP, giving rise to the signature of a displaced vertex. This is defined as an event with charged tracks originating from a position displaced from the IP by a macroscopic distance. A search for such a signature is referred to as a displaced vertex search in the rest of the thesis. In Chapter 8, we will show that the heavy neutrinos in the $B-L$ model can be long-lived and give rise to the displaced vertex signature at the LHC.

Once a displaced vertex signature is established, we need to distinguish it from possible SM backgrounds. To identify a displaced vertex, additional cuts on the location of the vertex and the momentum of its particles can be required. This can include cuts on the impact parameter minimal transverse distance between the IP and tracks, which is defined as $|d_0| = |L_x p_y - L_y p_x|/p_T$. Here, L_x and L_y are the displacements of the vertex in the x and y transverse direction, and p_x, p_y, $p_T = \sqrt{p_x^2 + p_y^2}$ are the components of momentum and transverse momentum of a track emerging from the displaced vertex. This is illustrated in Fig. 4.2, taking the secondary vertex and displaced tracks from a b-jet as an example. The cut on d_0

ensures that the transverse distance between a final state particle track and the IP is larger than the resolution of the detector in the transverse distance σ_d^t to make sure the final states are produced via a displaced vertex. It may also be useful to cut directly on the minimal displacements in different directions such as $L_{xy} = \sqrt{L_x^2 + L_y^2}$ or L_z for the transverse or longitudinal displacement, and $r = \sqrt{L_x^2 + L_y^2 + L_z^2}$ for the radial displacement [177].

Before we introduce and perform analyses based on the aforementioned measurements and searches for the $B-L$ gauge model, we firstly introduce the general LHC phenomenology for this model.

4.2 Main LHC phenomenology

The $B-L$ model contains BSM features including Higgs mixing between the two Higgs, the $B-L$ boson Z' and three heavy neutrinos N_i. These additional features can lead to BSM processes at the LHC, e.g., $pp \to Z' \to l^+l^-, jj$, which have been widely searched at the LHC.

For example, searches for Drell-Yan Z' production with subsequent decays to jets, $pp \to Z' \to jj$ [178–180], to leptons, $pp \to Z' \to l^+l^-, l = e, \mu$ [181] and to muons, $pp \to Z' \to \mu^+\mu^-$ [182] have been performed at CMS and ATLAS. Likewise, searches for the exotic Higgs h_2 with various final states such as $pp \to h_2 \to WW$, ZZ, $b\bar{b}$, $\gamma\gamma$, $\tau\tau$, and $t\bar{t}$ have been performed at CMS and ATLAS, mainly looking for a heavier Higgs $m_{h_2} > m_{h_{\mathrm{SM}}} \approx 125$ GeV [71–74, 79]. Heavy neutrinos have been mostly searched for via their mixing to the light neutrinos from the decays of W and Z bosons with prompt [80–83, 88, 89] and displaced signatures [85–87]. Other processes predicted in the model are also searched for, and a summary of the current experimental searches and the resulting limits in the $B-L$ model will be discussed in Chapter 5.

However, there are still additional processes in the $B-L$ model which need to be explored, such as the production of the heavy neutrino N from the decay of the SM-like Higgs, $pp \to h_1 \to NN$ or Z', $pp \to Z' \to NN$. We briefly introduce the main LHC phenomenology in this subsection, while the detailed calculations and discussions for some of the processes in certain scenarios will be carried out in Chapters 6, 7 and 8.

From the full Lagrangian of the $B-L$ model as shown in Sec. 3.1, the main BSM signatures of the model can arise from the following vertices.

- $W\bar{l_L}l_L, B\bar{l_L}l_L$:
  $(-\frac{1}{2}\frac{e\sin\theta_\nu\sqrt{2}}{\sin\theta_W}\gamma^\mu\frac{1+\gamma^5}{2})W^+l^-N$,
  $(\frac{1}{2}\frac{e\sin\theta_\nu}{\cos\theta_W\sin\theta_W}\gamma^\mu\gamma^5)Z\nu N$, $(\frac{1}{2}\frac{e\sin^2\theta_\nu}{\cos\theta_W\sin\theta_W}\gamma^\mu\gamma^5)ZNN$,
- $H\bar{f}f$: $(-\frac{1}{2}\frac{em_f\cos\alpha}{m_W\sin\theta_W})h_1\bar{f}f$, $(-\frac{1}{2}\frac{em_f\sin\alpha}{m_W\sin\theta_W})h_2\bar{f}f$,
- $\chi B'B'$: $(-4\sin\alpha\; g_{B-L}\, m_{Z'})h_1Z'Z'$, $(-4\cos\alpha\; g_{B-L}\, m_{Z'})h_2Z'Z'$,
- $B'\bar{f}f$: $(-g_{B-L}Y_{B-L,f}\gamma^\mu)Z'\bar{f}f$,
- $\chi\nu_R\nu_R$:
  $(-2\cos\alpha\;\frac{m_\nu}{v}-\sin\alpha\;\frac{m_N}{\tilde{x}})h_1NN$,
  $(-2\sin\alpha\frac{m_\nu}{v}-\cos\alpha\;\frac{m_N}{\tilde{x}})h_2NN$,
  $(-2\sin\theta_\nu\cos\alpha\;\frac{m_N}{v}-\sin\theta_\nu\sin\alpha\;\frac{m_N}{\tilde{x}})h_1\nu N$,
  $(-2\sin\theta_\nu\sin\alpha\;\frac{m_N}{v}-\sin\theta_\nu\cos\alpha\;\frac{m_N}{\tilde{x}})h_2\nu N$,
  $(-2\cos\alpha\;\frac{m_\nu}{v}-\sin\alpha\;\frac{m_\nu}{\tilde{x}})h_1\nu\nu$,
  $(-2\sin\alpha\;\frac{m_\nu}{v}-\cos\alpha\;\frac{m_\nu}{\tilde{x}})h_2\nu\nu$.

Here we take $\cos\theta_\nu = 1$ as the active-sterile neutrino mixing is small $\theta_\nu < 10^{-2}$ (see review [183] and Sec. 5.3). The first two types of vertices are present for sterile neutrinos without $B-L$ extension. In the mass eigenstates, as ν_L and ν_R mix to give ν and N, $W\bar{l_L}l_L$, $B\bar{l_L}l_L$ can result in processes such as $N \to W^\mp l^\pm$, $N \to Z\nu$ with the subsequent decays of $W^\pm$ and Z. As H and χ mix to give $h_{1,2}$, therefore the production cross section of $pp \to h_1$ as well as its decay width is no longer the SM value, and h_2 can be produced similarly. Z' couples to fermions and bosons whose $B-L$ charge is nonzero leading to processes such as $pp \to Z'$, $pp \to h_{1,2} \to Z'Z'$, $pp \to Z \to Z'\mu^+\mu^-$ and the decay of Z' including $Z' \to NN$. The vertices of type $\chi\nu_R\nu_R$ give rise to processes $h_{1,2} \to NN$, $h_{1,2} \to N\nu$, and $h_{1,2} \to \nu\nu$ with the subsequent decays of N.

In summary, the potentially interesting signatures of the $B-L$ model at the LHC are:

- Production of h_2 via gluon fusion, $pp(gg) \to h_2$, with subsequent decay to weak bosons.
- production of h_2 via gluon fusion, with subsequent decay to Z'.
- Decay of the SM Higgs to Z' pairs, $pp \to h_1 \to Z'Z'$.
- Direct production of Z', $pp \to Z'$ (or for lower masses, multiple Z'), often in association with hadronic jets, and with subsequent Z' decay to leptons.
- Associated production of the h_2 or Z' with γ, W or Z.
- Heavy neutrino production via its mixing to the light neutrinos ν from the decays of W/Z bosons: $pp \to W^{\pm} \to Nl^{\pm}$ or $pp \to Z \to N\nu$.
- Heavy neutrino pair production (or single N production with a ν) via the SM-like Higgs, exotic Higgs or Z' decays, $pp \to h_{1,2} \to NN(\nu)$ or $pp \to Z' \to NN(\nu)$, and subsequent decays to $W^{\pm}$ (decays to jj and $l^{\pm}\nu$) $l^{\mp}$ or Z (decays to jj, l^+l^- and $\nu\bar{\nu}$) ν.
- Additional light neutrino pair production via the SM-like Higgs, exotic Higgs or Z' decays, $pp \to h_{1,2} \to \nu\nu$ or $pp \to Z' \to \nu\nu$, when the monojet emission is visible.

We will concentrate on the following.

Production of h_1 and h_2: As the mass eigenstates $h_1 = H\cos\alpha - \chi\sin\alpha$ from Eqn. (3.15), the couplings to h_1 for any SM particle are just $\cos\alpha$ times the corresponding SM couplings. Analogously, $h_2 = H\sin\alpha - \chi\cos\alpha$ from Eqn. (3.15). Therefore, h_2 couples to any SM particle via $\sin\alpha$. Thus, the production of $h_{1,2}$ is mainly from the mixing with the SM Higgs via gluon fusion. We can obtain the cross section of h_1 production at the 13 TeV LHC by [184],

$$\sigma(pp \to h_1) = \sigma(pp \to h_{\mathrm{SM}})\cos^2\alpha \approx \cos^2\alpha\,(44 \pm 4)\ \mathrm{pb}, \qquad (4.1)$$

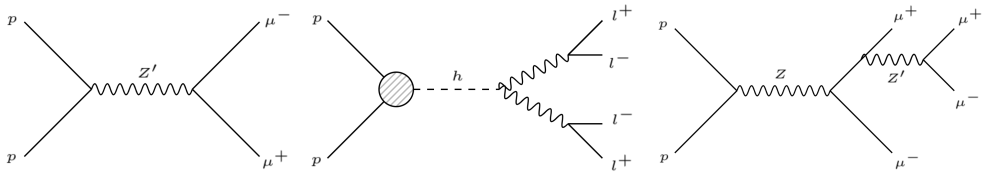

Figure 4.3: Feynman diagrams of Z' production modes follows with its decays to muon pairs including s-channel Drell-Yan $pp \to Z' \to \mu^+\mu^-$ (left), and Z' pair-production via SM Higgs $pp \to h_1 \to Z'Z' \to 4\mu$ (center), Z' final state radiation (FSR) from SM Z $pp \to Z \to Z'\mu^+\mu^- \to 4\mu$ (right).

while for the production of h_2, there is an additional factor to account for the different mass, an example of the study for its production can be found at Ref. [149]. Due to the mixing and its larger mass, the production cross section of h_2 is smaller than h_1 for at least three times and we hence focus on the production of h_1. The associated production of the $h_{1,2}$ with γ, W, Z is relatively small, hence is not discussed in this thesis.

Decay of h_1 and h_2: Similarly, $h_{1,2}$ can decay to SM particles via the Higgs mixing, e.g. $pp \to h_{1,2} \to l^+l^-$. As we have additional Majorana mass terms as shown in Eqn. (3.6), $h_{1,2}$ also couple to RH neutrinos via $\sin\alpha$ and the Yukawa coupling y^M. The RH neutrinos also mix to the mass eigenstates N_i via $\cos\theta_{\nu_i}$ where θ_{ν_i} is the neutrino mixings angle and $\sin\theta_{\nu_i} = V_{lN_i}$. As the active-sterile neutrino mixing is small $\theta_\nu < 10^{-2}$ (see review [183] and Sec. 5.3), we take $\cos\theta_\nu = 1$ and $V_{lN} = \sin\theta_\nu \approx \theta_\nu$. We can hence neglect $h_{1,2}N\nu$ ($h_{1,2} \to N\nu$ processes) and $h_{1,2}\nu\nu$ terms ($h_{1,2} \to \nu\nu$ processes) as $m_\nu \ll m_N$. We will discuss the possibility of h_1 decays to heavy neutrino pairs and the potential sensitivity at the LHC and its upgrade in detail in Sec. 8.4.1.

Additionally, $h_{1,2}$ can decay into Z' pairs, i.e., $pp \to h_{1,2} \to Z'Z'$, when $m_{Z'} < m_{h_{1,2}}/2$ as Z' can couple to $h_{1,2}$ via $h_1Z'Z'$ or $h_2Z'Z'$.

Production of Z': The Z' boson couples to any fermion via g_{B-L} and the corresponding $B-L$ charge. Thus it can be produced directly via s-channel Drell-Yan, $pp \to Z'$ (cf. Fig. 4.3 left). As mentioned above, it can also be produced from h_1, h_2 decays (cf. Fig. 4.3 center), so that their cross section is also controlled by the Higgs mixing $\sin\alpha$. Additionally, it can be produced from final state radiation such as $pp \to Z \to Z'\mu^+\mu^-$ (cf. Fig. 4.3 right). Apart from the above processes, Z' can also be produced associated with W/Z or a jet. The production cross section will however be smaller compared to the above processes. The production of the Z' will be introduced in detail in Sec. 7.1 for a light Z'.

Decay of Z': The Z' boson couples to any fermion including the heavy neutrino N_i. For each SM fermion generation, the partial width for different final states can be represented as [91]

$$\begin{aligned}\Gamma(Z' \to l_i\bar{l}_i) &\simeq 2\Gamma(Z' \to \nu_i\nu_i,\, N_iN_i) \simeq 3\Gamma(Z' \to q_i\bar{q}_i) \\ &= \frac{1}{3}\frac{g_{B-L}^2}{4\pi}m_{Z'}\left(1-\frac{4m_X^2}{m_{Z'}^2}\right)^{3/2},\end{aligned} \tag{4.2}$$

where X represents the fermion in the final state. [1]

When the Z' mass is relatively large, assuming only heavy neutrinos are not massless and neglecting any final states involving processes such as $Z' \to h_{1,2}h_{1,2}$, the total decay width of Z' can be approximated as

$$\Gamma(Z') \approx \left(2\times 3+1\times 3+(1/3)\times 2\times 5+3\times\left(1-\frac{4m_N^2}{m_{Z'}^2}\right)^{3/2}\right)\Gamma(Z' \to \nu_i\nu_i). \tag{4.3}$$

Here, the factor 2×3 represents 2 possible topologies and 3 generations of leptons while 1×3 corresponds to 3 generations of Majorana neutrinos. $(1/3)\times 2\times 5$ represents $1/3$ for the $B-L$ charge of quarks, and when Z' is relatively light, only five possible flavours of quarks are accessible except the top quark. $\left(1-\frac{4m_N^2}{m_{Z'}^2}\right)^{3/2}$ is the phase space factor for $Z' \to N\,N$ as we assume only the mass of N is comparative to Z' so that the phase space factor needs to be taken into account.

Nonetheless, the quark pairs in the final states will hadronize and form mesons. The decay width for certain $m_{Z'}$ can be then dominated by decays into mesons which are resonantly produced. This can be described in the Vector Meson Dominance (VMD) mechanism [185]. We will calculate the decay branching ratios of the Z'

---

[1] The factor of 2 for $\Gamma(Z' \to \nu_i\nu_i,\, N_iN_i)$ arises due to the Majorana nature of the neutrinos.

boson with `Darkcast` [31] which takes into account the effects of hadronization via VMD. Additionally, the decay $Z' \to N\nu$ via active-sterile mixing is also possible; it is however neglected as the active-sterile mixing is small.

The total decay width $\Gamma(Z')$ in general is a function of $m_{Z'}$ and g_{B-L}. For small g_{B-L} and $m_{Z'}$, the lifetime and thus the decay length of Z' can be macroscopic [186],

$$L_0(Z') \approx 1\ \mathrm{mm} \cdot \left(\frac{10^{-6}}{g_{B-L}}\right)^2 \cdot \left(\frac{1\ \mathrm{GeV}}{m_{Z'}}\right). \tag{4.4}$$

The branching ratios of Z' decays to various final states are shown in Fig. 4.4, where we include three generations of heavy neutrinos each with mass $m_N = 0.3 \times m_{Z'}$. For Z' heavier than 1 GeV, the branching ratios roughly remain constant except at the thresholds of $\tau\tau$ and $b\bar{b}$ at about 3.4 and 9.6 GeV, respectively. While for $Z' \approx 1$ GeV, two sharp peaks appear corresponding to the resonantly enhanced decays via η and Kaon mesons. Of special importance for our work is the branching ratio of Z' decaying to charged lepton pairs, which is approximately constant at 15% per generation for $m_{Z'} \gtrsim 10$ GeV.

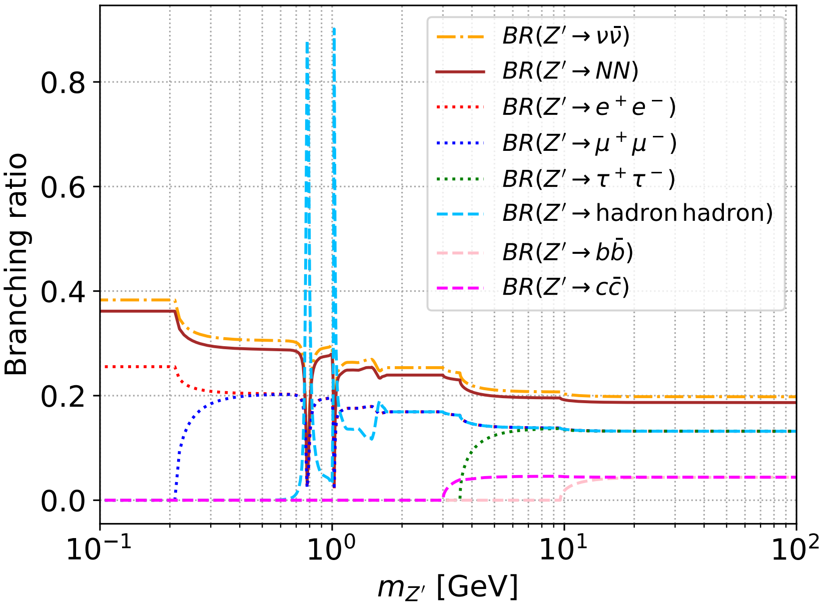

Figure 4.4: Branching ratios of Z' to different final states; here $\nu\bar{\nu}$ and NN represent the sum over all three light and heavy neutrinos in the final states, fixed $\frac{m_N}{m_{Z'}} = 0.3$ for all three generations of heavy neutrinos is assumed.

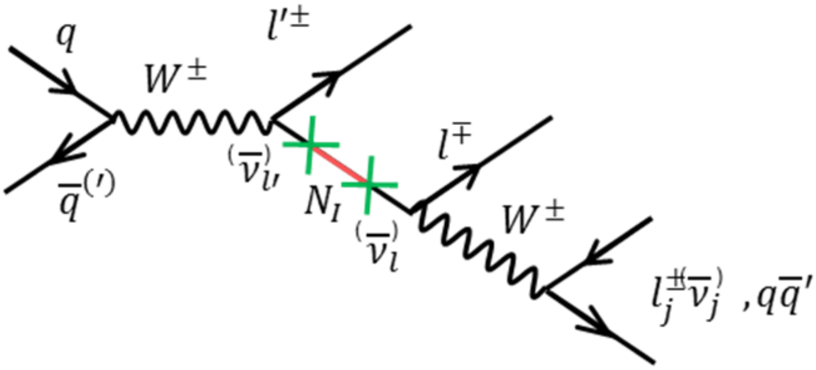

Figure 4.5: Feynman diagram of the heavy neutrino N production process $pp \to W^{\pm} \to l^{\pm}N$ followed with $N \to W^{\mp}l^{\pm}$. The figure is taken from the website `http://ep-news.web.cern.ch/content/hunting-right-handed-neutrinos-new-game-town` [187].

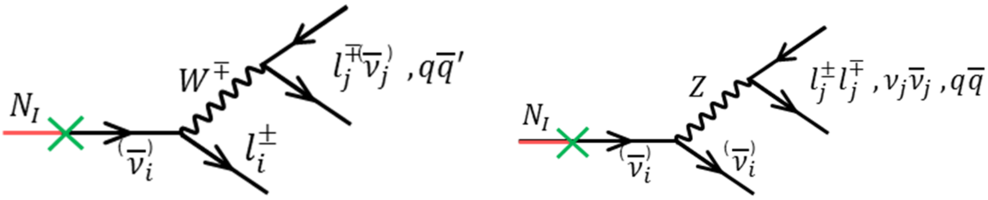

Figure 4.6: Feynman diagrams of the heavy neutrino N decays $N \to W^{\mp}l^{\pm}$ (left) and $N \to Z\nu$ (right). The figure is taken from the website `http://ep-news.web.cern.ch/content/hunting-right-handed-neutrinos-new-game-town` [187].

Heavy neutrino production Heavy neutrinos can be produced via neutrino mixing of light neutrino production such as $pp \to W^{\pm} \to l^{\pm}\nu$ as shown in Fig. 4.5. Similarly, it can be produced from $pp \to Z \to \nu\nu$. These production modes have already been searched for in many studies (see review [183]). The cross section of these processes is controlled by the square of the active-sterile mixing, and is thus negligible for small mixing. In Fig. 5.4, one can see that the sensitivity of these processes at the LHC cannot reach the seesaw regime.

However, in the $B-L$ gauge model, there are additional processes for the production of the heavy neutrinos which do not directly depend on the neutrino mixing. Such processes include the heavy neutrino production from the decays of $h_{1,2}$, $pp \to h_{1,2} \to NN$.

The heavy neutrinos can be additionally produced in Z' decays, $pp \to Z' \to NN$, if this channel is kinematically accessible. The neutrino couples to the Z'

boson via g_{B-L} with its $B-L$ charge equal to -1. The coupling of the $Z'NN$ vertex is simply $g_{B-L}\gamma^{\mu}\gamma^{5}$, and the production cross section is controlled by g_{B-L}^{2} and $m_{Z'}$. While it is not enhanced by gluon fusion, the cross section can still be sizeable when $m_{Z'} \ll m_{h_1}$. The process is discussed in detail in Sec. 8.1.

Heavy neutrino decay Heavy neutrinos, once produced, decay into SM particles via the active-sterile neutrino mixing. In principle, it can also decay into h_1, h_2 or Z' as well. However, we assume that heavy neutrinos are lighter than these particles and in any case the decay must be suppressed by the active-sterile mixing, e.g. $N \to Z'\nu$. If lighter than the W and Z, the heavy neutrino decays only via three body processes as shown in Fig. 4.6, $N \to l^{\mp}l^{\mp}\nu, l^{\mp}jj$ and $N \to l^{\pm}l^{\mp}\nu, \nu\bar{\nu}\nu, jj\nu$, and its decay width is approximately

$$\Gamma(N) \propto V_{lN}^{2} G_{F}^{2} m_{N}^{5}, \tag{4.5}$$

when $m_N \ll m_W$ [188], where G_F is the Fermi constant. In Sec. 8.1, we will use Monte Carlo tools to simulate and calculate the branching ratios (see Fig. 8.4) and the decay length. We will see that heavy neutrinos can lead to displaced vertices at the LHC.

Chapter 5

Experimental Constraints

As mentioned in Sec. 3.2, the $B-L$ model introduces three sectors of free parameters, i.e. the scalar sector, gauge sector and neutrino sector. From the potential LHC phenomenology mentioned in the last chapter, a wide range of constraints from existing experiments can be applied. For example, as the model contains an additional Higgs mass eigenstate mixing with the SM Higgs, searches such as for an extra Higgs [71–74] can give constraints on the scalar sector. The Higgs mixing also modifies the Higgs signal rate, therefore LHC Higgs production rate measurements are sensitive as well. In the gauge sector, a variety of Z' searches [50–53, 56, 57] can be applied to the model. Indirect bounds can also be obtained from recasting dark photon searches [31]. Heavy neutrinos and their mixing to the light neutrinos have been studied in many analyses through neutrino oscillation experiments, EW precision tests and direct RH neutrino searches (see review [189] and references therein). In this chapter, we will briefly summarise the existing experimental limits on the $B-L$ model.

5.1 Gauge sector

The gauge sector of the model contains an additional gauge boson Z' with associated $B-L$ gauge coupling g_{B-L} as shown in Sec. 3.1. Searches for the Z' thus probe the $m_{Z'}-g_{B-L}$ parameter space. Direct resonance searches for a heavy Z' with two lepton final states have been made since the Tevatron [41,48–50]. A summary of Tevatron's limits on $m_{Z'}$ and g_{B-L} is given in Ref. [190]. For Z' masses kinematically inaccessible at a given collider, such as LEP-II (209 GeV), effective four fermion contact interactions $\frac{g_{B-L}^2}{\Lambda^2}\bar{f}f\bar{f}f, \Lambda \sim m_{Z'}$ induce non-resonant processes such as $e^+e^- \to l^+l^-$. Therefore, limits on the contact coupling $\frac{g_{B-L}^2}{m_{Z'}^2}$ are achieved [50],

$$\frac{m_{Z'}}{2g_{B-L}} \equiv \tilde{x} \gtrsim 3 \text{ TeV}, \tag{5.1}$$

The Z' boson can also make additional contributions to EW observables, and limits are obtained based on the general analysis of EW precision data obtained from Large Electron-Positron Collider run 1 (LEP1), LEP2 and Stanford Linear Accelerator Center (SLAC) Large Detector (SLD). At 99% C.L. from EW precision limits [51,53],

$$\frac{m_{Z'}}{2g_{B-L}} \equiv \tilde{x} \gtrsim 3.5 \text{ TeV}, \tag{5.2}$$

and the $B-L$ breaking scale $\tilde{x}$ becomes the experimentally sensitive parameter. The above limits only apply for $m_{Z'}$ much above the EW scale, as the contact interactions are assumed only when $m_{Z'}$ is much larger than the energy of the LEP operating at the EW scale. In the LHC era, resonance searches for Drell-Yan processes $pp \to Z' \to l^+l^-$ show more stringent limits [54–59]. Recently, ATLAS and CMS analyses give a lower bound of $m_{Z'} \gtrsim 4.8$ TeV for a SM-like g_{B-L} coupling in narrow width approximation [58, 59]. Although the above limits yield bounds ruling out Z' lighter than $\approx$ TeV, this applies to SM-like coupling strength, $g_{B-L} \approx g_1$, and light Z' are still possible, as the coupling g_{B-L} can in principle be much smaller than the SM weak coupling. For Z' with masses below 10 GeV especially, non-perturbative effects become important and the factorization theorem is no longer applicable and the production should be dealt with via e.g. the VMD mechanism [186].

In general, for an exotic gauge boson with weak couplings to the SM fermions, current searches are mostly focused on dark photons as they are believed to be the bridge between the SM and a hidden dark sector. Dark photons mix with SM

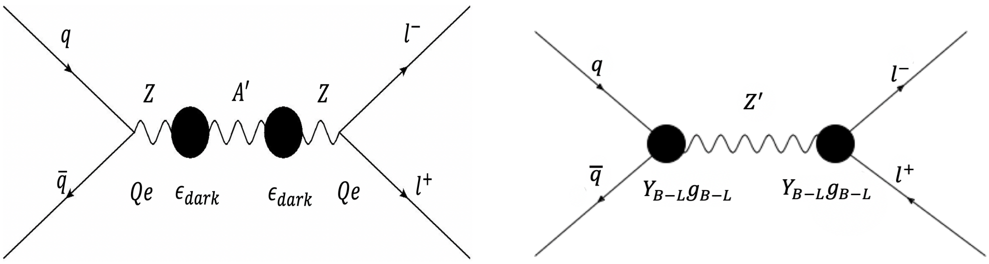

Figure 5.1: Feynman diagrams for $pp \to A' \to l^+l^-$ (left), and $pp \to Z' \to l^+l^-$ (right).

photons via a kinematic mixing $\varepsilon_{\text{dark}}$ [191],

$$\mathscr{L} = \frac{1}{2}\varepsilon_{\text{dark}} F^{\mu\nu,\text{EM}} F^{\text{dark}}_{\mu\nu}. \tag{5.3}$$

Here $F^{\mu\nu,\text{EM}}$ and $F^{\text{dark}}_{\mu\nu}$ are field strength tensors associated with the SM electromagnetic group $U(1)_{EM}$ and the dark $U(1)_{\text{dark}}$. Therefore, the dark photon A' interacts with SM particles described by,

$$\mathscr{L}_{\text{int}} = \varepsilon_{\text{dark}} e A'_{\mu} J^{\mu}_{EM}, \tag{5.4}$$

where J^{μ}_{EM} is the usual electromagnetic current, so that the A' couples to SM particles proportionally to their electric charges.

Searches for A' have been performed in both its leptonic decay channels $A' \to l^+l^-$ and hadronic decay channels $A' \to jj(\pi\pi)$. For example, LHCb has searched $pp \to A' \to l^+l^-$ for both prompt and long-lived dark photons [192]. The prompt search covers the mass range between the dimuon threshold and 70 GeV, setting upper limits $\varepsilon_{\text{dark}} \lesssim 10^{-3}$. The long-lived search is restricted to the low-mass region 214 MeV $< m_{A'} <$ 350 MeV with sensitivity close to $\varepsilon_{\text{dark}} \sim 10^{-4}$. The hadronic decay channel of A' has been searched for in KLOE for the process $e^+e^- \to A'\gamma$, $A' \to \pi^+\pi^-$ [193]. The search is able to set limits for $\varepsilon_{\text{dark}} \lesssim 10^{-3}$ for 527 MeV $\lesssim m_{Z'} \lesssim$ 987 MeV.

These limits can be recast to the $B-L$ model, as the $B-L$ gauge boson Z' can result in the same final states of the ones from the dark photon with same mass. In the most simplified case, such that $Br(Z' \to F) \approx Br(A' \to F)$ and the efficiency

$\varepsilon(Z') \approx \varepsilon(A')$ for $m_{Z'} = m_{A'}$, we can simply have the limits on g_{B-L} identifying $g_{B-L} = \frac{Qe\varepsilon_{\text{dark}}}{Y_{B-L}}$, where e is the elementary electric charge and Q is the electromagnetic charge number of the particle in question. For instance, as shown in Fig. 5.1, the processes $pp \to A' \to l^+l^-$ and $pp \to Z' \to l^+l^-$ have the same experimental signatures when $m_{A'} = m_{Z'}$, and the production cross sections are

$$\begin{aligned}\sigma(m_{A'}, \varepsilon_{\text{dark}}) &= \sigma(m_{A'})(Q_q e \varepsilon_{\text{dark}})^2, \\ \sigma(m_{Z'}, g_{B-L}) &= \sigma(m_{Z'})(Y_{B-L,q}\, g_{B-L})^2.\end{aligned} \tag{5.5}$$

Therefore, for $m_{Z'} = m_{A'}$, $g_{B-L} = \frac{Q_q e \varepsilon_{\text{dark}}}{Y_{B-L,q}}$.

However, this is not precise in general, as the full calculation done in Ref. [31] explicitly using

$$\sigma(Z')Br(Z' \to F)\varepsilon(Z')|(m_{Z'}, g_{B-L}) = \sigma(A')Br(A' \to F)\varepsilon(A')|(m_{A'}, \varepsilon_{\text{dark}}), \tag{5.6}$$

$Br(Z'/A' \to F)$ is the branching ratio of Z' or A' to the corresponding final states F and ε the corresponding experimental efficiency. So the limits on $\varepsilon_{\text{dark}}$ can be recast to the limits on g_{B-L} as a function of $m_{Z'} = m_{A'}$. The limits from invisible final states are derived by $Br(Z' \to NN) \simeq Br(Z' \to \text{invisible})$ for Z' decays to the heavy neutrinos N_i.

The results of the recast are shown in Fig. 5.2. To understand the limits, we will briefly introduce how the limits are obtained from different experiments.

BaBar The BaBar detector is part of the PEP-II B-factory [199] with a center-of-mass energy of 10.58 GeV. The BaBar collaboration searched for visible final states including both $Z' \to e^+e^-$ and $Z' \to \mu^+\mu^-$ where Z' is produced by the collision of e^+e^- [60, 61]. It also looked for invisible final states containing significant missing energy and momentum [200] from the mono-jet or mono-photon signature.

NA48/2 The NA48/2 experiment at the CERN SPS, collected decays of charged kaons ($K^\pm$). The $K^\pm$ can decay to π^0, and subsequently produce Z' via $\pi^0 \to Z'\gamma$. It then searched for visible final states such as $Z' \to e^+e^-$ [62].

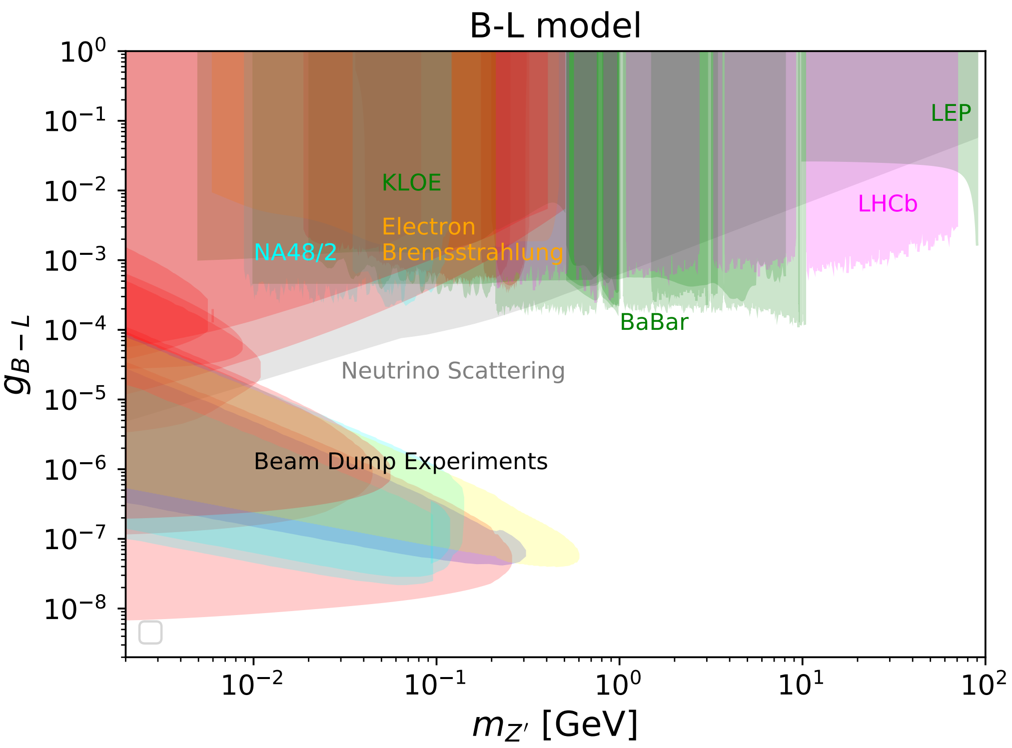

Figure 5.2: Current limits on the $m_{Z'} - g_{B-L}$ parameter space using `Darkcast`. The shaded areas represent the limits from electron beam dumps experiments (red), proton beam dumps experiments (yellow), e^+e^- colliders (green), pp collisions (magenta), meson decays (cyan and blue, including some proton beam dumps experiments), electron on fixed target experiments (orange), other limits including electron neutrino scattering experiments such as Borexino [194, 195], Texono [69, 196], CHARM-II [69, 70] and from SPEAR, DORIS, and PETRA [197, 198] are shown in grey. Both the visible and invisible final states are considered, and we take $Br(Z' \to NN) \approx Br(Z' \to \text{invisible})$.

Electron Bremsstrahlung The bremsstrahlung process occurs when an ultra-relativistic particle interacts with a strong electric or magnetic field. The limits from electron bremsstrahlung are shown as orange shaded regions in Fig. 5.2. The electron bremsstrahlung experiments include A1 [63], APEX [64] and NA64 [65, 66]. At the A1 and APEX experiments, the Z' can be produced via $e\mathscr{Z} \to e\mathscr{Z}Z'$ and then followed by the visible decay, $Z' \to e^+e^-$, where $\mathscr{Z}$ is a fixed nuclear target. The NA64 experiment, while having a similar production process, searched for invisible final states of Z'.

KLOE The KLOE detector is located at the e^+e^- collider DAΦNE, the Frascati ϕ-factory [201] (ϕ meson). Therefore, the Z' is produced via $\phi \to Z'\eta$, and followed by $Z' \to e^+e^-$ [67]. It can also be produced directly by e^+e^- such as $e^+e^- \to Z'\gamma$ and later followed by the decays $Z' \to \pi^+\pi^-$ [193] or $Z' \to e^+e^-$ [68].

LHCb has also searched for decays $Z' \to e^+e^-$ at the LHC, where the Z' is produced via $pp \to Z'$ [192].

Beam Dump experiments are fixed-target experiments which use detectors to look for decay products of rare penetrating particles behind a stopped particle beam. There are two kinds of beam dump experiments including the electron beams for E141, E137, E774, KEK, Orsay and the NA64 experiments, and the proton beams for $\nu - CAL\ I$, CHARM, NOMAD and PS191 experiments (see Ref. [31] and references therein).

At the electron beam dump experiments, Z' is produced via $e\mathscr{Z} \to e\mathscr{Z}Z'$ and then followed by $Z' \to e^+e^-$. As the detectors are at a macroscopic distance away from the target, they look for long-lived Z' with a decay length of the order of meters. This gives rise to the band-like shape of the limits in the bottom left corner of Fig. 5.2, as the detector size and its distance to the target sets the upper and lower bounds of g_{B-L} for Z' with masses smaller than 1 GeV, typically.

At proton beam dump experiments, similarly, Z' is produced via $P\mathscr{Z} \to P\mathscr{Z}Z'$, where $P = \pi^0, \eta$, or η', then followed by the decay $Z' \to e^+e^-$. The Z' is also required to be long-lived to be detectable.

LEP1 is the run 1 of the LEP as a Z-factory [202, 203]. It searched for the invisible decay of Z' produced from the $e^+e^- \to Z'\gamma$ process [204].

Neutrino Scattering There are additional limits from neutrino experiments via the measurements of the neutrino-electron and neutrino-nucleus scattering cross section from Borexino [194, 195], Texono [69, 196], CHARM-II [69, 70] and from SPEAR, DORIS, and PETRA [197, 198] as shown as the grey region, among which CHARM-II provides the most sensitive limits for $m_{Z'} \gtrsim 0.1$ GeV. They are not recast using `Darkcast`, but directly obtained from the experiments for the $B-L$ gauge model.

In summary, we can conclude that the upper limits for g_{B-L} can be roughly approximated as

- $g_{B-L} \leq 10^{-3}$ for $m_{Z'} > 10$ GeV,
- $g_{B-L} \leq 10^{-4}$ for 0.1 GeV $< m_{Z'} <$ 10 GeV.

The $m_{Z'} > 10$ GeV limit mainly from the LHCb dark photon searches. While for 0.1 GeV $< m_{Z'} <$ 10 GeV, the limit is dominated by CHARM-II .

There are also more recent limits from the LHC including a search for Z' final state radiation from Z production at CMS [205], a dilepton search at CMS [182] and a CMS high mass dilepton search [181]. We will discuss their details and limits in Chapter 7. Additionally, the Z' can be produced from SM-like Higgs decays $h_1 \to Z'$ when the Higgs mixing is nonzero and we can thus derive limits from four leptons searches [206, 207]. This possibility is going to be discussed in Chapter 7 as well.

5.2 Scalar sector

The scalar sector of the $B-L$ gauge model contains an additional Higgs mass eigenstate h_2 and the Higgs mixing $\sin\alpha$ between the SM-like Higgs state with the scalar singlet χ as shown in Sec. 3.1 and 3.2. These exotic features can lead to new phenomena at the LHC such as the modified production rate of the SM-like Higgs and the heavy Higgs state h_2 and their decays. The modified production rate of the SM-like Higgs can lead to deviations of the LHC measurements of the Higgs signal strength, and limits can be obtained from the tool HIGGSSIGNAL [208] using a χ^2 analysis [209–216]. The results are summarised in Refs. [27, 45, 46, 75–78] with an upper limit $|\sin\alpha| \lesssim 0.37$ for m_{h_2} from 150 GeV to 1000 GeV at LHC Run 2 with 95% C.L..

The heavy Higgs state h_2 can be searched for directly, and the non-observation yield limits for m_{h_2} and the Higgs mixing $\sin\alpha$ using HIGGSBOUNDS [217]. Direct searches at the LHC for an additional Higgs with final states such as WW and ZZ and their subsequent decays to $4l$, $2l2\nu$, or $2l2q$, $Z\gamma$, Zh_{SM} and with $Z \to b\bar{b}$ and

h_{SM} to different final states, $h_{SM}h_{SM}$ and decays to multiple final states, and $b\bar{b}$, $\gamma\gamma$, $\tau\tau$, $t\bar{t}$ directly from the additional Higgs decays, put limits on the exotic Higgs mass and the mixing to the SM Higgs. Summarising the direct LHC Higgs searches by combing the limits from different resonance searches gives upper limits $|\sin\alpha| \lesssim$ 0.20-0.60 depending on m_{h_2} [27,45,46,71–79].

The scalar sector of the $B-L$ gauge model also contains additional contributions in loops. Such loop effects are expected to contribute predominantly through vacuum polarization corrections to the EW precision observables which is characterised by the oblique parameters S, T and U [218–222]. Mainly from LEP or Tevatron, these limits give weaker upper limits $|\sin\alpha| \lesssim 0.60$ on the Higgs mixing [223]. The curve is not continuous because it combines different searches which has different sensitivities, final states, etc.

The limits including both the theoretical considerations in Sec. 3.3 and the above experimental limits are summarised in Fig. 5.3. In this figure, the VEV of the $B-L$ model is selected to be 10 times the electro weak scale $\tilde{x} = 2.46$ TeV. However, this choice only affects the perturbativity and EW observables limits, as they are rather weak, a different choice of the VEV would not make significant change to the results. At the lower end for the exotic Higgs masses, $m_{h_2} \in [130,300]$ GeV, the dashed green line which represents the direct exotic Higgs searches at the LHC provide the most sensitive limits. At higher masses, W boson mass constraint (see Sec. 3.3) gives the most powerful limits until $m_{h_2} \gtrsim 850 GeV$ where the limit from λ_1 perturbativity becomes more stringent.

Besides the above, there are new limits from recent and future studies. For example, searches at the LHC for a Higgs-like particle decaying into long-lived particles [224] have been studied, and the non-observation results indicate upper limits for its cross section. This information can provide corresponding limits for the process $pp \to h_1 \to NN$ in the $B-L$ model. Future colliders such as the high luminosity run of the LHC (HL-LHC) [225] and CEPC [226] can provide even more sensitive results from their Higgs signal strength measurements. CEPC especially, can already show a potential of a very powerful sensitivity as $\sin\alpha \lesssim 0.06$ via a

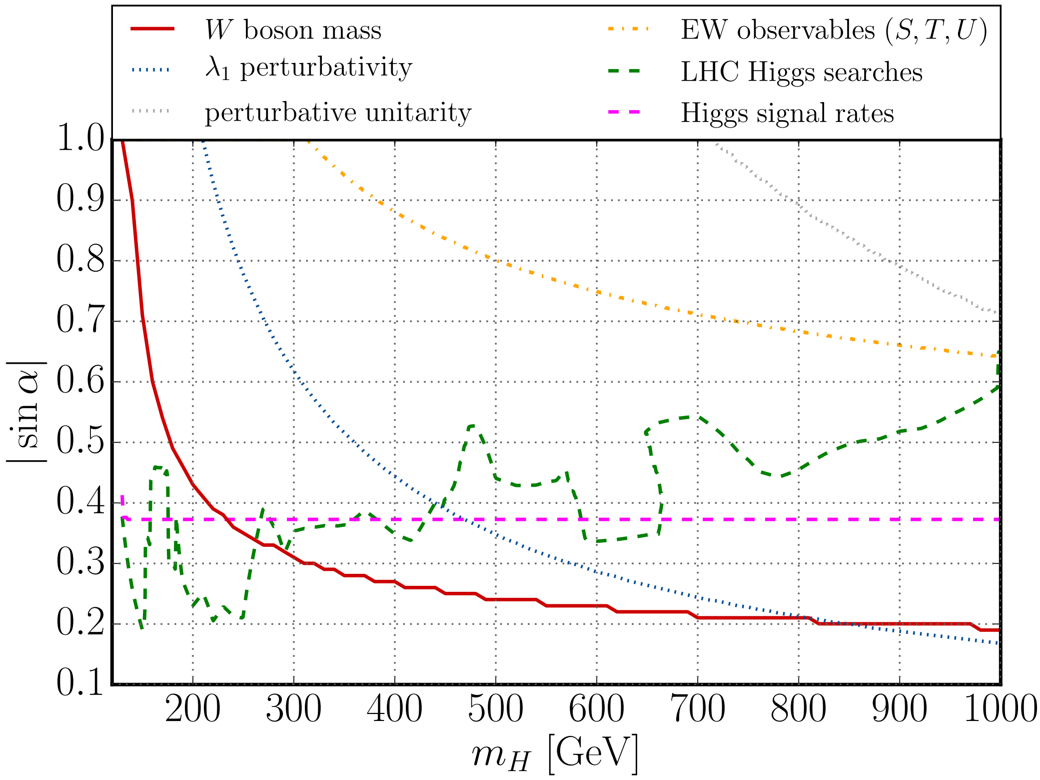

Figure 5.3: Constraints on the Higgs mixing $|\sin\alpha|$ as a function of the exotic Higgs mass m_{h_2} (indicated by m_H in this figure). The vacuum expectation value of the $B-L$ model is selected to be 10 times the electro weak scale $\tilde{x} = 2.46$ TeV (only affects the perturbativity and EW observables limits): Theoretical constraints from perturbativity of the couplings (dotted blue), perturbative unitarity (dotted gray), and constraints from the W boson mass correction (solid red), EW precision observables (dot-dashed orange), combined direct LHC Higgs searches for exotic Higgs bosons (dashed green) and LHC measurements of the Higgs signal rates (dashed magenta). Figure from Ref. [78].

simple χ^2 test for its measurement of the Higgs signal strength [227].

5.3 Neutrino sector

Heavy neutrino masses and their mixing to the light neutrinos can be probed in various experiments. While there exist two other heavy neutrinos in the model, we focus on one exclusively coupling to muons as we are interested in phenomena such as muons from a displaced vertex in the muon chamber of the LHC. Existing limits on the heavy neutrino mass m_N and its mixing $V_{\mu N}$ include those from direct collider searches, peak searches in meson decays, beam dump experiments, rare LNV decays of mesons, Z-decays and EW precision tests. Besides, neutrinoless double beta decay also provides limits on the heavy neutrino masses and mixing with the electron flavour. A complete review of the existing limits on heavy neutrino masses and active-sterile mixings for all three generations can be found eg. in Ref. [183] and [189]. In the following discussions, we give a brief summary.

Direct collider searches for heavy neutrinos can be performed at both lepton colliders as well as hadron colliders. At lepton colliders, a single heavy neutrino can be produced at LEP or LEP2 via its mixing with active neutrinos: $e^+e^- \to Z \to N\nu$, followed by its decay via neutral current (NC) or charge current (CC) interaction to the SM W, Z or Higgs bosons: $N \to lW, \nu Z, \nu H$ (see Sec. 4.2 and more details to be discussed in Sec. 8.1). These processes can lead to final states such as three charged fermions or even displaced vertices when the heavy neutrinos are long-lived. Searches for such processes have been performed at LEP and LEP2 and limits are obtained through reanalysis of data by the L3 [228] and DELPHI [229] collaborations. The proposed FCC-ee experiment as a high-luminosity Z-factory, will dramatically improve the sensitivity to $|V_{lN}|^2 \sim 10^{-12}$ for mixing with all flavours for 10 GeV $< m_N <$ 80 GeV due to its abundant production of Z boson [230, 231]. The limits on individual mixing parameters are derived from the corresponding limit on the sum of mixing $\Sigma_l |V_{lN}|^2$ assuming a normal hierarchy of light neutrinos [230].

At hadron colliders, heavy neutrinos can be produced from their mixing to light neutrinos via processes such as $pp(p\bar{p}) \to W^* \to Nl^\pm$. This can lead to the lepton-number violating process $Nl^\pm \to l^\pm l^\pm jj$ (see Fig. 4.6). An inclusive search for same-sign dilepton signals was first carried out at Tevatron [232] and such processes have also been searched for at the LHC for prompt decays [80–83, 88, 89]. Upper limits $V_{\mu N} \lesssim 10^{-2}$ are obtained for 1 GeV $< m_N <$ 1.2 TeV. When heavy neutrinos are long-lived, it can also lead to displaced vertex signatures. Such signatures can be approximately considered to be background free, thus several CMS or ATLAS searches [85–87] have been looking for displaced vertices which could come from heavy neutrinos decays. A combined search for both prompt and displaced signatures of heavy neutrinos has been performed at ATLAS [84] yielding $V_{\mu N} \lesssim 10^{-3}$ for $m_N < m_Z$.

EWPT Limits on the active-sterile mixing of neutrinos can also be obtained from EW precision data. This is due to the fact that the mixing can affect various EW observables such as the Z and Higgs invisible decay width, etc. in the SM [233–235]. The resulting non-unitary lepton mixing matrix [236–238] and violations of lepton universality in processes such as the leptonic and semileptonic decays of pseudoscalar mesons can also give bounds on the neutrino mixings [239–241]. For example, due to the presence of the active-sterile mixing, lepton universality can be violated. Therefore, the ratios such as $R_K \equiv \frac{\Gamma(K^+ \to e^+ \nu)}{\Gamma(K^+ \to \mu^+ \nu)}$ and $R_\pi \equiv \frac{\Gamma(\pi^+ \to e^+ \nu)}{\Gamma(\pi^+ \to \mu^+ \nu)}$ will no longer be the SM values. The shift of the ratios is characterised by functions of the active-sterile mixing V_{eN} and $V_{\mu N}$ and the masses of the heavy neutrinos m_{N_1} and m_{N_2} [239].

Meson Decays Heavy neutrinos can be produced in meson decays. For instance, searches for an additional peak in meson decays can probe heavy neutrino mixing with all lepton flavours. Among this, the two-body decays of mesons into leptons and neutrinos such as $X^\pm \to l^\pm N$ [242–244] are most promising. Searches have been performed for processes including $\pi \to eN$, $\pi \to \mu N$, $K \to eN$ and $K \to \mu N$ (see Ref. [183] and references therein). Three-body decay processes such as $B \to XlN$ have also been done at the Belle experiment [245].

Mesons can also decay via lepton number violation processes (LNV) such as $X_1^\pm \to l^\pm N$, $N \to l^\pm X_2^\mp$ [246] if heavy neutrinos are Majorana particles. Such decay modes have already been searched for at various flavour physics experiments including CLEO, Belle, BaBar and LHCb. Among them, the $K^+ \to l^+ l^+ \pi^-$ channel [188] gives the most stringent limits.

Beam Dump Experiments Heavy neutrinos are not stable and they are likely to decay at some distance when the mixing V_{lN} is small. Thus, the visible decay products can be searched by beam dump experiments when the detector is placed some distance away from the production site. Such searches have been performed at PS191 [247], NA3 [248], CHARM [249–251], IHEP-JINR [252], BEBC [253], FMMF [254], NuTeV [255] and NOMAD [256]. The proposed DUNE [257] experiment can also be sensitive to the active-sterile mixing.

The proposed fixed-target experiment SHiP [258] uses a high-intensity proton beam at the CERN SPS. The huge background due to multiparticle production inherent in hadron scatterings can be absorbed by adopting appropriate beam-dump techniques, thus allowing the sterile neutrinos to freely propagate into a decay volume. This experiment will improve the mixing sensitivity to $V_{lN} \lesssim 10^{-5}$ [183, 258].

Besides, neutrinoless double beta decay experiments are also sensitive to heavy neutrino masses and the active-sterile mixing. However, as double beta decay only probes heavy neutrinos mixing with the electron, we do not discuss this in detail in this thesis as we focus on the heavy neutrino which couples to the muon.

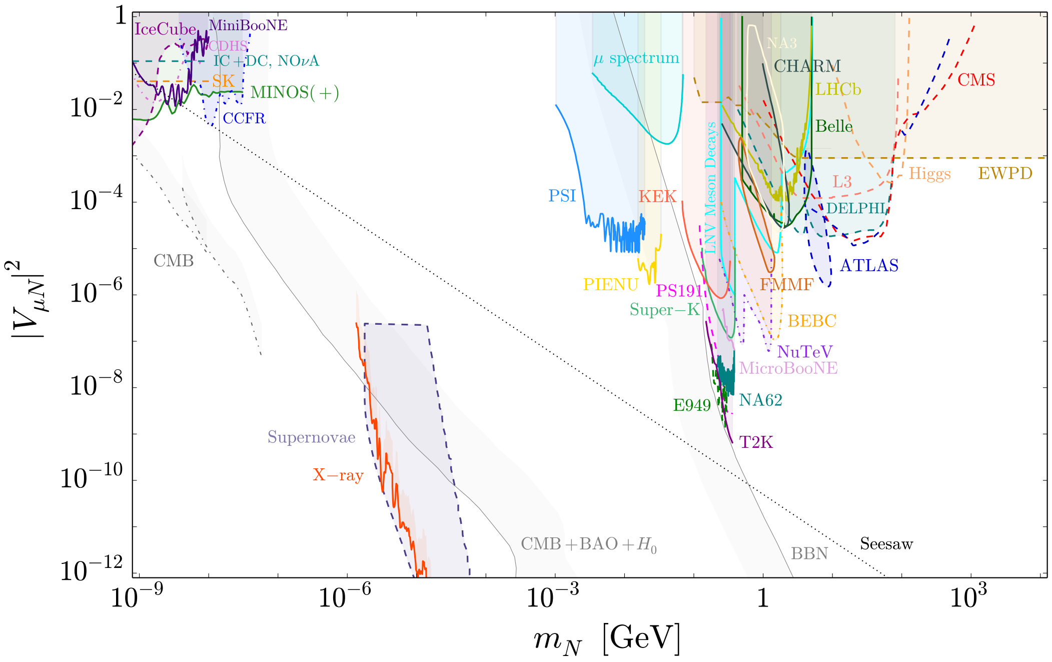

Figure 5.4: Current limits on the $m_N - V_{\mu N}$ parameter space. The shaded regions are excluded by the searches listed in the text. Figure from Ref. [189].

The existing limits on the heavy neutrino mass and neutrino mixing with the second generation are shown in Fig. 5.4. The expected limits from proposed experiments such as SHiP and FCC-ee are not shown. Besides, for m_N much below the EW scale, i.e. $m_N < 1$ GeV, the limits are also shown in the figure. As these limits are not relevant for the studies of this thesis, we do not discuss them in detail, only briefly indicate where the limits are from. For $m_N \sim 1$ MeV, the upper limits are set by PSI [259], PIENU [260], KEK [261, 262], measurements of the muon decay spectrum [263], Super-Kamiokande [264], E949 [265], NA62 [266], T2K [267] and MicroBooNE [268]. For $m_N \sim 100$ eV, limits have been placed by oscillation experiments such as IceCube [269, 270], MINOS/MINOS+ [271], Super-Kamiokande [272], NOνA [273], CDHS [274] and CCFR [275]. It should be noted that limits on the disappearance channel, i.e. active to sterile oscillation, tend towards a constant upper bound as a function of the difference of mass square Δm^2 and hence m_N. This bound can in principle be extended to arbitrarily large m_N, covering the region between 100 eV and 1 MeV. Finally, limits have been set from considerations of supernovae [276] and the non-observation of galactic X-rays [277, 278].

As can be seen, even the most stringent limits can not reach the generic seesaw limit $m_\nu \approx V_{lN}^2 m_N$ with $m_\nu < 0.3$ eV as discussed in Sec. 2.4. The above limits only take into account the production via the mixing to active neutrinos. In the $B-L$ model, the heavy neutrinos can also be produced via the SM-like Higgs h_1 or Z'. The cross section of these processes is independent of the mixing and a better sensitivity on the mixing is expected.

Chapter 6

Constraints from LHC SM Measurements

At the LHC, both precision measurements and direct final states searches are carried out. ATLAS and CMS make precise measurements of SM process cross sections with specific kinematical selection criteria. The main purpose for this is to compare with the SM theory predictions but they can be used to constrain any BSM physics that contributes to the same final state, i.e. one looks at deviations of the SM cross sections and distributions. For example, the LHC measurements of the dilepton cross section and distribution, mainly from $pp \to Z \to l^+l^-$ processes in the SM, can be sensitive to the $B-L$ model since it contributes as $pp \to Z' \to l^+l^-$. On the other hand, searches, looking at dedicated signals with a specific selection criteria to reduce the SM background, can obtain a better sensitivity in a specific scenario. Both measurements and searches can constrain BSM theories including the $B-L$ model discussed here. Direct BSM final states searches have been considered for most cases. However, undertaking this method for all possible signatures and scenarios is formidable. Thus, an alternative way can be provided by applying the large data of the existing measurements of SM signatures. This is done by using particle-level differential measurements in fiducial volumes of phase-space which are mostly model-independent. This method can possibly achieve sensitivities for scenarios where non-minimal models are considered, e.g. multiple BSM contributions.

In this chapter, we apply this method to the aforementioned $B-L$ model for several benchmark scenarios. Comparable sensitivities on the model parameters to the direct searches are then obtained. Nevertheless, the method is here primarily used to set limits on the combined gauge and scalar sector of the model, on the other hand, heavy neutrino searches using displaced vertices cannot be used as this does not correspond to a SM signature.

6.1 Constraints On New Theories Using Rivet

The `CONTUR` framework was first introduced in Ref. [1]. It works as follows, the Lagrangian of a specific BSM model is implemented in `FeynRules` [2] and is used to produce a `UFO` [3] which is fed to `Herwig7` [147]. For our $B-L$ model, we implement the `UFO` as introduced in the beginning of Chapter 3. `Herwig7` then generates all tree-level processes containing one or more BSM particles as well as next-to-leading order gluon fusion and photons loops for the Higgs production in proton-proton collisions at 7, 8 and 13 TeV. Here it is assumed that interference terms between the BSM and the SM contributions are negligible. While interference effects can be sizeable, they largely affect the detailed spectral shape. The effect is negligible for our purposes and the reader is referred to Ref. [279] for details. Unstable particle decays are handled by `Herwig7`, while a leading-logarithmic shower is used to take care of QED and QCD radiation. To produce a realistic final state for every event, hadronisation and hadron decays are also simulated using `Herwig7`. The `Herwig7` events are passed to `Rivet` [280] which calculates their contribution in the fiducial volumes of the LHC measurements from ATLAS, CMS and LHCb.

The significance of the additional BSM contribution to the experimental uncertainties on the measurements is derived using a simple χ^2 test statistic. For a certain C.L., we can obtain limits on the BSM parameters assuming the measurement is purely the SM. The difference between the BSM prediction and the SM measurement gives the exclusion. Asymptotic distributions of the test statistic [281] are adopted for the calculation of the confidence interval for different signal hypotheses. The confidence interval is interpreted as a C.L. using the C.L.s formalism [282]. Statistical correlations are eliminated by only using the most significant point from any data set where there are overlaps of events. Systematic uncertainties are assumed such that they are taken to be 100% correlated within a distribution and uncorrelated between distributions.

Within the `CONTUR` framework, in principle all processes in Sec. 4.2 can be studied, except those processes containing long-lived heavy neutrinos. Long-lived or stable exotic particles still cannot be considered in the `CONTUR` framework since the SM fiducial cross section and the detector corrections only consider prompt particles and weak decays of SM particles including B-hadrons and τ leptons in specialized cases. In practise, the heavy neutrinos are considered to be effectively stable and will appear as missing transverse energy showing as missing energy contributions to the fiducial cross sections.

6.2 Benchmark scenarios

To access the constraints imposed in the `CONTUR` framework, we consider the benchmark scenarios summarised in Tab. 6.1. In each case, we scan over two-dimensional slices of the parameter space while keeping all other parameters fixed. We set the neutrino masses to be $m_{N_i} = m_{Z'}/5$ to make the heavy neutrino Yukawa couplings always smaller than g_{B-L} so the perturbative condition is automatically met by requiring $g_{B-L} < 1$ and the phase space of Z' decays to a pair of N_i is appreciable. [1] The light neutrino masses are fixed to be 0.1 eV as it is not involved in the BSM signatures, so the active-sterile mixing strengths are fixed to $V_{lN_i} = \sqrt{0.1\ \text{eV}/m_{N_i}}$. When we scan over the gauge sector, we fix $m_{h_2} = m_{Z'}/(2g_{B-L})$ in Case A and B so $\lambda_2 \lesssim 1/2$ which is still perturbative for $m_{h_2} \gg m_{h_1}$ so that perturbativity is likely secured. Meanwhile, we keep $m_{h_2} = 200$ GeV in Case C for comparison. The Higgs mixing $\sin\alpha$ is either chosen to be zero (Case A) or close to maximum 0.2 which can be obtained from Fig. 5.3 (Case B, C).

For Case D and E, the $U(1)_{B-L}$ breaking VEV $\tilde{x} \equiv \frac{m_{Z'}}{2g_{B-L}}$ should be larger than

---

[1] Any possible values which can maintain the two requirement are also reasonable, as we select $m_N = 0.3 * m_{Z'}$ in Chapter 8.

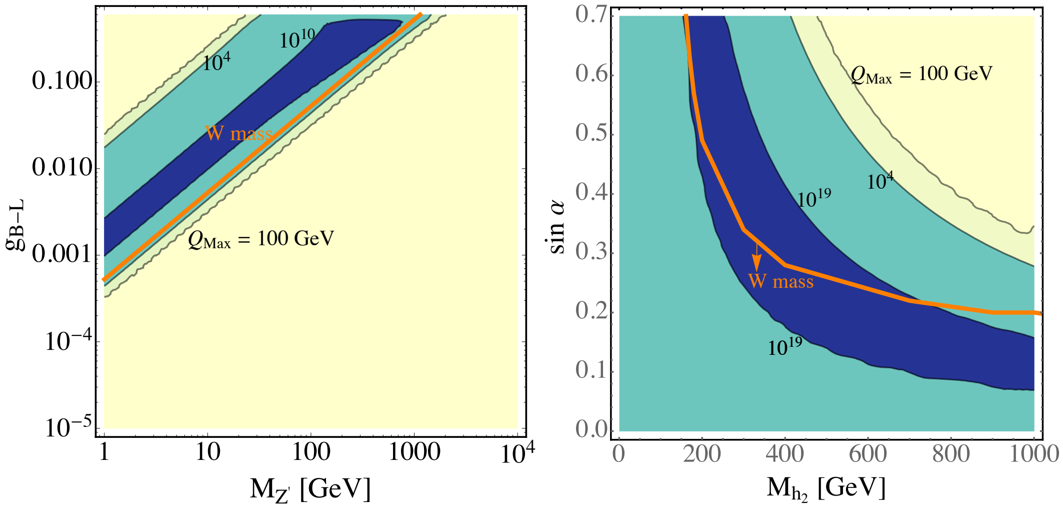

Figure 6.1: Maximal perturbative scale $Q_{\rm Max}$ in GeV and constraint from EW W mass corrections (see Sec. 3.3) as a function of: g_{B-L} and $m_{Z'}$ with $m_{h_2} = m_{Z'}/(2g_{B-L})$ and $\sin\alpha = 0.2$ (Case B) (left) and: m_{h_2} and $\sin\alpha$ with $m_{Z'} = 7$ TeV and $g_{B-L} = 0.2$ (Case D) (right). The W mass constraint is satisfied above (below) the depicted contour in the left (right) panel, as indicated by the arrows.

3.5 TeV, cf. Sec. 5.1 Eqn. (5.1), and we choose $g_{B-L} = 0.2$, $m_{Z'} = 7$ TeV (Case D), or $g_{B-L} = 10^{-3}$, $m_{Z'} = 35$ GeV (Case E).

Scenario	$m_{Z'}$ [GeV]	g_{B-L}	m_{h_2}	$\sin\alpha$	m_{N_i}
A	$[1, 10^4]$	$[3\times10^{-5}, 0.6]$	$m_{Z'}/(2g_{B-L})$	0	$m_{Z'}/5$
B	$[1, 10^4]$	$[3\times10^{-5}, 0.6]$	$m_{Z'}/(2g_{B-L})$	0.2	$m_{Z'}/5$
C	$[1, 10^4]$	$[3\times10^{-5}, 0.6]$	200 GeV	0.2	$m_{Z'}/5$
D	7000	0.2	[0, 800] GeV	[0, 0.7]	$m_{Z'}/5$
E	35	10^{-3}	[0, 800] GeV	[0, 0.7]	$m_{Z'}/5$

Table 6.1: Benchmark scenarios used in our analysis. Additionally, the active-sterile neutrino mixing is fixed as $V_{lN} = \sqrt{0.1\ \text{eV}/m_N}$.

Before we make a detailed analysis based on the LHC measurements, we first take into account the theoretical considerations mentioned in Sec. 3.3. We will choose the parameters in Tab. 6.1 at the EW scale, then evolve them according to the renormalization group equations. We then calculate the maximal scale $Q > Q_{\rm EW}$ for the model to sustain the vacuum stability and pertubativity conditions. We will also indicate these conditions as well as the W boson mass correction for these scenarios.

In Fig. 6.1, we show the maximal scale $Q_{\rm Max}$ for the model to sustain the theoretical constraints including the W boson mass constraint discussed in Sec. 3.3 for Case B and D. In Fig. 6.1 (left), we show the maximal scale for Case B where only a narrow band $g_{B-L} \approx 10^{-3}$, $m_{h_2} \approx 1$ GeV to $g_{B-L} \lesssim 1$, $m_{Z'} \approx 1$ TeV can have Q_{Max} as high as 10^{10} GeV. This is an indirect effect mainly coming from the fact that $m_{h_2} = \frac{m_{Z'}}{2g_{B-L}}$ changes for different $m_{Z'}$ and g_{B-L} while the $\sin\alpha$ is fixed at 0.2 which is quite high. This dependence is clearer in the right plot where vacuum stability and perturbativity rules out simultaneously large regions while a hyperbolic band in the middle can have a Q_{Max} at or above the Planck scale. Besides, the W boson constraint taken from the Ref. [46] is also shown in both plots. For Case B, this is also an indirect bound as different combinations of $m_{Z'}$ and g_{B-L} make m_{h_2} and $\sin\alpha$ correct the W boson mass differently. The allowed region in the left plot is shown as the region *above* the depicted line. For the right plot, the allowed parameter space from the limit for W boson mass corrections is shown *below* the corresponding line.

6.3 Constraints on the gauge sector

We first show the `CONTUR` constraints in Case A, B and C, respectively, for the gauge sector parameters in the top, middle and bottom panels of Fig. 6.2. In each panel, the left plot shows the excluded regions at 95% and 68% C.L. and the right plot gives a detailed heatmap.

For Case A, the exotic Higgs sector is decoupled as we set $\sin\alpha = 0$, with m_{h_2} taken to equal to the VEV $\tilde{x}$. From the top panel of Fig. 6.2, the `CONTUR` approach rules out most of the region for $g_{B-L} > 0.01$ with $m_{Z'} < 2$ TeV and has very little sensitivity for any region beneath this.

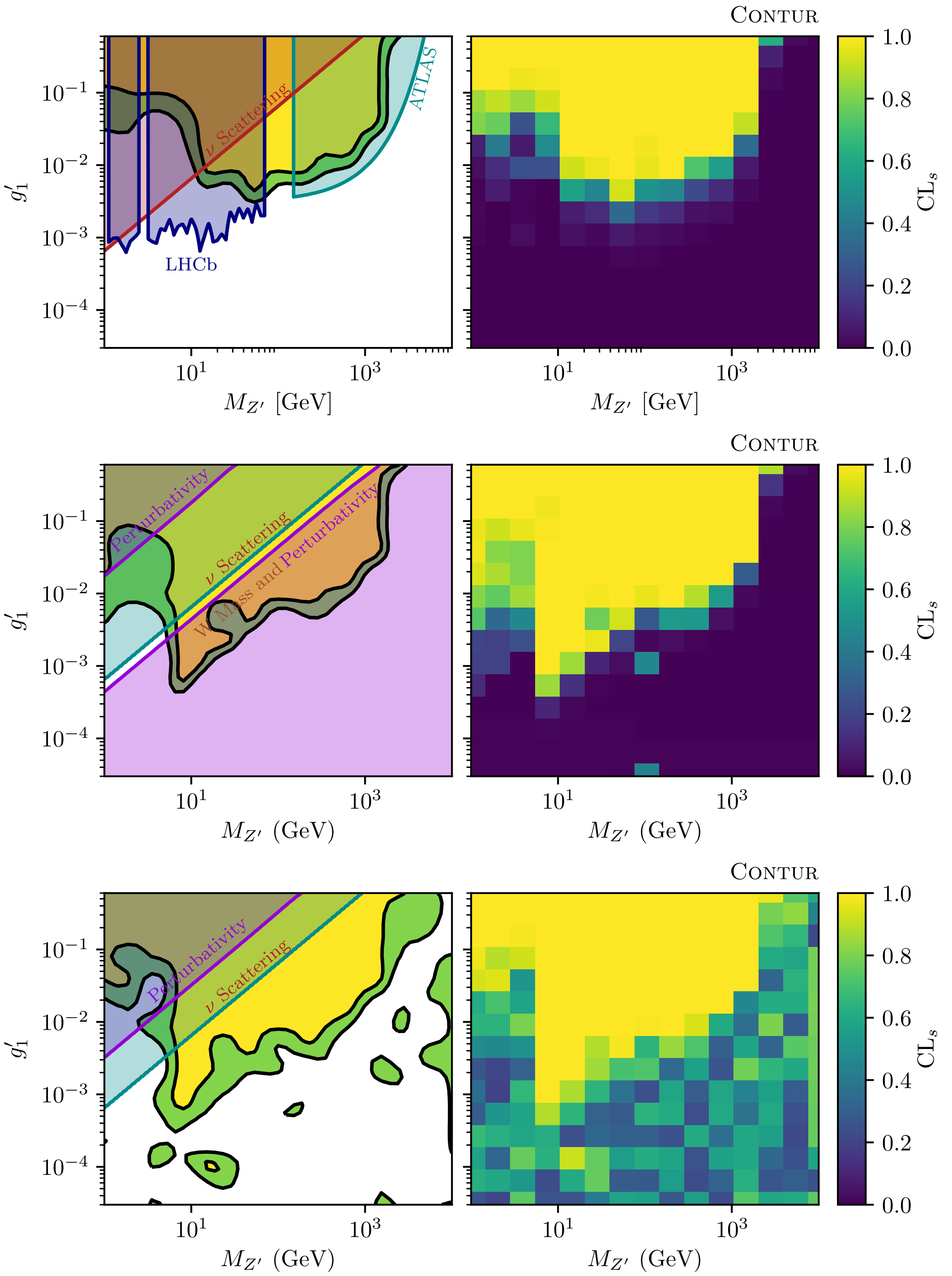

Figure 6.2: Sensitivity of LHC measurements to the $B-L$ model in the $(m_{Z'}, g_{B-L})$ plane. In this figure, g_{B-L} is indicated by g_1'. Top: Case A, $\sin\alpha = 0$, $m_{h_2} = \frac{m_{Z'}}{2g_{B-L}}$; Left, 95% (yellow) and 68% (green) C.L. excluded regions. Right, the corresponding heatmap of exclusion. In addition, the 95% C.L. limits from the `Darkcast` reinterpretation of the LHCb dark photon search, from electron-neutrino scattering, from the ATLAS search using lepton pairs, and the 10 TeV line for the scale which the vacuum stability and perturbativity is still achieved are also shown. Middle: the same but for Case B, $\sin\alpha = 0.2$ and $m_{h_2} = \frac{m_{Z'}}{2g_{B-L}}$; limits from the W mass and electron-neutrino scattering are also shown. Bottom: the same but for Case C, $\sin\alpha = 0.2$, $m_{h_2} = 200$ GeV.

The exclusion is mainly derived via the various leptonic decays of the Z', i.e., $pp \to Z' \to l^+l^- (l = e, \mu)$, which will contribute to the leptonic differential cross sections mainly from the SM processes $pp \to Z \to l^+l^-$. Therefore, the ATLAS 7 and 8 TeV Drell-Yan measurements [283–285] have a big impact for the region 12 GeV $< m_{Z'} <$ 1500 GeV. And the WWW cross section $pp \to W^\pm W^\pm W^\pm \to l^\pm \nu l^\pm \nu l^\pm \nu, l^\pm \nu l^\pm \nu jj$ [286] is also able to be sensitive to larger $m_{Z'}$ from the contribution of $pp \to Z'W^+W^-$. Besides, the Z+jet measurements $pp \to Z/\gamma^* j, Z \to l^+l^-$ [287] can disfavour some region as well from the BSM contribution $pp \to Z'j, Z' \to l^+l^-$. The contribution of the individual measurements will be discussed in detailed later.

Comparing the `CONTUR` limits with those from dedicated searches, the 13 TeV search of the ATLAS [56] yields similar constraints as can be seen in Fig. 6.2 (top left). This is expected given the higher beam energy as we are only using the 7 and 8 TeV measurements as the particle-level measurement for this final state at 13 TeV is not available in `Rivet` at the time we ran `CONTUR`. In general, the sensitive regions we obtain are mostly ruled out by the combination of existing limits, including the ones from LHC searches as well as electron-neutrino scattering cross section measurements. Nevertheless, there are regions near the Z pole with 70 GeV $< m_{Z'} <$ 150 GeV where `CONTUR` provides better constraints than the current limits (except for a very narrow exclusion around the Z mass reaching $g_{B-L} \lesssim 10^{-3}$ from LEP which is not illustrated here).

We move to the middle panel of Fig. 6.2 to discuss Case B. For this scenario, the h_2 mixes to the SM Higgs with $\sin\alpha$ = 0.2. The limit from electron-neutrino scattering is applicable here while the ATLAS dilepton limit will change as the Higgs mixing can alter the production of the Z' by a factor $\cos^2\alpha$. However, the `CONTUR` limit from the 8 TeV dilepton measurement is not significantly modified for high $m_{Z'}$ and g_{B-L}, the ATLAS limit from the top panel should apply similarly.

The main difference is that, in Case B, the theoretical considerations to make the model well-defined at least to $Q_{\text{Max}} = 10$ TeV which is approximately the LHC scale come into play. The constraints from maximal scale from RGE running is shown for Case B at the left panel of Fig. 6.1. The W mass constraint also applies in this scenario because $m_{h_2} = \frac{m_{Z'}}{2g_{B-L}}$ and our choice of $\sin\alpha = 0.2$ can be ruled out for certain values of m_{h_2}. Therefore, only a narrow region is still viable after the combination of the theoretical consideration with electron-neutrino scattering cross section limits. This entire region is almost ruled out by the `CONTUR` analysis.

Case C with $m_{h_2} = 200$ GeV is shown in the bottom panel of Fig. 6.2. The extra Higgs mass is chosen such that we have an appreciable viable region given the theoretical considerations. In this case, the theoretically disfavoured region is already ruled out by electron-neutrino scattering measurements. Compared to Case B, `CONTUR` gives similar exclusion regions. Additionally, the heatmap on the right side indicates that there is sensitivity to constrain whole $m_{Z'} - g_{B-L}$ plane. This arises because the exotic Higgs production cross section (dominantly via gluon fusion) with subsequent decays to WW (e.g., $pp(gg) \to h_2 \to WW \to l\nu jj$), is not sensitive to $m_{Z'}$ and g_{B-L}, but the events will contribute to the $l\nu jj$ signal rate measurement of [286]. Besides, we will obtain exclusions at various cases from the measurements of the leptonic decays of W and/or Z. For small $m_{Z'}$ and appreciable g_{B-L} such that it is larger than 10^{-3}, h_2 can decay dominantly to Z' pairs and decay subsequently to leptonic final states, e.g., $pp(gg) \to h_2 \to Z'Z' \to l^+l^-l^+l^-$, with branching ratio about 40%. Therefore, the ATLAS 7 (8) TeV four-lepton $pp \to ZZ^{(*)} \to l^+l^-l'^+l'^-$ measurement [288–291] can be extremely sensitive at this region even though the Z' mass is below the Z or even Z^* mass threshold. With these points, it is expected that with future LHC measurements with higher luminosity and beam energy, this method will be even more sensitive in these regions.

Comparing the Case C to the existing limits, assuming the ATLAS dilepton constraint still applies, `CONTUR` gives better constraints. This is due to the fact that Case C is a non-minimal scenario as both the BSM contribution from the Z' as well as h_2 can have exclusion power on the parameter space.

For all cases, the heavy neutrino production processes, $pp \to Z' \to N_iN_i$ only contribute to the missing transverse energy in SM measurements. This is justified as the heavy neutrinos are assumed to be effectively stable and thus do not decay in the fiducial volume. A good example is shown in the left panel of Fig. 6.3 for Case B. Here, we can see that it is a good approximation for the heavy neutrinos to be effectively stable, $m_{N_i} \lesssim 20$ GeV, thus $m_{Z'} \lesssim 100$ GeV. While it would decay more promptly for higher masses, the production cross section is negligible, as justified in the right panel of Fig. 6.3. Only for higher g_{B-L}, the cross section becomes significant. Therefore, the overall contribution from heavy neutrino production to the `CONTUR` sensitivity for the parameter space we are considering is negligible.

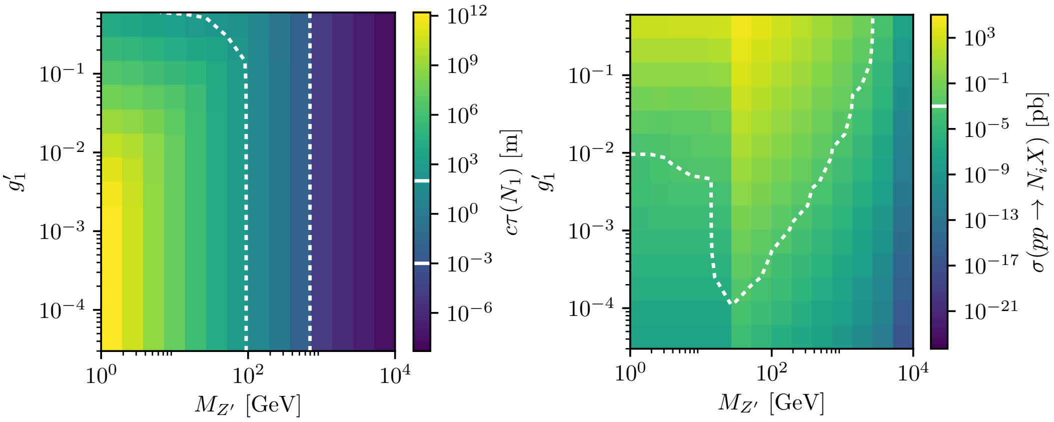

Figure 6.3: Left: The proper decay length of the heavy neutrinos as a function of g_{B-L} (indicated by g'_1) and $m_{Z'}$ for Case B. Here we set $m_{N_i} = m_{Z'}/5$. The dashed white lines illustrates the boundaries of the regions such that the heavy neutrinos are considered to be 'long-lived particles' with proper decay lengths between 1 mm-100 m. Right: the total production cross section of the heavy neutrinos in Case B, for 8 TeV proton-proton collisions. The 1 fb cross section contour is shown as the white dashed line which corresponds to approximately 30 events before any cuts, for the maximum luminosity we are consider here.

To illustrate how the overall sensitivity is obtained via individual measurements, Fig. 6.4 gives an example for Case C showing the constraints from different, statistically independent sources of data. For instance, in Fig. 6.4 b, the sensitivity of four-lepton measurements [288–291] to low mass Z' and $g_{B-L} > 10^{-3}$ is demonstrated. The main difference to Case B is due to the smaller m_{h_2} and thus higher production cross section for h_2, the Z' production from both the SM Higgs h_1 and BSM h_2 is larger for low mass Z', and their contribution to several leptonic signatures measurements becomes more important (e.g., panels a and e). It should be acknowledged that though measurements of Higgs properties such as its signal rates and decay width can also be sensitive in this scenario, but this is not included in the

`CONTUR` framework yet.

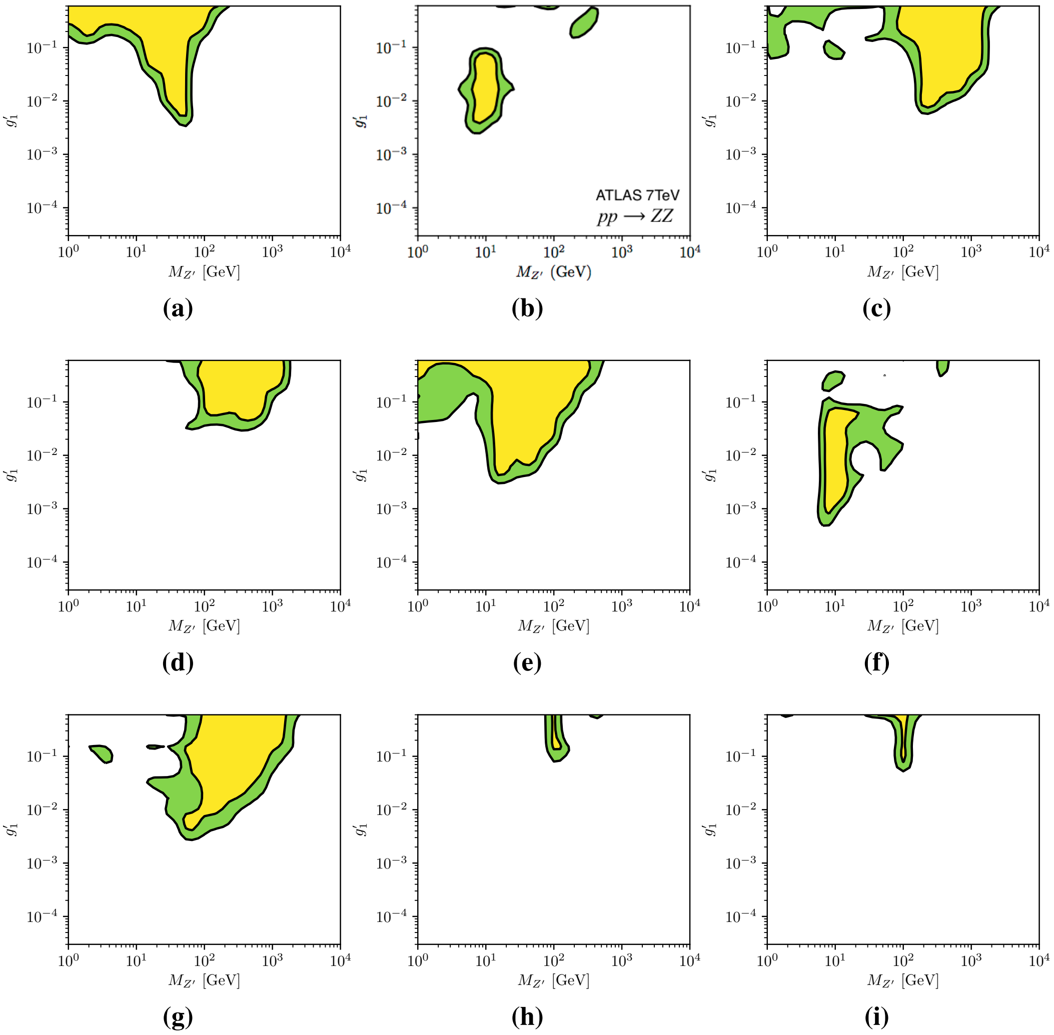

(a) **(b)** **(c)**

(d) **(e)** **(f)**

(g) **(h)** **(i)**

Figure 6.4: Constraints on the $m_{Z'} - g_{B-L}$ parameter space for Case C from the individual measurements of (a) Low mass Drell-Yan $pp \to Z/\gamma^* \to ll, (l = e, \mu)$ at ATLAS (7 TeV) [283], (b) Four-lepton $pp \to ZZ^{(*)} \to l^+l^-l'^+l'^-$ at ATLAS (7 TeV) [288], (c) High mass Drell-Yan at ATLAS (8 TeV) [285], (d) Dilepton plus photon $pp \to Z\gamma, Z\gamma\gamma$, with $Z \to l^+l^-, \nu\bar{\nu}$ at ATLAS (8 TeV) [292], (e) Dilepton plus jet $pp \to Zjj$, with $Z \to l^+l^-$ [284, 293, 294] at ATLAS (8 TeV), (f) Four-lepton at ATLAS (8 TeV) [290, 291], (g) Dilepton plus missing transverse energy $pp \to W^\pm W^\pm W^\pm \to l^\pm \nu l^\pm \nu l^\pm \nu, l^\pm \nu l^\pm \nu jj$ and $pp \to W^\pm W^\pm \to l^\pm \nu l^\pm \nu$ at ATLAS (8 TeV) [286,295], (h) Dilepton plus jet at CMS (8 TeV) [296], (i) Dimuon plus jet at LHCb (7 TeV) [297]. In this figure, g_{B-L} is indicated by g_1'. The colour scheme is the same as Fig. 6.2.

Examples of how the SM measurements are applied our BSM signal in `CONTUR` are shown in Fig. 6.5 and 6.6 for Case C moving along the edge of the region of Case C excluded by electron-neutrino scattering. The cross sections and

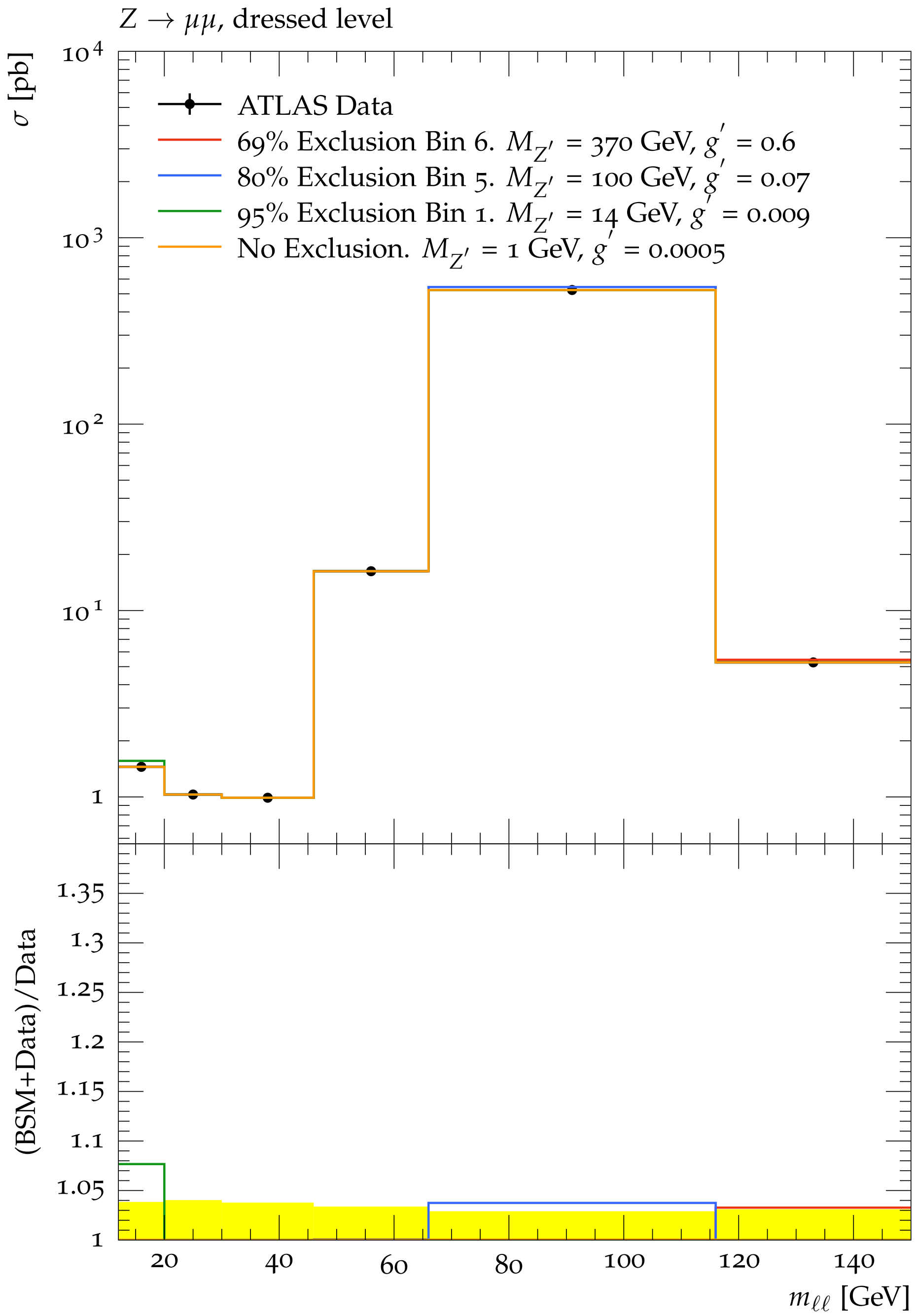

Figure 6.5: Examples of the exclusion of four points in the parameter space, Fig. 6.2 bottom panel (Case C). From Dilepton plus jet $pp \to Zjj$, with $Z \to l^+l^-$ measurement [284] (corresponding to part of Fig. 6.4 e). The legend indicates the parameter point in $m_{Z'}$ and g_{B-L} space with $m_{h_2} = 200$ GeV and $\sin\alpha = 0.2$. In this figure, g_{B-L} is indicated by g'.

branching ratios obtained from `Herwig` for the dominant processes in Fig. 6.5 and 6.6 is illustrated in Tab. 6.2. The branching ratio of $Z' \to jj$ can be found in Fig. 4.4. From the table, the $m_{Z'} = 1$ GeV case lead to dominant final states of $4l$

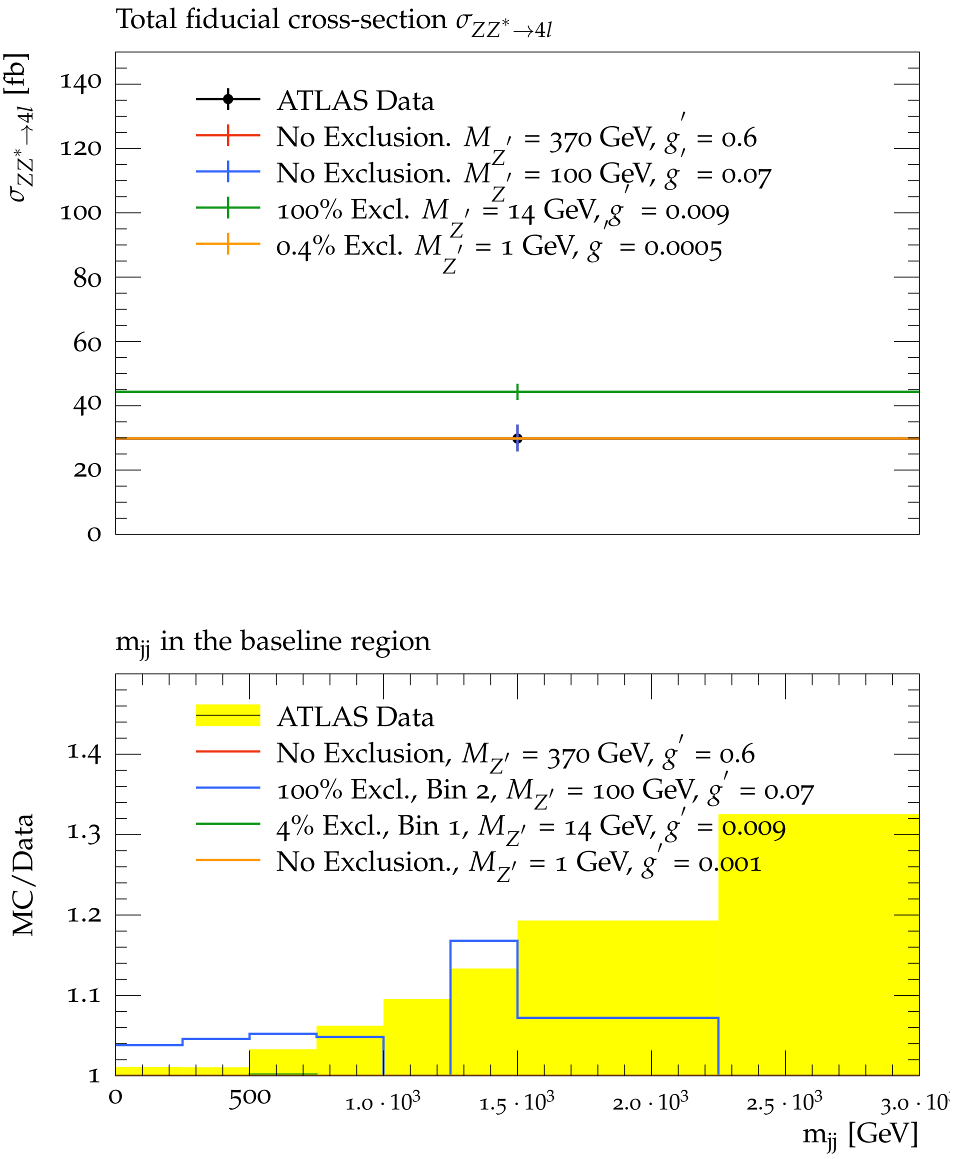

Figure 6.6: Same as Fig. 6.5 but from four-lepton measurement (top) [288] (corresponding to Fig. 6.4 b), and dijet mass in Z events $pp \to Z \to jj$ (bottom) [293] (corresponding to part of Fig. 6.4 e). The legend indicates the parameter point in $m_{Z'}$ and g_{B-L} space with $m_{h_2} = 200$ GeV and $\sin\alpha = 0.2$. In this figure, g_{B-L} is indicated by g'.

with small cross section, while $2l$ for the other cases. In Fig. 6.5, the m_{ll} distribution for both the ATLAS data and the BSM prediction is compared. Combined with the information provided in Tab. 6.2, the green line ($m_{Z'} = 14$ GeV and $g_{B-L} = 0.009$) shows a scenario excluded at 95% C.L. where the dominant BSM contribution is the production process for Z' associated with a jet, e.g., $pp(u\bar{u}) \to gZ' \to l^+l^-j$. In Fig. 6.6 (top), BSM and ATLAS data for the total fiducial cross section $\sigma_{pp\to ZZ^*\to 4l}$

is illustrated. Here the strongest exclusion comes again from the case with $m_{Z'}$ = 14 GeV and g_{B-L} = 0.009. In Fig. 6.6 (bottom), the m_{jj} distribution gives a powerful exclusion when $m_{Z'}$ = 100 GeV close to the Z mass, as the decay of the Z' gives additional contribution for $m_{jj} \lesssim 500$ GeV.

$m_{Z'}$ [GeV]	g_{B-L}	Production Process	Cross Section [pb]	Decay	Branching Ratio
1	0.0005	$gg \to h_{1,2} \to Z'Z'$ $gg \to gh_2$	0.6 0.078	$Z' \to l^+l^-(jj)$ $h_2 \to Z'Z'$	0.36(0.37) 0.58
14	0.009	$u\bar{u} \to gZ'$	40.6	$Z' \to l^+l^-(jj)$	0.27(0.46)
100	0.07	$u\bar{u} \to Z' \to l^+l^-$	31	$Z' \to l^+l^-(jj)$	0.27(0.46)
370	0.6	$u\bar{u} \to Z' \to l^+l^-$	30	$Z' \to l^+l^-(jj)$	0.27(0.46)

Table 6.2: Cross sections (8 TeV pp collisions) and branching ratio for the dominant processes in Fig. 6.5 and 6.6 for Case C.

6.4 Constraints on the scalar sector

We now consider Cases D and E with variations in the scalar sector. The corresponding `CONTUR` limits are shown in Fig. 6.7.

For Case D, we have a heavy Z' with negligible contribution, but the h_2 can potentially mix with the SM Higgs significantly. The theoretical considerations from W boson mass disfavour the upper right corner. $pp(gg) \to h_2 \to WW, ZZ$ processes with threshold at approximately 200 GeV as well as $pp(gg) \to h_2 \to t\bar{t}$ processes with threshold at approximately 400 GeV and their subsequent decays to leptons or jets, yield some sensitivity on mixing angles such that $\sin\alpha \lesssim 0.2$. The most sensitive limits are the $lljj$ cross section [286] as well as the four-lepton cross section [289]. In Fig. 6.8 and 6.9, the exclusion for four points obtained from the aforementioned measurements is shown as an example and the corresponding dominant processes are listed in Tab. 6.3. The points are taken by moving along the lower edge of the theoretical allowed region for the Case D. The decay of $h_2 \to WW$ can not lead to final states of either $lljj$ or $4l$, while it is still listed for the sake of completeness. The LHC data do provide a minor sensitivity for small $\sin\alpha$ as indicated by the heat map of Fig. 6.7. With more data acquired in the future high luminosity runs, more sensitive limits on $\sin\alpha$ and m_{h_2} might be achievable.

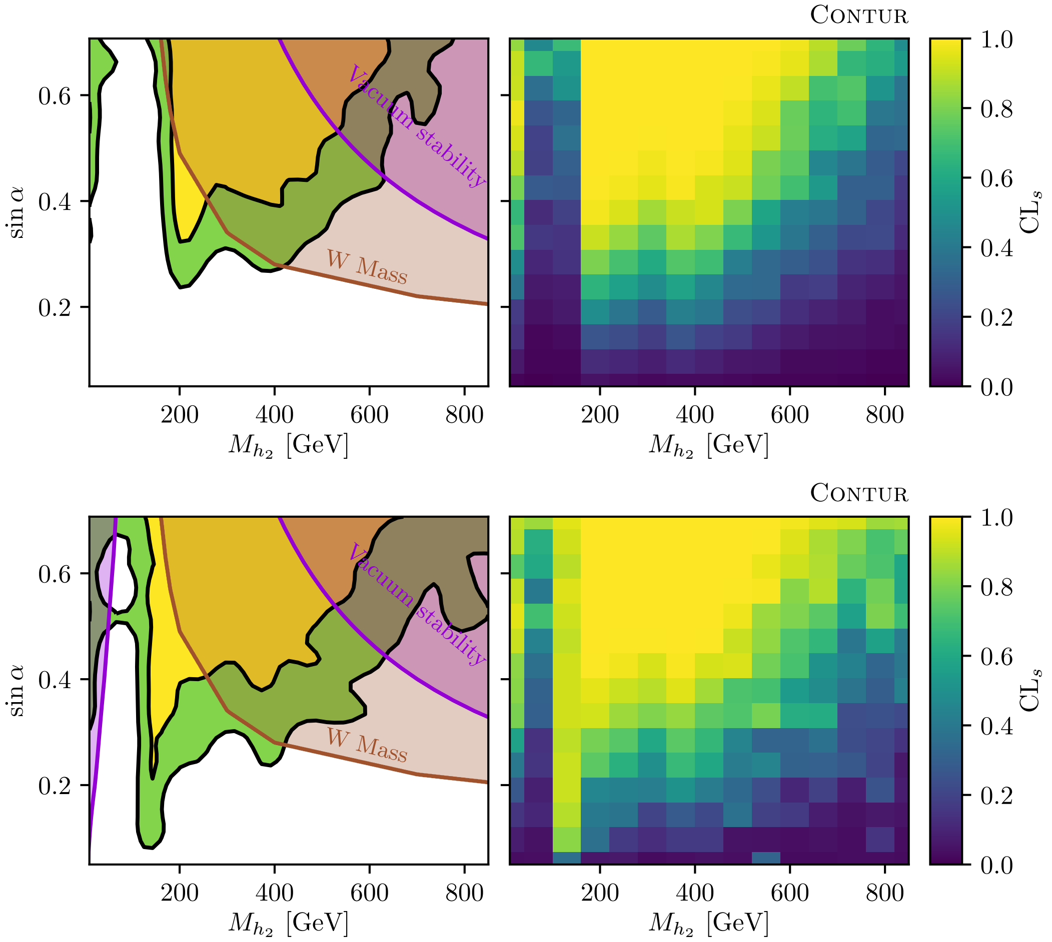

Figure 6.7: Sensitivity of LHC measurements to the $B-L$ model in the $(m_{h_2}, \sin\alpha)$ plane. Top: Case D, g_{B-L} = 0.2, $m_{Z'}$ = 7 TeV; Left, 95% (yellow) and 68% (green) C.L. excluded regions. Right, the corresponding heatmap of exclusion. In addition, the theoretical constraints including the limits from perturbativity and vacuum stability, demanding the model is well-defined at a scale at least 10 TeV together with the W boson mass constraint are illustrated as well. Bottom: the same but for Case E, g_{B-L} = 0.001, $m_{Z'}$ = 35 GeV; same as in top but for Case E.

Case E as shown at the bottom of Fig. 6.7 can be regarded as complementary to Case D. Here, the Z' is light and can be produced in h_2 decays (e.g., $pp(gg) \to h_2 \to Z'Z'$) but the tiny value of g_{B-L} makes the rate small but still appreciable at low m_{h_2}. In general, the limits from LHC measurements are similar to Case D. As Z' can be pair produced from h_2 decays, there are additional limits for lower m_{h_2}.

In Summary, we have shown the constraints from LHC measurements using `CONTUR` in this chapter for several benchmark scenarios. For single BSM contribu-

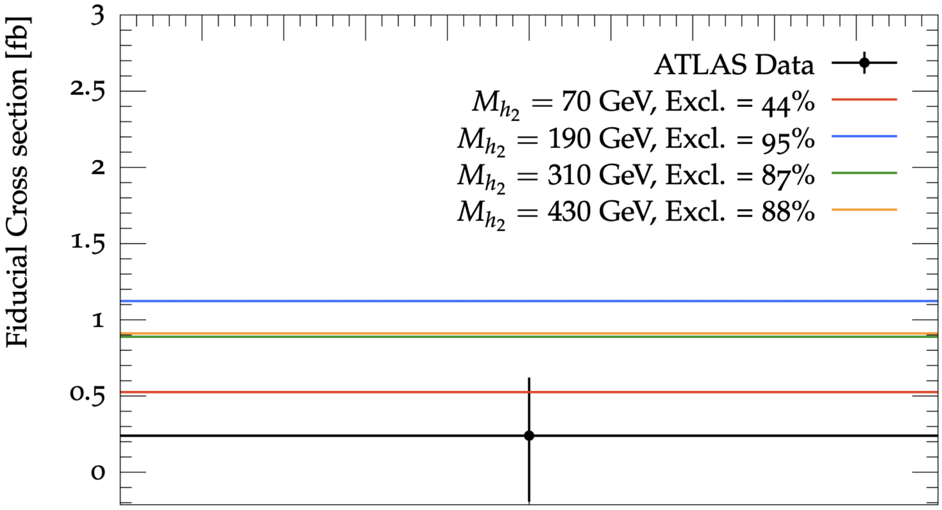

Figure 6.8: Examples of the exclusion for four points along the lower edge of the theoretically allowed region of the left panel of Fig. 6.7 top (Case D) from $lljj$ cross section $pp \to W^\pm W^\pm W^\pm \to l^\pm \nu l^\pm \nu jj$ measurement [286]. The legend indicates the parameter point with $m_{Z'}$ = 7 TeV, g_{B-L} = 0.2, $\sin\alpha$ = 0.42

tion as Case A where there is no Higgs mixing or Case D where the Z' is decoupled, this method still achieves competitive exclusion power to the dedicated searches. When multiple BSM contribution are considered in other cases, while this conditions have been barely considered for most of the existing searches, this method can yield the sum of the exclusion power thus stringent limits are obtained.

m_{h_2} [GeV]	Production Process	Cross Section [pb]	Decay	Branching Ratios
70	$u\bar{u} \to Zh_2$	0.13	$h_2 \to b\bar{b}$	0.88
190	$gg \to gh_2$	0.37	$h_2 \to WW$	0.78
			$h_2 \to ZZ(\to jjll)$	0.21
310	$gg \to gh_2$	0.20	$h_2 \to WW$	0.51
			$h_2 \to ZZ(\to jjll)$	0.27
			$h_2 \to hh(\to jjll)$	0.22
430	$gg \to gh_2$	0.14	$h_2 \to WW$	0.46
			$h_2 \to ZZ(\to jjll)$	0.22
			$h_2 \to hh(\to jjll)$	0.21
			$h_2 \to t\bar{t}$	0.11

Table 6.3: Cross sections (8 TeV pp collisions) and branching ratios for the dominant processes in Fig. 6.8 and 6.9 for Case D.

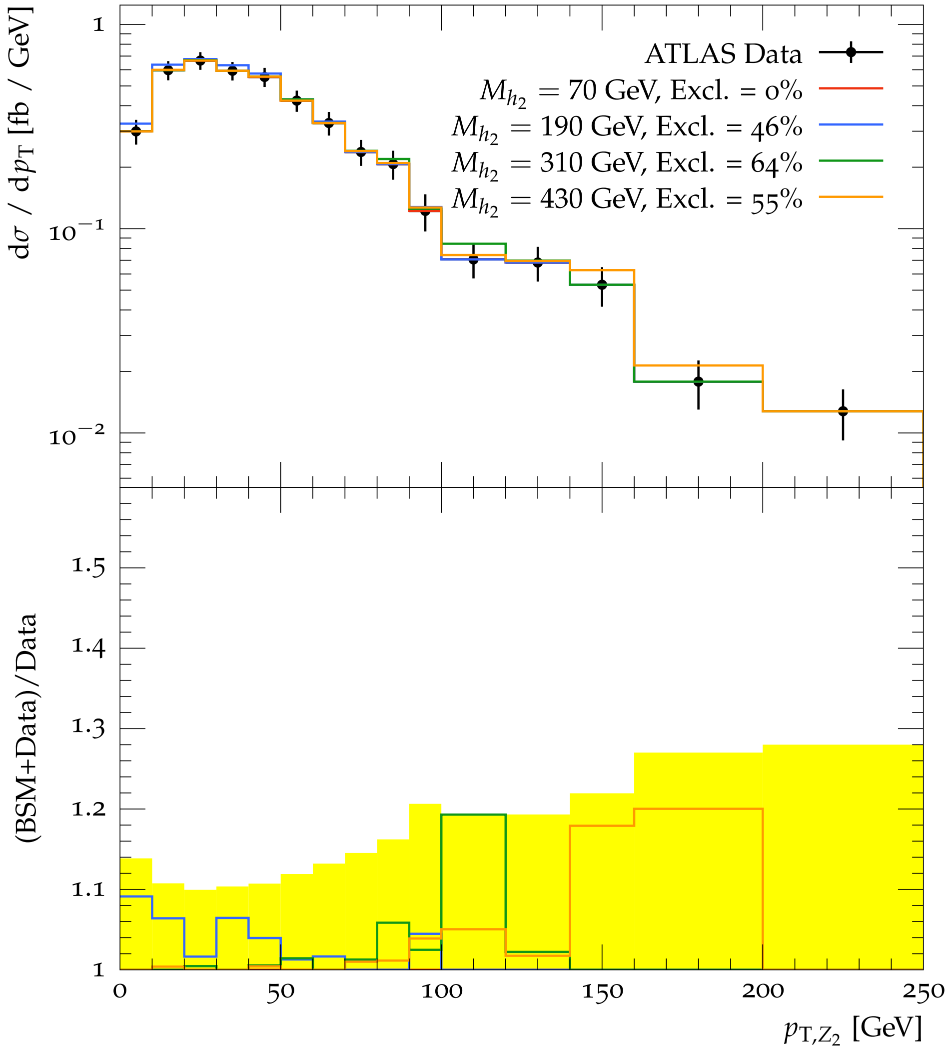

Figure 6.9: Same as Fig. 6.8 but from four-lepton measurement [289]. The legend indicates the parameter point with $m_{Z'} = 7$ TeV, $g_{B-L} = 0.2$, $\sin\alpha = 0.42$. The yellow shaded region is the experimental uncertainties of the ATLAS experiment.

Chapter 7

Constraints from Prompt Lepton Searches

In the previous chapter, we have described the constraints arising from LHC SM cross section measurements. In this chapter, we focus on probing the gauge sector again, but by recasting recent searches for prompt leptonic final states (containing mainly muons) which arise from a relatively light Z' in the $B-L$ model.

We consider three production mechanisms for a light Z' with a mass $m_{Z'} \approx 0.25-100$ GeV to get appreciable cross section, Drell-Yan Z' production ($pp \to Z'$, cf. Fig. 4.3 left), Z' pair production via SM-like Higgs ($pp \to h_1 \to Z'Z'$, cf. Fig. 4.3 center), Z' final state radiation (FSR) from Z production ($pp \to Z \to Z'\mu^+\mu^-$, cf. Fig. 4.3 right). Several recent CMS and ATLAS searches set limits on these channels:

- $pp \to Z' \to \mu^+\mu^-$ at CMS [182],
- $pp \to h_1 \to Z'Z' \to 4\mu$ at CMS [206], $\to 4\ell$ at ATLAS [207],
- $pp \to Z \to \mu^+\mu^- Z' \to 4\mu$ at CMS [205].

Apart from the above processes, it is also possible to search for Z' via associated production with W/Z or a jet. These processes will however yield a smaller production cross section compared to the ones listed above. Therefore, we will not explicitly consider them in this work. Besides, it is accounted for in the s-channel production of Z' in the form of showering and hadronization. As mentioned before, numerous searches for resonance in dijet final states are also available. Their limits are however weak and therefore, we do not consider hadronic searches in this chapter.

7.1 Light Z' production and decay

The production and decay mechanisms of Z' are already briefly introduced at Section 4.2. Here, we discuss and calculate their cross section in leading order using `MadGraph5aMC@NLO` -v2.6.3 [146], for the three production mechanisms of Z' and their decay to muons listed above. We focus on the parameter space where $g_{B-L} \lesssim 10^{-3}$ which is approximately the largest allowed value from experimental constraints (cf. Fig. 5.2 in Sec. 5.1).

The cross section of the $s-$channel Drell-Yan channel $pp \to Z' \to \mu^+\mu^-$ is a function of g_{B-L} and $m_{Z'}$ as illustrated in Fig. 7.1 (top left). Here we only calculate the cross section for $m_{Z'} > 10$ GeV as it is difficult to consider the non-perturbative QCD effects for lighter Z'. For lighter $m_{Z'}$, we use extrapolation to extend the contours to $m_{Z'} > 3$ GeV for comparison.

For $pp \to h_1 \to Z'Z' \to 4\mu$ process, $m_{Z'}$ is restricted to below the kinematical threshold, i.e. $m_{Z'} < m_{h_1}/2 \approx 62$ GeV. The production cross section can be appreciable for large Higgs mixing,

$$\begin{aligned}\sigma(pp \to h_1 \to Z'Z') &= \sigma(pp \to h_1) \times \mathrm{Br}(h_1 \to Z'Z') \\ &= \cos^2\alpha \times \sigma(pp \to h_{\mathrm{SM}}) \frac{\Gamma(h_1 \to Z'Z')}{\cos^2\alpha\,\Gamma(h_{\mathrm{SM}}) + \Gamma(h_1 \to Z'Z')},\end{aligned} \tag{7.1}$$

where $\Gamma_{h_{\mathrm{SM}}} \approx 4$ MeV [132]. In Eqn. (7.1), the tiny partial width of Higgs decaying to a pair of heavy neutrinos $\Gamma(h_1 \to NN)$ is neglected, when calculating the total width [90]. The partial decay width of h_1 decays to $Z'Z'$ in our model can be

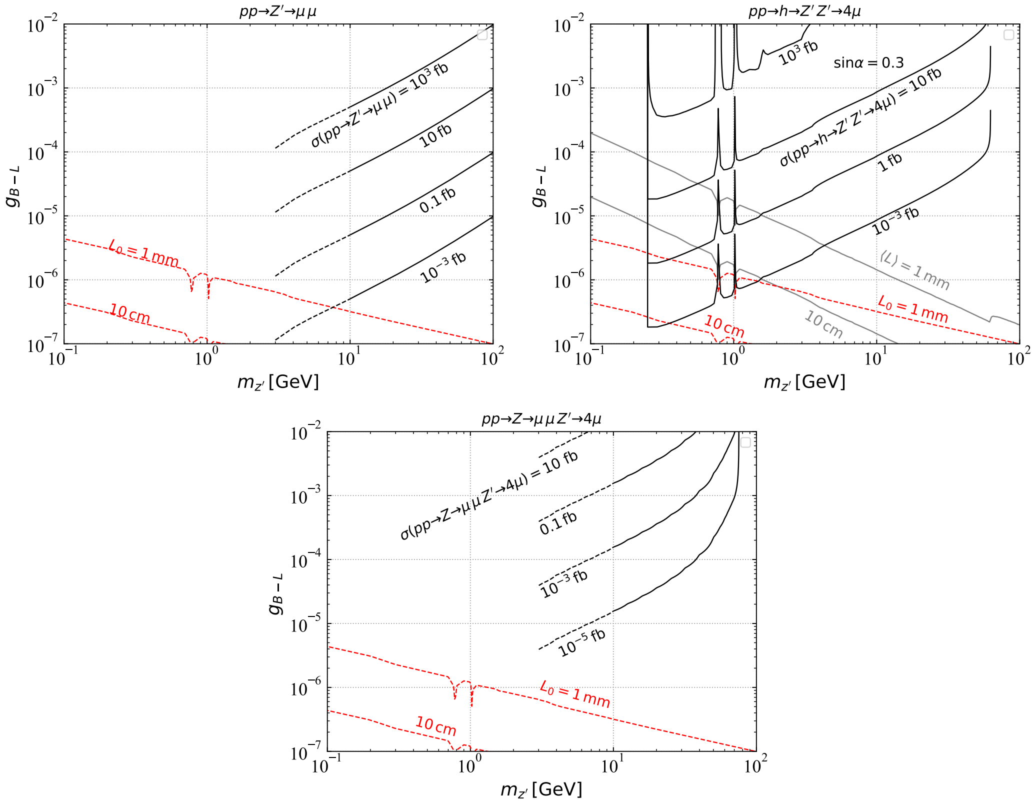

Figure 7.1: Cross section of Drell-Yan Z' production, $pp \to Z' \to \mu^+\mu^-$ (top left), Z' pair-production via Higgs, $pp \to h_1 \to Z'Z' \to 4\mu$ (top right), and Z production with final state radiation (FSR), $pp \to Z \to 2\mu + Z' \to 4\mu$ (bottom), as a function of the Z' mass $m_{Z'}$ and the $U(1)_{B-L}$ gauge coupling g_{B-L} (black solid curves). All cross section are at 13 TeV. In the upper right plot, the Higgs mixing is set to $\sin\alpha = 0.3$. The dashed red lines represent the proper decay length L_0 of Z' while the solid grey lines in the upper right plot indicate the average Z' lab frame displacement $\langle L \rangle$ in SM Higgs production. Figure from Ref. [186].

expressed as

$$\Gamma(h_1 \to Z'Z') = \frac{3\, g_{B-L}^2 \sin^2\alpha}{8\pi m_{Z'}^2} m_{h_1}^3 \sqrt{1 - \left(\frac{2m_{Z'}}{m_{h_1}}\right)^2} \left(1 - 4\left(\frac{m_{Z'}}{m_{h_1}}\right)^2 + 12\left(\frac{m_{Z'}}{m_{h_1}}\right)^4\right). \tag{7.2}$$

In the top right panel of Fig. 7.1, the cross section of Z' pair-production via SM-like Higgs, $pp \to h_1 \to Z'Z' \to 4\mu$ is illustrated as a function of $m_{Z'}$ and g_{B-L} for $2m_\mu < m_{Z'} < \frac{m_{h_1}}{2}$. We choose the Higgs mixing $\sin\alpha = 0.3$ which is approximately the largest allowed value from experimental constraints for a heavy Higgs mass of 300 GeV (cf. Fig. 5.3 in Sec. 5.2). In the figure, there are a few resonances near the QCD threshold $m_{Z'} \approx 1$ GeV, this is due to the fact that the Z' near threshold dominantly decays to mesons (such as $\pi^{\pm,0}$ and Kaon mesons) resonantly [31]. Compared to the Drell-Yan channel, this channel can reach lower $m_{Z'}$ as the Z' is produced from a heavy resonance decays, the SM-like Higgs.

Besides, the aforementioned FSR process $pp \to Z \to \mu^+\mu^- Z' \to 4\mu$ is also possible. This process is particularly useful for $L_\mu - L_\tau$ model [205], as it is not possible to produce the associated Z' from quark annihilation. However, in our model, this channel is less competitive to the above channels. The process is considered for the sake of completeness and the total cross section is shown in Fig. 7.1 (bottom). The total production cross section for this process is tiny due to the suppressed phase space from the requirement of an off-shell muon to emit a massive particle. The cross section is only calculated for $m_{Z'} > 10$ GeV to avoid non-perturbative effects. Similar to Fig. 7.1 (top left), we use extrapolation to extend the contours to $m_{Z'} > 3$ GeV for comparison. From this figure, we can obtain a maximal cross section $\sigma \approx 1$ fb in the parameter space we consider, i.e. $g_{B-L} \lesssim 10^{-3}$.

In addition, as mentioned in Sec. 4.2, for small g_{B-L} and $m_{Z'}$, the lifetime and thus the decay length of Z' can be macroscopic. Moreover, light Z' produced at the LHC can also be highly boosted, increasing the decay length in the lab frame. The boost factor $\beta\gamma = |p_{Z'}|/m_{Z'}$ and an example of its distribution when produced as $pp \to h_1 \to Z'Z'$ is shown in Fig. 7.2. In the figure, the boost factor $\beta\gamma$ can reach $\langle\beta\gamma\rangle \gtrsim 100$ for $m_{Z'} \approx 1$ GeV, but it is reduced for larger $m_{Z'}$.

In Fig. 7.1 (top right), we show the average decay length $\langle L\rangle$ of Z' pair production from SM Higgs decays as an example. As can be seen there, for very low mass Z', the average lab decay length can be more than 10 cm in the parameter space which can be potentially probed by the HL-LHC as it will lead to signature of displaced vertex which is detectable at the CMS/ATLAS detector (see Eqns. 8.6 and 8.7). Light Z' from Drell-Yan can also be boosted, but as we are only considering $m_{Z'} > 10$ GeV in this case, we omit it.

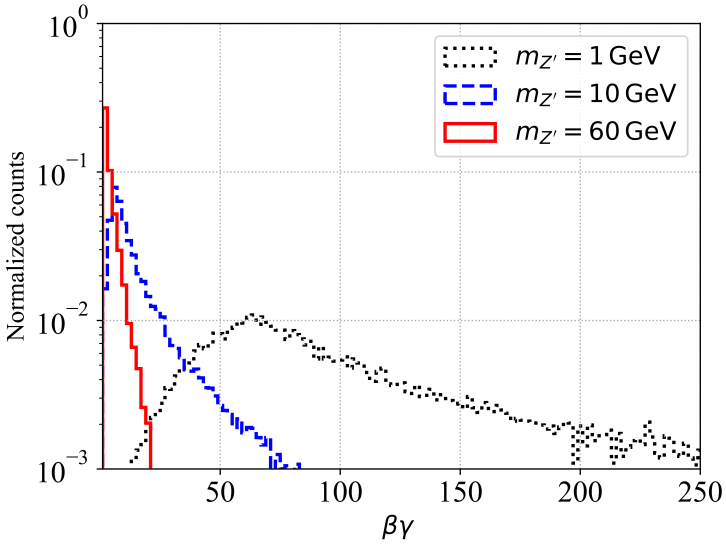

Figure 7.2: Truth level distribution of the Z' boost factor $\beta\gamma$ in Z' pair-production through SM Higgs, $pp \to h_1 \to Z'Z'$.

7.2 Recasting procedure

At this section, we describe the recasting procedure to apply the ATLAS/CMS searches mentioned at the start of this chapter.

In order to do so, we compare the cross section of a given experimental signature, as predicted in the $B-L$ model and take into account any experimental selection criteria. The $B-L$ cross section is calculated using the following procedure. We employ the UFO [3] for the $B-L$ model with next-to-leading order (NLO) QCD production, developed in Ref. [90], as introduced in the beginning of Chapter 3, in combination with the Monte Carlo event generator `MadGraph5aMC@NLO` - v2.6.3 [146] at parton level. For every signal sample, we generate 10^4 signal events. We then pass the generated parton level events to `PYTHIA` v8.235 [298] which handles the initial and final state parton showering, hadronization and heavy hadron decays. We do not simulate detector effects, as the experimental limits are already unfolded. Instead, individual analysis efficiencies as described later are taken into account in order to obtain results. The analysis results we consider here include either fiducial cross sections reported in a certain part of the phase space without detector effects, or experimental efficiencies which can be applied to hadronized events. We therefore do not compromise on the accuracy of our results due to the absence of a detector simulation as the existing experimental limits are unfolded. For the Higgs-mediated mode we use the NLO capabilities of our model to simulate Higgs production via gluon-gluon fusion.

Z' pair production via SM-like Higgs at CMS (CMS $h_1 \to 4\mu$) The CMS collaboration reported on a search for the pair production of new light bosons a decaying into muons at $\sqrt{s} = 13$ TeV with an integrated luminosity of 35.9 fb^{-1} in Ref. [206], $pp \to h_1 \to aa \to 4\mu$. This search looked for both final states from prompt decays and with an intermediate displacements, $\langle L \rangle \approx 10$ cm. With no observation of excess, the search gives an upper limit on the signal cross section in prompt and displaced final states for a neutral boson with mass $m_a \approx 0.25-8.5$ GeV. In order to recast the limits in the $B-L$ model, we take the limits on $\sigma(pp \to h_1 \to 2a)\mathrm{Br}^2(a \to 2\mu)\alpha_{\mathrm{gen}}$ from CMS, where α_{gen} is the generator level acceptance, and take $m_{Z'} = m_a$. We thus obtain the limit on $\sigma(pp \to h_1 \to Z'Z')\mathrm{Br}^2(Z' \to 2\mu)\alpha_{\mathrm{gen}}$ in our model.

To constrain the parameters g_{B-L} and $m_{Z'}$, we need to calculate the acceptance α_{gen} in simulation. We apply the cuts for our signal samples of the process $pp \to h_1 \to Z'Z' \to 4\mu$ [206],

$$\begin{aligned} p_T(\mu_1) &> 17 \text{ GeV}, \quad |\eta| < 0.9, \quad \text{for the leading muon,} \\ p_T(\mu) &> 8 \text{ GeV}, \quad |\eta| < 2.4, \quad \text{for the other three muons.} \end{aligned} \tag{7.3}$$

Additionally, there is a selection criteria on HLthe transverse displacements L_{xy} as well as the longitudinal displacements L_z (both are defined in Sec. 4.1), of each muon from the IP,

$$L_{xy} < 9.8 \text{ cm}, \;\; L_z < 46.5 \text{ cm}. \tag{7.4}$$

With this criteria, Z' with moderate displacement $L_0 \lesssim 10$ cm are included.

We have been able to reproduce the generator acceptance α_{gen} from [206] for light Z' with a mass of 1 GeV in simulation. For our model, the cuts on the displacement have negligible effects in most of the parameter space as the decay length of Z'

is small. However, for light Z' and small g_{B-L}, the average lab decay length can be macroscopic. For instance, for very light Z' with $m_{Z'} = 0.25$ GeV and $g_{B-L} = 10^{-6}$, the proper decay length of the Z' is $\mathscr{O}$(cm). As the Lorentz boost factor for this case is roughly a hundred as shown in Fig. 7.2, the mean lab decay length $\langle L \rangle$ can reach a meter. Thus, the selection on the displacement becomes relevant for our analysis in a small region of the parameter space.

This search also reports an estimated background of $9.90 \pm 1.24\,\text{stat} \pm 1.84\,\text{syst}$ events for 35.9 fb^{-1} [206]. The 95% C.L. bound on the signal event rate can be derived from $\chi^2 = S^2/B > 3.84$ [132], and very similar limits are obtained from this method.

Moreover, we also calculate the expected sensitivity of this analysis for the HL-LHC with 3000 fb^{-1} luminosity. We scale the number of background and signal events according to the luminosity, and the limits are computed using a χ^2 analysis. As this analysis is able to probe light Z' and HL-LHC is expected to reach even smaller g_{B-L}, the cuts on displacements become more important.

Z' pair production via SM-like Higgs at ATLAS (ATLAS $h_1 \to 4l$) An ATLAS analysis [207] similarly studied the pair production of light exotic bosons through decays of the SM-like Higgs at $\sqrt{s} = 13$ TeV with an integrated luminosity of 36.1 fb^{-1}. Instead of only looking for muons, final states for either pairs of electrons or muons, i.e. either $4e, 4\mu$ or $2e2\mu$ final states are searched requiring the p_T of the three leading leptons to be above 20 GeV, 15 GeV and 10 GeV, respectively. The analysis gives an upper limit (U.L.) on the signal strength of the process $pp \to h_1 \to aa$ for the light neutral boson a with mass $m_a \approx$ 1-60 GeV, where the SM QCD resonance regions are removed due to large background [207]. This signal strength limit can be recast in other models by modifying the ratio of the SM-like Higgs production cross section in a given BSM model with the SM Higgs production cross section. In the $B-L$ model this ratio is $\cos^2 \alpha$. Therefore, we get upper limits on $\text{Br}(h_1 \to Z'Z')$,

$$\left(\frac{\sigma(h_1)}{\sigma(h_{\text{SM}})} \times \text{Br}(h_1 \to aa) \right)^{\text{U.L.}} = \cos^2 \alpha \times \text{Br}^{\text{U.L.}}(h_1 \to Z'Z'). \tag{7.5}$$

The kinematical acceptance α_{gen} is already accounted for in the experimental result, so we can directly derive the limits according to Eqn. (7.2). However, the analysis only searches for prompt final states, as discussed at the last section whereas the final states of Z' can be displaced if we probe low values of $m_{Z'} - g_{B-L}$. Therefore, to describe this underlying effect, we introduce a prompt efficiency function $\varepsilon_{\text{prompt}} \approx 1 - \exp(-1\ \text{mm}/L)$, where 1 mm is the threshold for lab frame displacement $\langle L \rangle$ of Z' within which we regard it is prompt, as the displacement becomes larger than the resolution of the vertex detector [299]. This method should be applicable at the HL-LHC as well.

Z' final state radiation from Z production at CMS (CMS FSR) The CMS analysis [205] reports on the search for an $L_\mu - L_\tau$ gauge boson Z' from a 4μ final state where the Z' is radiated in the final state as $pp \to Z \to Z'\mu^+\mu^- \to 4\mu$ (cf. Fig. 4.3 right) at the LHC with $\sqrt{s} = 13$ TeV and an integrated luminosity of 77.3 fb^{-1}. The analysis applies cuts such that at least two muons are required to have $p_T > 20$ GeV and at least one muon should have $p_T > 10$ GeV. The limits on the $L_\mu - L_\tau$ coupling $g_{L_\mu - L_\tau}$ are hence obtained for a neutral gauge boson with mass between 5 and 70 GeV. These limits can be easily converted to our model by requiring the same expected number of signal events from the two models, i.e., $\sigma_{\text{limit}} \propto {g_{B-L}}^2 \times \text{Br}(Z' \to \mu^+\mu^-)_{B-L} = g^2_{L_\mu - L_\tau}\text{Br}(Z' \to \mu^+\mu^-)_{L_\mu - L_\tau}$. Thus,

$$
{g_{B-L}}^2 = \frac{g^2_{L_\mu - L_\tau}}{3 \times \text{Br}(Z' \to \mu^+\mu^-)_{B-L}}, \tag{7.6}
$$

where $\text{Br}(Z' \to \mu^+\mu^-)_{L_\mu - L_\tau} = 1/3$ is taken [205]. For the HL-LHC, we project our limits on the coupling g_{B-L} to $L^{-1/4}$ as $\sigma_{\text{limit}} \propto L^{-1/2}$, where L is the integrated luminosity. As no light Z' with a few GeV masses are considered, no special consideration for displaced vertices are taken.

Z' resonance search at CMS (CMS dilepton) Finally, we discuss the most recent search for a narrow resonance in the dimuon final state by the CMS collaboration [182], $pp \to a \to \mu^+\mu^-$. The analysis uses two methods for different mass regions. For a light resonance between 11 and 45 GeV, it uses a scouting search in

96.6 fb^{-1} of data requiring $p_T(\mu) \gtrapprox 5$ GeV. For a heavier resonance with mass of 45 GeV to 200 GeV, a resonance search using the full 137 fb^{-1} Run 2 reconstructed level dataset is performed requiring $p_T(\mu) \gtrapprox 10$ GeV. Here, the data scouting technique, introduced by CMS in 2011, is the use of specialised data streams based on reduced event content, enabling LHC experiments to record unprecedented numbers of proton-proton collision events that would otherwise be rejected by the usual filters [300]. Therefore, this analysis is able to overcome the traditional limitations for a dilepton resonance search in a low mass region. This makes it possible to reach light resonances, which are otherwise difficult to look for. The original analysis focuses on a dark photon model with limits on the kinetic mixing $\varepsilon_{\text{dark}}$ and the dark photon mass m_{Z_D} are derived. Combining the two regions, it is able to give limits for Z_D mass between 11.5 GeV and 200 GeV. Recasting to the $B-L$ model can be realized by taking $g_{B-L} \approx e\,\varepsilon_{\text{dark}}$ [31] (see Sec. 5.1).

This dilepton resonance analysis is applicable to a wide range of signal models. Therefore, it is possible to constrain not just the resonance Drell-Yan production of Z' but the Higgs mediated Z' production as well. However, for the same g_{B-L}, the expected cross section for the Higgs mediated production is much smaller as it is suppressed by both g_{B-L} and $\sin\alpha$. Thus, we neglect this possibilities and only assume the final states are from $pp \to Z' \to \mu^+\mu^-$ process.

7.3 Sensitivity reach on $m_{Z'}$ and g_{B-L}

With the above recasting procedures of the existing searches, the upper 95% C.L. limits on the $B-L$ gauge coupling g_{B-L} are derived as a function of $m_{Z'}$. As before, we assume $\sin\alpha = 0.3$, for the Higgs mixing angle. This assumption is important for the pair production of the Z' from SM-like Higgs; for smaller Higgs mixing, the production rate will decrease and thus the limit on g_{B-L} is weakened.

As $\sigma(pp \to h_1 \to Z'Z') \propto g_{B-L}\sin(2\alpha)/2$, cf. Eqns. (7.1) and (7.2), the constraint on this parameter as a function of $m_{Z'}$ is illustrated in Fig. 7.3 for CMS $h_1 \to 4\mu$ and ATLAS $h_1 \to 4\mu$. CMS $h_1 \to 4\mu$ gives limits for $m_{Z'} \approx 0.25-8.5$ GeV, while ATLAS $h_1 \to 4\ell\,(\ell = e,\mu)$ covers $m_{Z'} \approx 1-60$ GeV with two

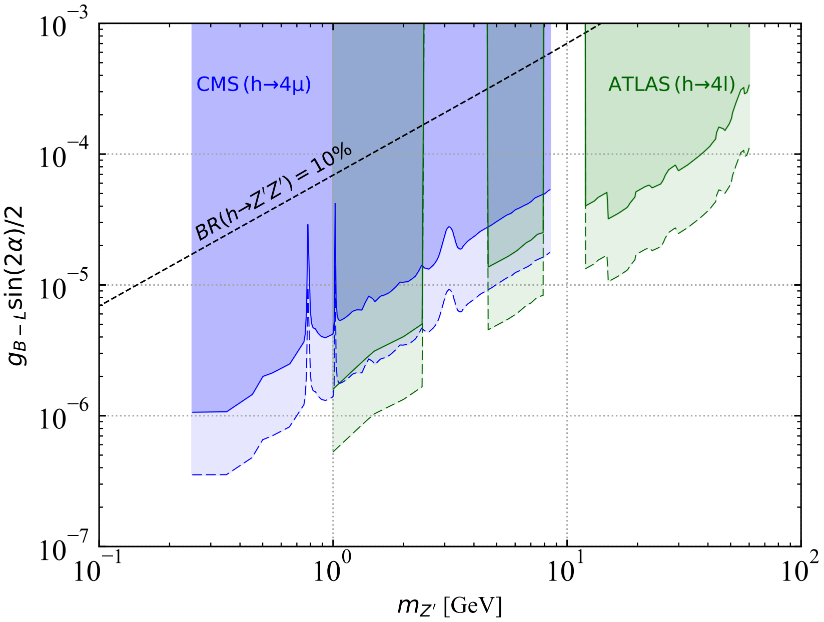

Figure 7.3: Constraints on the effective coupling $g_{B-L}\sin(2\alpha)/2$ as a function of the Z' mass $m_{Z'}$ recasted from the CMS $h_1 \to 4\mu$ [206] and ATLAS $h_1 \to 4\ell$ ($\ell = e, \mu$) [207] searches. The dark coloured regions are excluded by current data whereas the light coloured regions indicate the improvement expected by rescaling to a luminosity of 3,000 fb^{-1}. Also indicated is the contour for constant branching ratio $\mathrm{Br}(h_1 \to Z'Z') = 10\%$.

gaps between 2 GeV $< m_{Z'} <$ 5 GeV and 8 GeV $< m_{Z'} <$ 10.5 GeV due to QCD resonances removed to reduce background [207]. The CMS analysis instead estimates this background by identifying correlations between dimuon invariant mass pairs. Generally, the ATLAS analysis gives better limits than CMS. As can be seen from the model independent limits presented by both ATLAS and CMS, the limits on fiducial cross sections are very similar [206, 207]. However the phase space in which the fiducial cross section is computed is very different. In order to demonstrate the effect of phase space we can estimate the generator level acceptance for the two analysis. For this, we implemented the acceptance cuts as given in the two analyses, we find that the acceptance for the CMS analysis is about 25% while that for the ATLAS analysis is 50%. We also show the projections of the HL-LHC with 3,000 fb^{-1} luminosity as the lighter shaded regions delimited by a dashed curve in Fig. 7.3. This projection assumes a simple scaling of signal and background with luminosity. In addition to the above searches, the Higgs to invisible branching ratio limits can also be applied to this parameter if $h_1 \to Z'Z'$ is the only BSM Higgs decay mode available. Thus, the line in Fig. 7.3 corresponding to $\mathrm{Br}(h_1 \to Z'Z') = 10\%$, which is roughly the existing limit on the invisible Higgs decay branching ratio [132]. Moreover, if heavy neutrinos are lighter than half the SM Higgs mass, the decay to two N will also contribute. However, we neglect this possibility, as the branching ratio is negligible compared to $h_1 \to Z'Z'$ for the scenarios we consider (cf. Eqns. (7.2) and (8.1)).

Fig. 7.3 is particularly useful as there is a degeneracy between g_{B-L} and $\sin\alpha$ which can only be broken by individually searching for the presence or absence of extended Higgs or gauge sectors at experiments. Using this plot, it is possible to rescale and obtain values of g_{B-L} for any value of $\sin\alpha$. For instance, taking the approximately largest allowed value of the Higgs mixing as $\sin\alpha = 0.3$, we obtain the upper limits of $g_{B-L} \sim 3\times10^{-5}$ for $m_{Z'} = 1$ GeV, while $g_{B-L} \sim 5\times10^{-5}$ for $\sin\alpha = 0.2$ for the same $m_{Z'}$. On the other hand, taking the current existing limits on the gauge coupling, $g_{B-L} \lesssim 10^{-4}$ yields corresponding constraints on the Higgs mixing $\sin\alpha \lesssim 0.1$ which is very competitive to direct Higgs searches. However, as low values of g_{B-L} with light $m_{Z'}$ can result in long-lived Z' and the analyses we consider are mainly searching for prompt states, we cannot scale between g_{B-L} and $m_{Z'}$ for arbitrary low g_{B-L}.

In Fig. 7.4, we show the combined constraints on the $m_{Z'} - g_{B-L}$ parameter plane, setting $\sin\alpha = 0.3$. This allows to combine the aforementioned constraints from CMS $h_1 \to 4\mu$ and ATLAS $h_1 \to 4l$ with the CMS FSR and CMS dilepton constraints that only dependent on g_{B-L}. It is evident to see that the CMS FSR search gives the weakest limits, $g_{B-L} \gtrsim 0.01$ for $m_{Z'} \approx 5-60$ GeV. In the meantime, the $h_1 \to 4\mu$, $h_1 \to 4l$ yields the most stringent limits for 0.25 GeV $< m_{Z'} < 50$ GeV. Above $m_{Z'} \approx 50$ GeV, the CMS dilepton analysis gives the most stringent limits up to 70 GeV. To address the potential displaced vertex signatures from Z' decays, we also illustrate the contours of the mean lab frame $m_{Z'}$ displacement of 1 mm (solid grey line) and 10 cm (dashed grey line) when Z' is produced from the decays of h_1. Finally, $\mathrm{Br}(h_1 \to Z'Z') = 10\%$ is also shown for reference.

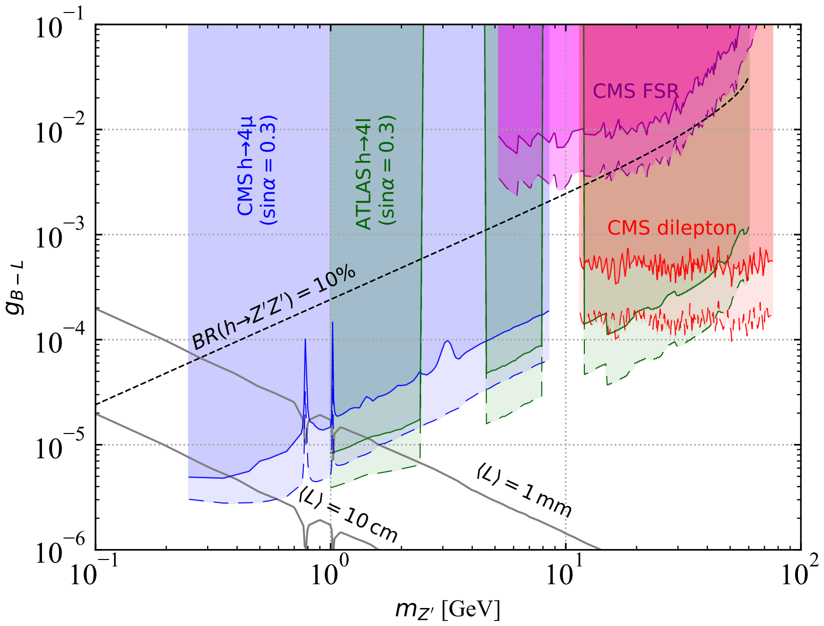

Figure 7.4: Constraints on the $U(1)_{B-L}$ gauge coupling g_{B-L} as a function of the Z' mass $m_{Z'}$ derived from the CMS $h_1 \to 4\mu$ [206], ATLAS $h_1 \to 4\ell$ ($\ell = e, \mu$) [207], CMS FSR [205] and CMS dilepton [182] searches. The dark coloured regions are excluded by current data whereas the light coloured regions indicate the improvement expected by rescaling to a luminosity of 3,000 fb^{-1}. Also indicated are the contours for constant branching ratio $\mathrm{Br}(h_1 \to Z'Z') = 10\%$ and constant average decay length $\langle L \rangle = 1$ mm, 10 cm, the latter applicable for the Higgs mode.

More specifically, the CMS $h_1 \to 4\mu$ analysis provides the strongest limits, $g_{B-L} \lesssim 5 \times 10^{-6}$, for Z' masses as low as 0.25 GeV. As the Z' becomes heavier, the production cross section decreases, thus these limits gradually weaken to $g_{B-L} = 1.8 \times 10^{-4}$ for $m_{Z'}$ = 8.5 GeV. The potential displaced vertex signatures are most relevant for the HL-LHC as a significant region of the parameter space is below the curve corresponding to $\langle L \rangle = 1$ mm where a simple scaling for luminosity is not applicable. This effect of displacement is illustrated by the 'flattening' of the g_{B-L} limit around $\langle L \rangle = 10$ cm in the $m_{Z'}$ region of 0.25 to 0.5 GeV for CMS $h_1 \to 4\mu$, as it allows for displacements up to 10 cm. For ATLAS $h_1 \to 4l$, a similar effect occurs for $\langle L \rangle \approx 1$ mm due to the promptness selection for $m_{Z'}$ between 1 to 2 GeV. Here, the effect is less visible because the ATLAS $h_1 \to 4\mu$ curve is steeper and the decay length of Z' is smaller. The effect of displacement is also reflected in the gain of limits due to luminosity, which is much smaller in the displaced region compared to the prompt region $m_{Z'} \gtrsim 0.5$ GeV at CMS, and similarly at ATLAS.

Finally, the current limits and its projection at the HL-LHC from the CMS dilepton analysis are also shown. It is also competitive to or better than the limits from the ATLAS $h_1 \to 4l$ for $m_{Z'} \approx 10-70$ GeV.

As we obtained several new limits from different sources, it is also interesting to compare their behaviour for different masses of Z'. It is evident to find that the limits from the FSR and CMS dilepton searches are roughly constant over $m_{Z'}$, whereas the limits from Higgs mediated processes get weaker as $m_{Z'}$ increases. This is because the cross section of Higgs mediated processes is dominantly controlled by $\mathrm{Br}(h_1 \to Z'Z')$, which depends on $g_{B-L}/m_{Z'}$ as seen from Eqns. (7.1) and (7.2).

Given our discussion so far, it is clear that it will be difficult to probe large Z' displacements in the $B-L$ model unlike in the dark photon case. The production and decay of $B-L$ Z' are controlled by the same parameters g_{B-L}, which limits the sensitivity of LHC searches due to rapidly falling cross sections. However, if we turned on the $Z-Z'$ mixing $\tilde{g}$ in the $B-L$ model, it would scale similarly.

Our limits can be compared with the other constraints as described in Sec. 5.1. In Fig. 7.5, this comparison is shown for Z' with a mass between 0.1 GeV to 1000 GeV. In this figure, apart from the limits obtained in this chapter, we also show existing limits mainly from dark photon searches as described in Sec. 5.1 (see Fig. 5.2), the limits from the CONTUR framework as discussed in Sec. 6.3 (cf. Fig. 6.2 (top)), the limits from CMS dilepton searches [182] for $m_{Z'} \approx 110-200$ GeV, and high mass dilepton resonance searches (CMS high mass) [181]. The contours for a constant proper decay length $L_0 = 1$ mm, 10 cm and 10 m are also shown. For light Z' with a mass from 0.25 to 1 GeV, our analyses from Higgs mediated processes improve the current limits by an order of magnitude. For slightly larger masses, our analyses still win over the current limits. For $m_{Z'}$ ranging from 10 to 60 GeV, the Higgs mediated channel as well as the recent CMS dilepton search in the dimuon final state still show better limits to the existing limits (mainly from LHCb dark photon searches). Finally, we also show the limits from interpreting recent CMS high mass searches [181]. They arise from the ratio of the dilepton resonance cross

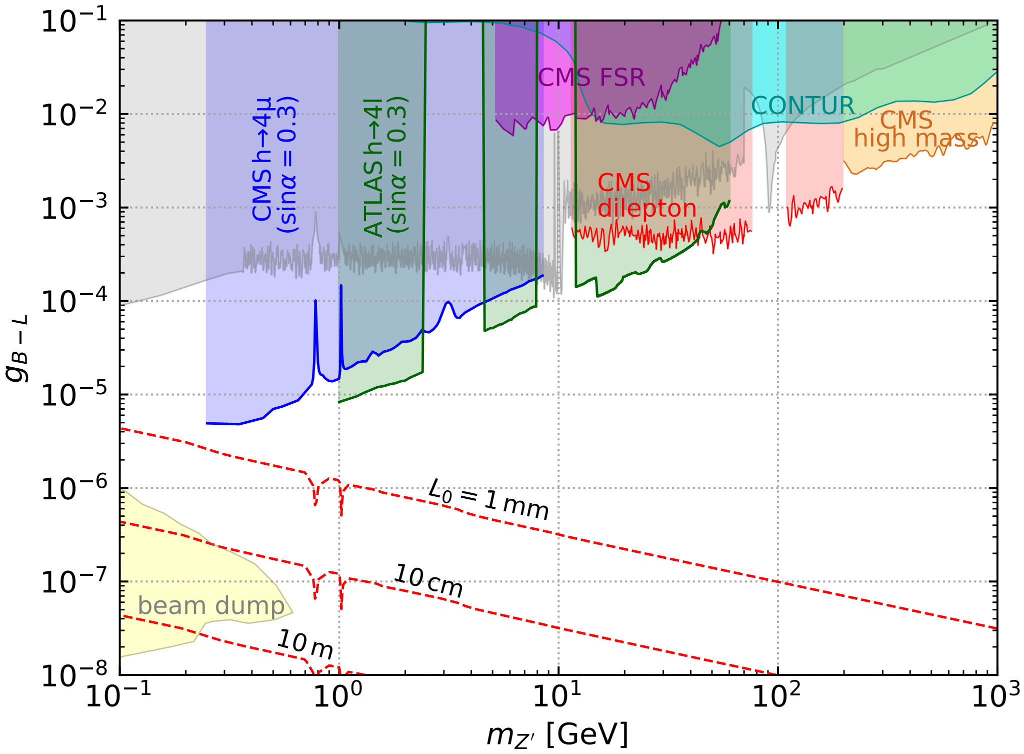

Figure 7.5: Summary of constraints on the $U(1)_{B-L}$ gauge coupling g_{B-L} as a function of the Z' mass $m_{Z'}$. The grey area represents existing constraints whereas the coloured regions represent the constraints discussed in this thesis derived from the CMS $h_1 \to 4\mu$ [206], ATLAS $h_1 \to 4\ell$ ($\ell = e, \mu$) [207], CMS FSR [205] and CMS dilepton [182] searches. Also shown are the constraints derived from the CMS dilepton search [181] (CMS high mass) and from LHC SM measurements using `CONTUR` [156] (CONTUR). For the Higgs mediated modes we assume a Higgs mixing angle $\sin\alpha = 0.3$.

section to the SM Z to dilepton production cross section. Thus, taking the cross section $\sigma(pp \to Z \to \mu^+\mu^-)$ to be 1870 pb and multiplying it to the constraint on the ratio, we derive the limit on g_{B-L}. The corresponding ATLAS analysis [58] gives similar limits. The figure also illustrates the gaps in the dilepton resonance searches at ATLAS and CMS. In the region $m_{Z'} \approx 10$ GeV, only weak constraints from the CMS FSR analysis can be derived, while the region around the Z mass remains unconstrained by current LHC searches. As discussed in [156] and Chapter 6, using the `CONTUR` framework of interpreting LHC SM measurements can still be used to extract constraints, albeit comparatively weaker.

Chapter 8

Displaced Vertex Searches

As mentioned in Chapter 3 and 6, the heavy neutrinos in our model can result in signatures with displaced vertices. In this chapter, we focus on such displaced vertex signatures at the LHC, also in proposed detectors dedicated to long-lived particle searches. Together with the other approaches for the gauge sector and the scalar sector, we are able to probe all six free parameters of the $B-L$ model.

We here focus on a heavy neutrino which only couples to the muon and in the following we omit any subscript, e.g. $N \equiv N_\mu$ with $V_{\mu N} \neq 0$. The main reason for this choice is that the muon chamber of the CMS and ATLAS detectors is placed meters away from the interaction point (IP), thus it is especially sensitive the displaced vertices with emerging muons.

At the LHC, the most studied heavy neutrino production mechanism is through the SM W and Z via the active-sterile mixing, $pp \to W^\pm \to Nl^\pm$ and $pp \to Z \to N\nu$. From the observation of the light neutrino masses, we assume 0.01 eV $< m_\nu <$ 0.3 eV (see Sec. 4.2) and from the Type-I seesaw relation $m_\nu \approx V_{lN}^2 m_N$ (Eqn. (2.53)), heavy neutrinos at the EW scale $m_N \sim 1-100$ GeV would require $V_{\mu N} \approx 10^{-6}$. Such a mixing for heavy neutrinos results in them being long-lived with proper decay length $L_N \gtrsim 1$ cm (see Eqn. (8.3)). As the production cross section drops with the square of the active-sterile mixing, the LHC is not sensitive to such long-lived heavy neutrinos through this production mechanism. Displaced vertices of sterile have nevertheless been studied at the LHC, see Fig. 5.4 (ATLAS) [84], albeit for much larger mixing. Instead, we consider long-lived heavy neutrinos pair pro-

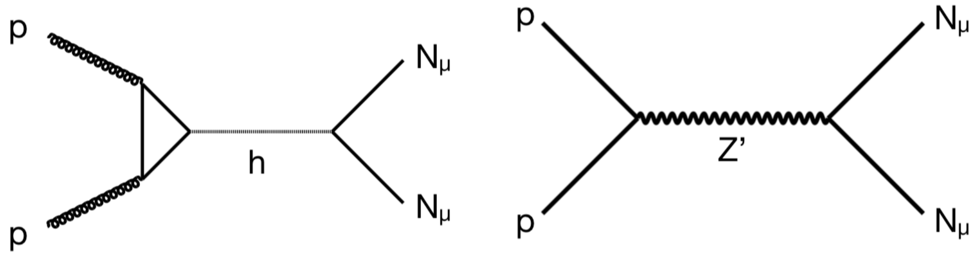

Figure 8.1: Left: Feynman diagram for the pair-production of a heavy neutrino from SM Higgs decays, $pp(gg) \to h_1 \to NN$. Right: Feynman diagram for the pair-production of a heavy neutrino from Z' decays, $pp \to Z' \to NN$.

duced from the decay of either a SM-like Higgs h_1 or the $B-L$ gauge boson Z', $pp \to h_1, Z' \to NN$. These processes are not dependent on the active-sterile mixing, thus can potentially reach the seesaw regime. We start with calculating the cross section of heavy neutrino production using event generators, then simulate the displaced vertex from the heavy neutrinos decays and estimate the event rate and geometric efficiencies for different detectors. For the detailed simulation of the displaced vertex event, we include detectors such as CMS [85, 87], LHCb [301], MATHUSLA [302], FASER [303, 304], MAPP [305], and CODEX-b [306] at the current LHC and HL-LHC as well as detectors at future lepton colliders including the ILC [307, 308] and CEPC [226, 309]. Their sensitivities are obtained and compared in the end.

8.1 Heavy neutrino production and decay

We consider the heavy neutrinos pair-produced either from the SM-like Higgs $pp \to h_1 \to NN$ (Fig. 8.1 (left)) or Z' decays $pp \to Z' \to NN$ (Fig. 8.1 (right)). The processes $pp \to h_1, Z' \to N\nu$ are also possible in principle. However, they are very rare as the active-sterile mixings are tiny, thus neglected. The production and decay of the heavy neutrino from SM-like Higgs or Z' decays depends on all of the three sectors of the free parameters in principle. In this chapter, we focus on the neutrino sector, and set the Higgs mixing to be its approximately experimental max allowed value $\sin\alpha = 0.3$ and the $B-L$ coupling at $g_{B-L} = 10^{-3}$ for 10 GeV $< m_{Z'} <$ 100 GeV to get an appreciable cross section for $pp \to h_1 \to NN$ and $pp \to Z' \to NN$ and avoid non-perturbative effects. For simplicity, when we consider heavy neutrinos from Higgs decays, we assume the Z' is decoupled and vice versa.

Pair-production of heavy neutrinos from Higgs decays Heavy neutrinos can be pair-produced from SM-like Higgs decays through their Yukawa couplings when the Higgs mixing is nonzero. At the leading-order, the coupling of h_1 with two heavy neutrinos $\kappa_{h_1NN} = y^M \sin\alpha\cos^2\theta_\nu \simeq y^M \sin\alpha \simeq \frac{m_N}{\tilde{x}}\sin\alpha$, where the y^M is the corresponding Majorana Yukawa coupling and θ_ν is the active-sterile neutrino mixing angle, $\cos\theta_\nu \simeq 1$ as it is tiny. Therefore, the production cross section of heavy neutrinos in this mode is proportional to ${m_N}^2$, inversely proportional to $\tilde{x}^2$, and additionally depend on the phase space factor bounded by $m_{h_1} > 2\, m_N$.

The decay width of $h_1 \to N\, N$ is approximately [28],

$$\Gamma(h_1 \to NN) = \frac{2}{3}\sin^2\alpha\frac{m_N^2}{\tilde{x}^2}\frac{m_{h_1}}{8\pi}\left(1-\frac{4m_N^2}{m_{h_1}^2}\right)^{3/2}. \tag{8.1}$$

In the $B-L$ model, the SM-like Higgs production is modified by a factor of $\cos^2\alpha$. When the exotic Z' is heavier than the SM-like Higgs thus decouples from this mode, the branching ratio of h_1 decays into two heavy neutrinos can be expressed as,

$$\mathrm{Br}(h_1 \to NN) = \frac{\Gamma(h_1 \to NN)}{\Gamma(h_{\mathrm{SM}})\cos\alpha^2 + \Gamma(h_1 \to NN)}, \tag{8.2}$$

where $\Gamma(h_{\mathrm{SM}}) \approx 4$ MeV [132]. As can be seen in Eqns. (8.1) and (8.2), the branching ratio $\mathrm{Br}(h_1 \to NN)$ is independent of the active-sterile neutrino mixing $V_{\mu N}$. The cross section $\sigma(pp \to h_1 \to N\, N) = \sigma(pp \to h_1) \times \mathrm{Br}(h_1 \to NN)$ is shown in Fig. 8.2 (left) as a function of m_N and $\sin\alpha$. The dependence on the heavy neutrino mass m_N balances the effects from the associated Yukawa coupling $y^M = \frac{m_N}{\tilde{x}}$ and smaller phase space $\left(1-4m_N^2/m_{h_1}^2\right)^{3/2}$ for larger m_N. Thus the cross section peaks at about $m_N = 40$ GeV for a fixed $\sin\alpha$. With some choices of the combinations of the parameters, we can obtain a cross section for $pp \to h_1 \to N\, N$ of about 50 fb for $\sin\alpha \sim 0.3$. Therefore, the current LHC with about 100 fb^{-1} luminosity should be

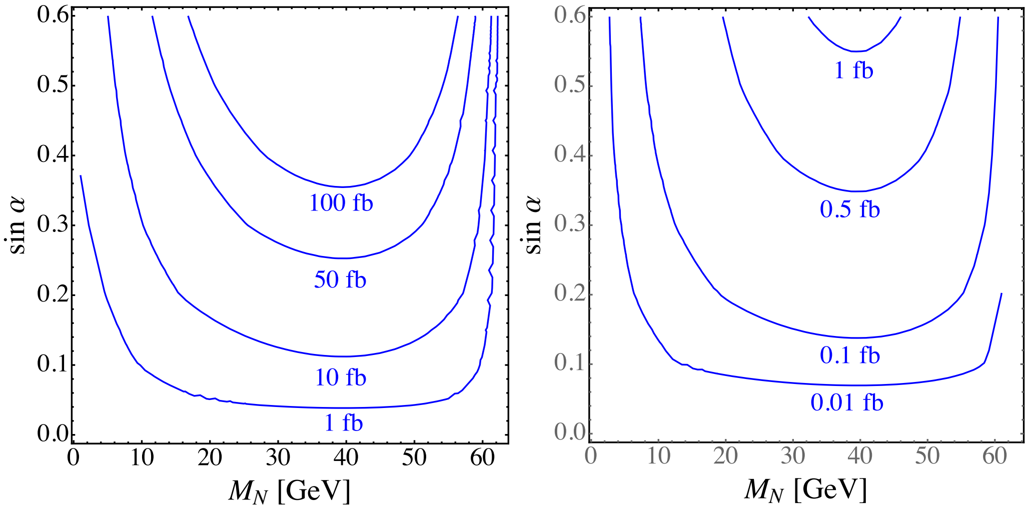

Figure 8.2: Left: $\sigma(pp \to h_1 \to NN)$ as a function of the mass for the heavy neutrino m_N and the Higgs mixing $\sin\alpha$ at the 13 TeV LHC. Right: $\sigma(e^+e^- \to Z^* \to Zh_1 \to Z + NN)$ as a function of the same parameters at an electron-positron collider with a collision energy of $\sqrt{s} = 250$ GeV.

sensitive to this process.

We show the cross section for a lepton collider with $\sqrt{s}$ = 250 GeV as well for comparison (initial state radiation (ISR) not considered for simplification). At the lepton collider with $\sqrt{s}$ = 250 GeV, Higgs-Strahlung, $e^+e^- \to Z^* \to Zh_1$ is the dominant Higgs production process. The cross section of this process is expected to be 240 fb when $\sqrt{s} = 250$ GeV [226]. In our model, this would give the cross section $\sigma(e^+e^- \to Z^* \to Zh_1) \approx 240$ fb $\times \cos^2\alpha$. Hence, as illustrated in the Fig. 8.2 (right), the total cross section of heavy neutrino production in this mode is roughly 200 times smaller compared to the LHC.

Pair-production of heavy neutrinos from Z' decays We have already discussed the main production mechanisms of the Z' at the LHC in Sec. 7.1. Z' is mainly produced through the $s-$channel Drell-Yan process, $pp \to Z'(\to l^+l^-)$ at the LHC. Therefore, we only consider the Drell-Yan Z' production in this chapter. As discussed previously, for a Z' with mass below and around the QCD scale which is 10 GeV, the cross section can not be simulated well because the process is not perturbative. We therefore only consider 10 GeV$< m_{Z'} <$ 100 GeV, so the cross section is still appreciable and calculable at the 14 TeV LHC. We take 14 TeV LHC to account for the upgraded collision energy for the HL-LHC which is mostly discussed in the

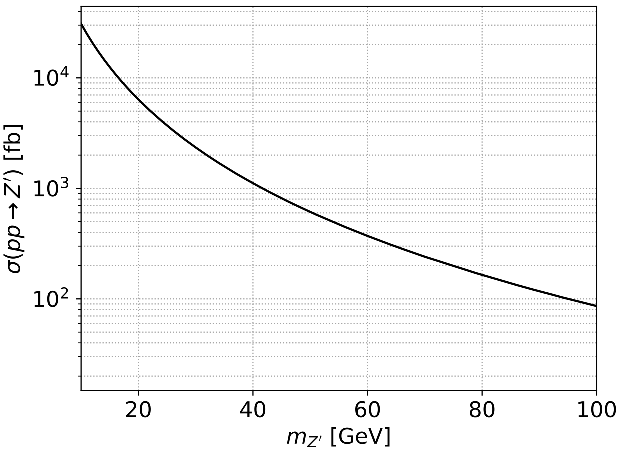

Figure 8.3: Production cross section of $pp \to Z'$ at $\sqrt{s} = 14$ TeV with $g_{B-L} = 10^{-3}$.

following calculations for this channel. We show the cross section of Z' production in Fig. 8.3. The production cross section can vary from a few pb for Z' just heavier than 10 GeV and $\mathcal{O}(100)$ fb for heavy Z' when g_{B-L} coupling is fixed at 10^{-3}.

Once the Z' is produced, heavy neutrinos can be produced from its decay. Unlike in Chapter 6 where $\frac{m_N}{m_{Z'}} = 0.2$ is assumed, here we fixed $\frac{m_N}{m_{Z'}} = 0.3$ to remain only one free parameter. This mass relation is imposed to keep the m_N of the order of EW scale and such that the phase space factor of $Z' \to N\,N$ is still appreciable. The partial decay width for $Z' \to N\,N$ is shown in Eqn. (4.2), and the branching ratio of the Z' decays is shown in Fig. 4.4. The branching ratio for three generations of degenerate heavy neutrinos are added up. As we are only interested in the generation of the heavy neutrino that couples to the muon, its branching ratio is thus about 6-7% for fixed $\frac{m_N}{m_{Z'}} = 0.3$ in the regions of our interests. Thus, as $\sigma(pp \to Z' \to N\,N) = \sigma(pp \to Z') \times \mathrm{Br}(Z' \to N\,N)$ and the production cross section of heavy neutrino via this channel varies from about 1 pb to about 10 fb in the mass range 10 GeV $< m_{Z'} <$ 100 GeV at the 14 TeV LHC, leading to potential sensitivity.

Heavy neutrino decays The heavy neutrino is able to decay to various SM final states through active-sterile neutrino mixing. We consider a heavy neutrino which only mixes to the μ. Assuming $m_N < m_{h_2}, m_{Z'}$, and $m_N \lesssim m_W$, the N decays dominantly to $\mu q\bar{q}$ and $\mu^+\mu^-\nu_\mu$ for final states containing muons, cf. Fig. 4.6. It is worth to reiterate that all decay processes are through the active-sterile mixing $V_{\mu N}^2$. The branching ratios for the heavy neutrino decays into different final states thus do not depend on the mixing. [1]

We use `MadGraph5_aMC@NLO` v.2.5.5 [146] to calculate the branching ratios of the heavy neutrinos for $m_N \lesssim m_W$ roughly considering the hadronization effects for N decays to jets. The thresholds are calculated approximately due to the relatively large step size between the simulated m_N values. For example, we only calculated the branching ratios of N for $m_N = 10^{-2}$ GeV and $m_N = 10^{-1}$ GeV for 10^{-2} GeV$< m_N < 10^{-1}$ GeV. The different channels open when they are kinematically allowed. The branching ratios change near the m_W threshold, because the $N \to W^{\pm} l^{\mp}$ decays become nearly on-shell [188]. The result is illustrated in Fig. 8.4 which shows that the N decays dominantly to $\nu\nu\nu$ for $m_N \lesssim 0.1$ GeV and to $\mu q\bar{q}$ for $m_N \gtrsim 1$ GeV. The proper decay length of the N for $m_N \lesssim m_W$ is approximately [90, 188] (see Sec. 4.2)

$$L_N \approx 0.025\ \mathrm{m} \cdot \left(\frac{10^{-6}}{V_{\mu N}}\right)^2 \cdot \left(\frac{100\ \mathrm{GeV}}{m_N}\right)^5 . \tag{8.3}$$

The lab frame decay length should be modified by the boost factor $\beta\gamma$ for different processes. From the above equation, the heavy neutrino can have a decay length of $\mathcal{O}$ (mm) for $m_N \approx 30$ GeV and $V_{\mu N} \approx 10^{-4}$. For smaller mixing, like in the naive seesaw estimation $V_{\mu N} \approx 10^{-6}$ for EW scale heavy neutrinos $m_N \sim 1 - 100$ GeV (see Sec. 2.4), decay length of more than meters are possible, potentially resulting in signatures of displaced vertices at the LHC and other colliders. For even smaller mixing, the heavy neutrino can decay outside the detector leading to a missing energy signature. For heavy neutrinos produced from a very light Z', the boost factor can be large resulting in even longer lab frame decay lengths from the above discussions.

---

[1] This is no longer true if we allow the neutrino to couple to more than one lepton flavour. The branching ratios will then depend on the ratios of mixing strength $V_{\alpha N}/V_{\beta N}$.

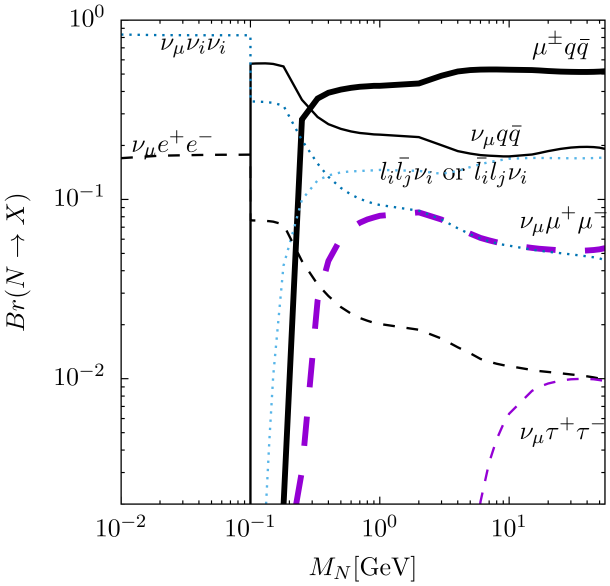

Figure 8.4: Decay branching ratios $\mathrm{Br}(N \to X)$ of the heavy neutrino N into the denoted channels X as a function of m_N. Here, $i, j = e, \mu, \tau$ denotes lepton flavour with $i \neq j$ and the heavy neutrino is assumed to mix only with the light muon neutrino, $V_{\mu N} \neq 0$, $V_{e,\tau N} = 0$. In this case, the branching ratios are independent of $V_{\mu N}$. The thresholds are calculated approximately due to the relatively large step size between the simulated m_N values.

8.2 Displaced vertex event simulation

There are multiple existing and proposed detectors that can potentially detect displaced vertices. Here we discuss a detailed simulation for both the N from the SM-like Higgs and Z' to calculate the approximate displaced vertex event rate at these detectors. For each detector, we first use an event generator to generate the corresponding events at the generator level with initial kinematic cuts from any trigger requirement (for the Z' channel, the simulation is done at hadronization and shower level). Then, we put the geometric cuts to estimate the geometric acceptance of the corresponding detector. For simplicity, we do not perform a detector simulation and the detector efficiency is assumed to be 100% for an optimistic estimation. In the following discussions, the details of the event generation for the two channels and the trigger and geometrical cuts for each detector are introduced.

Event generation To simulate events, we use the model file as introduced in Chapter 3 and feed it to the Monte Carlo event generator `MadGraph5_aMC@NLO` v.2.5.5 (`MadGraph5_aMC@NLO` v.2.6.3 for the Z' channel). After the event generation at the generator level, initial and final state parton shower, hadronization, heavy hadron decays, are considered and handled by `PYTHIA` v8.235 [298] only for Z' channel. A detector simulation is not carried out at this point, while idealistic displaced vertex simulation at different detectors will be discussed in the following sections. As both $m_{Z'}$ and m_N are free parameters, we fix $m_N = 0.3 \times m_{Z'}$ to reduce the parameter space. This ratio ensures that there is no appreciable suppression from the $Z' \to NN$ phase space, the heavy neutrinos are still heavy enough to decay to a pair of muons and they are not too light to escape the detector. Nevertheless, we will also determine the sensitivities if m_N is varied independently of $m_{Z'}$ in Fig. 8.14.

Generally, to fully reconstruct the displaced vertex and estimate the event rate, we apply kinematic and geometric selection cuts according to the different detectors. This will reduce the signal events as $\sigma \times L \times \varepsilon_{\text{kin}} \times \varepsilon_{\text{geo}}$ with the production cross section σ, the luminosity L, the kinematic and geometric efficiency ε_{kin} and ε_{geo}, respectively. For both channels, we only require one of the N to decay leading to a signature with a *single displaced vertex*, while the other N can decay to any possible final state, or even escape the detector. This is justified as a single displaced vertex signature is already distinct enough and events with *two displaced vertices* are rarer. In the following discussions, we introduce the kinematic cuts for specified selection criteria and the geometric cuts for different detectors.

CMS ATLAS and CMS are two general purpose detectors at the LHC which are both able to detect displaced vertex signatures with intermediate displacements for $L_N \sim \mathscr{O}(10)$ cm [87]. For simplicity, we only consider CMS. Considering the muon final states, the signal can be classified as $pp \to h_1, Z' \to NN \to N\mu^{\pm} jj$ (Channel 1) and $pp \to h_1, Z' \to NN \to N\mu^{+}\mu^{-}\nu$ (Channel 2), respectively. Both channels will be simulated at generator level for the heavy neutrinos from SM-like Higgs decays, while Channel 2 is discussed and chosen for a detailed displaced vertex simulation for both h_1 and Z' in the following sections.

In the literature [28, 310, 311], various selection criteria were employed for similar signatures. Targeting on a prompt lepton (muon) and a heavy neutrino from the decays of a W boson, Ref. [310] proposes a kinematical cut for the signal containing a muon jet which is a reconstructed object with more than one muon track within a cone of radius $R_0 = 0.5$, i.e., the muons are collimated from $pp \to W^\pm \to \mu^\pm N \to \mu^+\mu^+\mu^-\nu_\mu$ or $\mu^+\mu^+jj$. Nonetheless, this is not applicable for the N pair produced from a SM-like Higgs or Z' decay and the muons produced from the subsequent decays of N are generally un-collimated, as it is from the decay of a not too light N.

Ref. [311] discusses a characteristic signal for $\mu^\pm jj$ orginating from displaced decays of a neutralino which can be regarded as our Channel 1 signal. The selection criteria applied on the transverse momentum p_T, pseudo-rapidity η and isolation ΔR on the muon, which is to be referred as *one-muon event* to identify a candidate both in the inner detector and the muon spectrometer, are

$$p_T(\mu) > 50 \text{ GeV},\ |\eta| < 1.07,\ \triangle R = \sqrt{(\Delta\phi)^2 + (\Delta\eta)^2} < 0.15,\ |d_0| > 1.5 \text{ mm}. \tag{8.4}$$

$\Delta\phi$ and $\Delta\eta$ is the difference between the azimuthal angle (pseudorapidity) of the reconstructed muon and that of the muon identified by the trigger. Therefore, the observed muon related to the muon identified by the trigger is ensured by the small ΔR requirement. The cut on the transverse distance d_0 (defined in Sec. 4.1) makes sure that the muons are produced via a displaced vertex (see the discussions in Sec. 4.1).

In Ref. [28], softer p_T cuts have been applied requiring two muons in the final states from the same signal processes Channel 1 and 2, $pp \to h_1(Z') \to NN \to N\mu^+\mu^-\nu_\mu$ and $\mu^\pm jj\mu^\pm jj$. The kinematic cuts used (Channel 2 with $\mu\mu\nu$ from *single displaced vertex* or Channel 1 with μjj from *two displaced vertices*) that satisfy the following cuts for the two muon tracks are

$$\begin{gathered} p_T(\mu_1) > 26 \text{ GeV},\ \ p_T(\mu_2) > 5 \text{ GeV},\ \ |\eta| < 2.0 \\ \Delta R > 0.2,\ \ \cos\theta_{\mu\mu} > -0.75. \end{gathered} \tag{8.5}$$

The cuts on the angle between the muons $\cos\theta_{\mu\mu}$ and correlating the corresponding

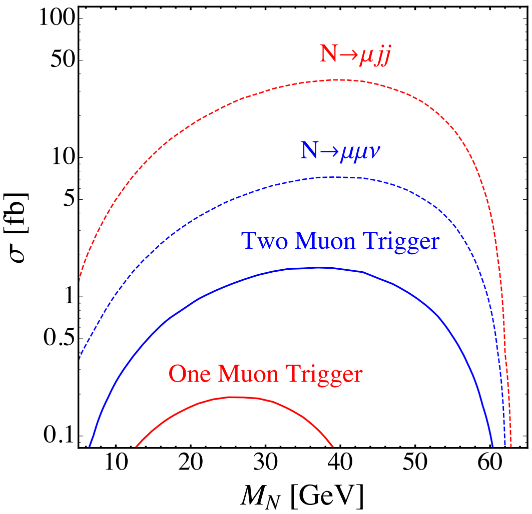

Figure 8.5: Cross section for Channel 1 and Channel 2 as a function of the heavy neutrino mass before (dashed) and after (solid) the corresponding kinematical cuts. The dashed red line represents the theoretical prediction for $\sigma(pp \to h_1 \to NN \to N\mu jj)$, while the solid red line corresponds to the cross section after the one muon selection, Eqn. (8.4). Likewise, the dashed blue line gives $\sigma(pp \to h_1 \to NN \to N\mu\mu\nu)$, and the solid blue line corresponds to the cross section after the two muon selection, Eqn. (8.5)

hits with the beam collision time make sure that the background from cosmic ray muons is removed [87]. Additional cuts for $|\Delta\Phi| < \pi/2$ in the azimuthal angle between the vector of the momentum of the dilepton and from the primary vertex to the dilepton vertex has been implemented to distinguish the data in the control region and signal region in Ref. [85, 87]. Nonetheless, this is not relevant for us as we do not employ it in our simulation. We will call such an event a *two-muon event*.

For Channel 1, although a *two-muon event* can be applied requiring *two displaced vertices*, the probability is generally smaller so we start with requiring only a *single displaced vertex* for both channels. In Fig. 8.5, the cross section for Channel 1 (μjj) and Channel 2 ($\mu\mu\nu$) from the SM-like Higgs decays ($pp \to h_1 \to NN$) before and after applying the cuts from a *one-muon event* (Eqn. (8.4)) and *two-muon event* (Eqn. (8.5)) explicitly, is illustrated and compared. Even though the branching ratio for N to decay into μjj in Channel 1 is higher, this can not balance the advantage of using a softer p_T cut for Channel 2 requiring a *two-muon event*, leaving the cross section after corresponding kinematical cuts for Channel 2 larger than Channel 1. Therefore, we only simulate the detector geometry for Channel 2 with the *two muon event* and we only require a *single displaced vertex*. Although the muons from the Z' channel can be more boosted as we consider $m_{Z'} = 10 - 100$ GeV, the cross section of Channel 2 with *two-muon event*s is still larger, and we only simulate this combination requiring a *single displaced vertex* for the Z' channel as well.

After the kinematic cuts, the geometric cuts characterising the detector geometry for the CMS detector are applied to calculate the displaced vertex rate. The displaced vertices in the CMS detector are required to be located in the Region 1 and Region 2 as defined in Fig. 4.1. The inner tracker can track the displaced vertex signatures via the decay of the heavy neutrinos as they are recorded by the tracks of muons from their decays. This region is referred to as Region 1, which is the inner (grey) area of Fig. 4.1. The tracks of the muons from the heavy neutrino decays can also be registered in the muon chamber [28]. The region within which the parent heavy neutrinos can decay, roughly including the HCAL and ECAL, and the inner region of the muon chamber, is illustrated by the outer (orange) area (Region 2).

The geometric cuts can be summarised approximately regarding the CMS detector as an idealistic cylinder (also in Tab. 8.1),

$$\begin{aligned}
\text{Region 1:} \quad & 10\ \text{cm} < |L_{xy}| < 50\ \text{cm},\ |L_z| < 1.4\ \text{m}, && (8.6)\\
& d_0/\sigma_d^t > 12,\ \sigma_d^t = 20\ \mu\text{m}, \\
\text{Region 2:} \quad & 0.5\ \text{m} < |L_{xy}| < 5\ \text{m},\ |L_z| < 8\ \text{m},\ d_0/\sigma_d^t > 4,\ \sigma_d^t = 2\ \text{cm}, && (8.7)
\end{aligned}$$

where $L_{xy,z}$ are the transverse and longitudinal distances from the IP and σ_d^t is the transverse resolution of the detector as defined in Sec. 4.1.

LHCb From an existing LHCb displaced vertex search [177, 301], displaced vertex signatures at the LHCb can be captured at its VELO and TT tracking station (defined in Sec. 4.1) via a trigger requirement with,

$$\begin{aligned}
& N(\mu) = 1,\ N(j) > 0,\ p_T(\mu) > 12\ \text{GeV}, && (8.8)\\
& M[\mu jj] > 4.5\ \text{GeV},\ 2 < \eta(\mu, j) < 5.
\end{aligned}$$

As the trigger requires $N(j) > 0$, we only use $N \to \mu^\pm jj$ for the LHCb detector. Other decay channels such as $N \to \mu^+\mu^-\nu$ can pass this requirement when ISR or FSR emits jets, however as the branching ratios are smaller comparing to $N \to \mu^\pm jj$ and smaller production cross section for ISR and FSR processes, these channels are not taken into account. As for the geometrical cuts, we follow the description in Ref. [177]:

- $\arctan \frac{L_{xy}}{L_z} < 0.34$ for the angle of the displacement to the beam line.
- Region 1 for LHCb requires the heavy neutrino to decay within the VELO, characterised by 0.02 m $< r < 0.5$ m, where r is the radial distance to the IP, and $L_z < 0.4$ m. We assume the reconstruction efficiency of the signal to be 100%.
- Region 2 for LHCb requires decays within the TT tracking station where 0.005 m $< r < 0.6$ m and $L_z < 2$ m. $r_{\text{min}} = 0.005$m is taken as the b-quark backgrounds is appreciable for $r \lesssim 0.005$m. Outside Region 1, we assume the signal reconstruction efficiency to be 50%, because of the larger background from the detector and blind spots. While an efficiency of 100% is used for the intersect of the Region 1 and 2.

MATHUSLA Several designs of detectors at the lifetime frontier have been proposed to enable the HL-LHC to probe long-lived particles. We study multiple such proposals. Among them, MATHUSLA (MAssive Timing Hodoscope for Ultra Stable neutraL pArticles) incorporating a large detector on the ground surface above the CMS or ATLAS IPs, is capable of detecting ultra long-lived particles with a few hundred meters of displacement from the IP [302,312,313]. We apply the following geometric selection cuts for this detector,

$$-100\text{ m} < L_x < 100\text{ m},\ 100\text{ m} < L_y < 120\text{ m},\ 100\text{ m} < L_z < 300\text{ m}. \tag{8.9}$$

Because of its design, the angular coverage of MATHUSLA is comparatively small, leading to a poor geometric acceptance ε_{geo}. Nonetheless, it can potentially be sensitive to very small active-sterile neutrino mixing due to its large distance from the IP.

FASER The FASER (the ForwArd Search ExperRiment) detector is an approved new detector to be operational in Run 3 of the LHC. It is situated 480 meters away from the IP of ATLAS centred on the beam line. We put geometric cuts following its design [303] in its two phases:

- FASER 1: A cylinder with 1.5 m depth in the beam direction and a 0.1 m radius for its transverse extent at the 150 fb^{-1} LHC.
- FASER 2: A cylinder with 5 m depth in the beam direction with a 1 m radius in transverse direction at the 3000 fb^{-1} HL-LHC.

Due to the small angular coverage, FASER 1 will not be sufficiently sensitive to heavy neutrinos in the $B-L$ model, thus only simulations for FASER 2 are performed.

MAPP Within the MoEDAL experimental setup [305], there is a proposal for a sub-detector focusing on detecting long-lived particles called the MAPP (Monopole Apparatus for Penetrating Particles) detector. In its initial design, it is going to use a tunnel 50 meter away from the IP of the LHCb, with 7 to 10 meters depth covering 5 to 25 degree of angle to the beam-line at a 300 fb^{-1} (at the LHCb IP), 14 TeV HL-LHC. The original design of the detector contains two arrays of scintillator bars (with detector volume of 1 m^3) and the whole detector can move inside the whole tunnel to capture long-lived particles with different angles while lowering the effective luminosity. With the above design, MAPP will not be able to probe heavy neutrinos in the $B-L$ model due to its small angular coverage. In Ref. [91], we used a hypothetical version of the MAPP detector making use of the whole tunnel referred to as MAPP* and estimated its sensitivity.

In parallel, the MoEDAL collaboration has also updated designs equipping the whole tunnel with a detector [314]. There are two stages: MAPP-1 at the LHC Run 3 with smaller volume and 30 fb^{-1} luminosity. It is a box characterised by eight points:

$$\begin{aligned}
&\text{Point 1}(4.00,\ \ 1,-61.39),\ \text{Point 2}(6.19,\ \ 1,-56.89), \\
&\text{Point 3}(3.27,\ \ 1,-52.82),\ \text{Point 4}(5.42,\ \ 1,-48.31), \\
&\text{Point 5}(4.00,-2,-61.39),\ \text{Point 6}(6.19,-2,-56.89), \\
&\text{Point 7}(3.27,-2,-52.82),\ \text{Point 8}(5.42,-2,-48.31),
\end{aligned} \tag{8.10}$$

where Point X (x,y,z) meter is the corresponding coordinate to the LHCb IP in the x, y, z axis, respectively. MAPP-1 will be installed for Run 3 of the LHC [315].

MAPP-2 with an about three times larger volume is a planned extension for the HL-LHC. Similarly, it is a box characterised by eight points:

$$\begin{aligned}
&\text{Point 1}(4.00,\ \ 1,-61.39),\ \text{Point 2}(16.53,\ \ 1,-35.45), \\
&\text{Point 3}(3.27,\ \ 1,-52.83),\ \text{Point 4}(12.24,\ \ 1,-33.63), \\
&\text{Point 5}(4.00,-2,-61.39),\ \text{Point 6}(16.53,-2,-35.45), \\
&\text{Point 7}(3.27,-2,-52.83),\ \text{Point 8}(12.24,-2,-33.63).
\end{aligned} \tag{8.11}$$

With its larger volume and the increased luminosity, MAPP-2 is expected to capture $\mathcal{O}(30)$ times the number of events than MAPP-1. We will estimate the sensitivities of both MAPP-1 and MAPP-2 in the following calculation.

CODEX-b In a large unoccupied space in the LHCb cavern after the upcoming Run 3 upgrade of LHCb, CODEX-b (the COmpact Detector for EXotics at LHCb) has been proposed to be built with a 3 m thick concrete radiation shield [306]. To estimate its sensitivity to displaced vertices, we follow the geometric selection cuts from Ref. [316]:

$$26\text{ m} < L_x < 36\text{ m},\ -3\text{ m} < L_y < 7\text{ m},\ 5\text{ m} < L_z < 15\text{ m}. \tag{8.12}$$

Additionally, Refs. [306, 316] require the track energy to be above 600 MeV. We neglect this requirement, as it makes no difference for the relatively large masses

Region	Inner Radius	Outer Radius	z-Extent	$\lvert d_0\rvert/\sigma_d^t$	σ_d^t
LHC Region 1	10	50	140	12	0.02
LHC Region 2	50	500	800	4	2
ILC Region 1	22	120	152	12	0.002
ILC Region 2	120	330	300	4	2
CEPC Region 1	15	180	240	12	0.007
CEPC Region 2	180	440	400	4	2

Table 8.1: Parameters of simplified detector geometries representing current and future detectors, including LHC [164], ILC [307,308], CEPC [226,309]. All length units are in cm.

in our simulation. We estimate the CODEX-b sensitivity at the HL-LHC with 300 fb^{-1} luminosity.

Lepton Colliders We additionally estimate the sensitivity at the future lepton colliders including International Linear Collider (ILC) and Circular Electro Positron Collider (CEPC) for the Higgs channel only. Lepton colliders are generally considered to be cleaner, for Higgs production in particular. We consider the lepton colliders with a center-of-mass energy of $\sqrt{s} = 250$ GeV and a luminosity of 5000 fb^{-1}. Higgs-Strahlung is the dominant Higgs production process at an electron-positron collider at 250 GeV, i.e., $e^+e^- \to Z^* \to Zh_1$. In the SM, this cross section is expected to be around 240 fb for $\sqrt{s} = 250$ GeV [226]. Due to the Higgs mixing angle, an additional reduction of the cross-section to $\cos^2\alpha = 0.91$ occurs in our case.

For the kinematic cuts, we use softer p_T cuts on the two muons in the final states and other cuts similar to CMS (Eqn. (8.5)) [90],

$$p_T(l) > 10\,\mathrm{GeV},\ |\eta| < 2.0,\ \Delta R > 0.2,\ \cos\theta_{\mu\mu} > -0.75, \tag{8.13}$$

for both colliders. For general purpose detection and precision measurements, a Silicon Detector (SiD) [307,308] is proposed to be used at ILC. In Table 8.1, we list the geometry of the detectors of ILC and CEPC [226,307–309] as well as the LHC from Eqns. (8.6) and (8.7) for comparison, as it is used for later geometric selection. Similar to the LHC, we refer to the silicon tracker as Region 1, and the components before the muon system as Region 2 for the lepton colliders. Therefore, we apply the geometric selection criteria associated with displaced vertices as in LHC analysis.

From the above discussions, the detectors can be classified in two categories according to their angle to the beam line. CMS and MATHUSLA are placed away from the beam line, whereas LHCb, FASER, MAPP and CODEX-b are situated in a more forward direction. Due to the kinematics, particles which are largely boosted are more likely to decay near the forward direction while the less boosted particles are more likely to decay away from the beam line. For our consideration of the two production processes of the heavy neutrinos either from the SM-like Higgs or Z' decays, as we focus on a light Z' with its mass smaller than 100 GeV and so as to the SM-like Higgs, the heavy neutrinos from the SM-like Higgs are considered to be less boosted. Thus we only simulate the processes $pp \to h_1 \to NN$ at CMS and MATHUSLA. Additionally, for the lepton colliders, as they can run at the Higgs pole with $\sqrt{s} = 250$ GeV, we only consider the Higgs channel for them.

8.3 Analytic estimation of the displaced vertex event rate

Apart from calculating the displaced vertex event rate using a full Monte Carlo simulation of the exponential decay of a heavy neutrino (including its process-specific boost), a quick estimation of the rate can be also obtained via analytical calculation based on the exponential decay. In the following discussion, we will show an example of the analytical estimation for the displaced event rate from SM-like Higgs decays at CMS. The overall results approximately match those from the full Monte Carlo simulation. While calculating the event rate from the exponential decay using integration can be formidable for complex detector volumes, this method can be regarded as a good approach to quickly estimate the overall displaced event rate assuming the shape of the detector volume is approximately regular.

The rate of displaced vertex events can be calculated analytically using integration based on the probability density of the exponential decay. We simplify the shape as an ideal ring-like cylinder. In the following, we estimate the number of such displaced events and thus the sensitivity of the 13 TeV LHC in probing the active-sterile mixing $V_{\mu N}$.

We take into account the probability of the heavy neutrino decaying inside the detector taking the shape as an ideal ring-like cylinder and estimate the event rate corresponding to observed displaced vertex events,

$$\frac{N_{\text{events}}}{\mathscr{L}} = \sigma(pp \to h_1 \to NN) \times \text{Br}(N \to \text{final state}) \times P(x_1 < x_N < x_2). \quad (8.14)$$

Here, $P(x_1 < x_N < x_2)$ is the probability of the heavy neutrino decaying between distances x_1 and x_2, which is approximately the probability of the heavy neutrino decay inside a LHC detector, such as the CMS and ATLAS. Taking into account the production mechanism,

$$P(x_1 < x_N < x_2) = \frac{1}{N} \int_0^{\pi} d\phi_N \int_0^1 d\beta_h \, p(x_1 < x_N < x_2) f(\beta_h) g(\phi_N), \quad (8.15)$$

where $\frac{1}{N}$ is the normalised factor, $p(x_1 < x_N < x_2)$ represents the probability density of an individual neutrino to decay within the given range, $p(x_1 < x_N < x_2) = e^{-x_1/L'_N} - e^{-x_2/L'_N}$ (the primed decay length are in center-of-mass frame, not in the rest frame of the neutrino). $f(\beta_h)$ is the probability density function for the velocity of the SM-like Higgs h_1 at the LHC, this function is obtained via calculating the kinematic of the Higgs produced at 13 TeV LHC based on the Mathematica package for Martin-Stirling-Thorne-Watt Parton Distribution Functions (MSTW PDFs) [317]. $g(\phi_N)$ represents the probability density function for the production angle ϕ between the SM-like Higgs (i.e. the beam pipe) and the RH neutrino in the center-of-mass frame.

We show the result of this analytic estimate of the rate of neutrinos that decay to a one muon final state within 1 cm and 1 m in Fig. 8.6, where we consider the displaced decay of one RH neutrino while we treat the second RH neutrino inclusively. Comparing the results in this section with the results from the Monte Carlo simulation for the CMS detector at the LHC described in Sec. 8.2 shown in Fig. 8.7, taking into account that $\frac{Br(N \to \mu^p m jj)}{Br(N \to \mu^p m \mu^+ \mu^- \nu)} \approx 10$ from Fig. 8.4, we find that both methods yield similar results if no kinematic acceptance is taken into account. The kine-

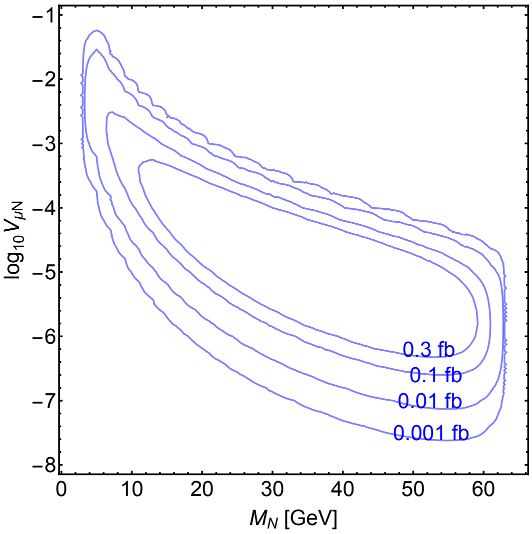

Figure 8.6: Displaced vertex event rate at the LHC $\frac{N_{\text{events}}}{\mathscr{L}}(pp \to h_1 \to NN \to N\mu^+\mu^-\nu)$ with one N decaying at a distance between 1 cm and 1 m, as a function of the neutrino mass and m_N and the mixing $V_{\mu N}$. The Higgs mixing angle is set at $\sin\alpha = 0.3$.

matic acceptance ε_{kin} in Fig. 8.7 is defined as $\sigma_{\text{after cuts}}/\sigma_{\text{total}}$, where $\sigma_{\text{after cuts}}$ is the cross section after implementing the cuts from Eqn. (8.5) which indicated at the Fig. 8.7 as the blue contours and σ_{total} is the original cross section before cuts. The kinematic efficiency ε_{kin} drops when m_N is either too small or too large closing the kinematic threshold, as the p_T contribution is small from the mass difference of N and μ for the former case, or from the Z' and N for the later case, where $p_T(\mu) > 26$ GeV cut becomes powerful.

8.4 Sensitivity reach

The sensitivity of the aforementioned detectors in the parameter space of the neutrino sector is estimated in the following discussion. For the Higgs decay channels, we generate the signal and implement the kinematic and geometric cuts for CMS at the 13 TeV LHC with 100 fb^{-1} luminosity, as well as CMS and MATHUSLA at the 13 TeV HL-LHC with 3000 fb^{-1} luminosity. Additionally, as lepton colliders are proposed as Higgs factories, we also estimate the sensitivity of the lepton colliders ILC [307, 308] and CEPC [226, 309] with 5000 fb^{-1} luminosity where the Higgs is produced via $e^+e^- \to Z^* \to Zh_1$ following a similar approach. For

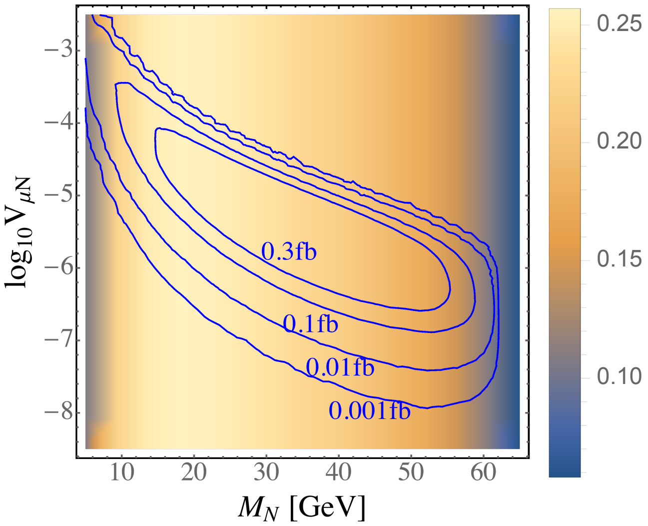

Figure 8.7: Effective LHC displaced vertex cross section $\sigma(pp \to h_1 \to NN \to N\mu^+\mu^-\nu)$ as a function of the RH neutrino mass M_N and the neutrino mixing. The background shading represents the kinematic efficiency $\varepsilon_{\rm kin}$ as indicated.

the Z' decay channels, we follow the same procedure but with CMS and MATHUSLA at the 14 TeV HL-LHC with 3000 fb^{-1} luminosity, and LHCb, MAPP-2 and CODEX-b at the 14 TeV HL-LHC with 300 fb^{-1} luminosity. Even though FASER 2 is in the forward direction, its operational luminosity is 3000 fb^{-1}. The estimated number of signal events is thus $N_{signal} \approx \sigma_{\rm signal} \times \varepsilon_{\rm kin} \times \varepsilon_{\rm geo} \times L$, where $\sigma_{\rm signal}$ is the cross section for the corresponding signal including specific final states. We require two muons at the CMS as well as the detectors at the lepton colliders, $pp \to h_1, Z' \to NN \to N\mu^+\mu^-\nu$, and single muon accompanied with jets at the LHCb, $pp \to h_1, Z' \to NN \to N\mu^\pm jj$. All visible final states $pp \to h_1, Z' \to NN$ (i.e. excluding $N \to \nu\nu\nu$) are accounted for all the other detectors without specified final states. L is the corresponding luminosity. $\varepsilon_{\rm kin}$ is the kinematic efficiency. The $\varepsilon_{\rm geo}$ is calculated by requiring a single N to decay within the corresponding geometry for the specified detectors.

To obtain the allowed parameter space, as the expected signal events are at most $\mathcal{O}(10)$, we follow a Poisson distribution for the number of signal events. The lower and upper limits on the mean value of signal events μ when observing n

events are given by [246]:

$$\mu_{\min} = \frac{1}{2}F^{-1}_{\chi^2}(\alpha, 2n), \quad \mu_{\max} = \frac{1}{2}F^{-1}_{\chi^2}(1-\alpha, 2(n+1)), \tag{8.16}$$

respectively. Here, $F_{\chi^2}(\alpha, n)$ is the cumulative distribution function for the χ^2 distribution with α being the significance level and n denoting the number of observed events. Probing a cross section with a sensitivity at 95% C.L., the upper bound on $\mu = \sigma \times L$ for $n = 0$ is 3.09 [246]. Therefore, we consider a model parameter point with $\mu > 3$ to be excluded at 95% C.L. on non-observation of any event.

With no observation of displaced events in existing searches, this assumption of no background is reasonable at CMS and LHCb [84–87]. For MATHUSLA, FASER 2, MAPP-2 and CODEX-b, as they are placed far away from the IP and thus detecting large displacement, this assumption is quite safe [302–306]. For lepton colliders, as they are regarded as much more cleaner than the hadron colliders, such assumption is reasonable as well [226, 307–309].

Nonetheless, we can take a pessimistic view to take into account the possible background for future high-sensitivity searches. This is realised by scaling the experimental upper limit on the background to the luminosity. Following a Poisson distribution for the non-observation of displaced vertex events [85, 87] at 20.5 fb^{-1}, we derived the upper limit on the average number of the background events to be 3 at 95% C.L.. We scale this rate up for the 100 fb^{-1} LHC and 3000 fb^{-1} HL-LHC, leading to 15 and 450 potential background events, respectively. For LHCb, we interpret the non-observation result of the existing displaced vertex events at 2 fb^{-1} [301] to obtain an upper limit on the average rate of 3 events at 95% C.L. [246]. Scale it to 300 fb^{-1} HL-LHC, we get 450 events of background again for LHCb by coincidence. Despite of that, we still take no background for lepton colliders, MATHUSLA, MAPP-2 as well as CODEX-b. Thus, a parameter point is excluded on no observation if $\chi^2 = (N_{\text{tot}} - N_B)^2/N_B > 3.84$ at 95% C.L., where N_{total} is the total number of events and N_B is the number of events for background.

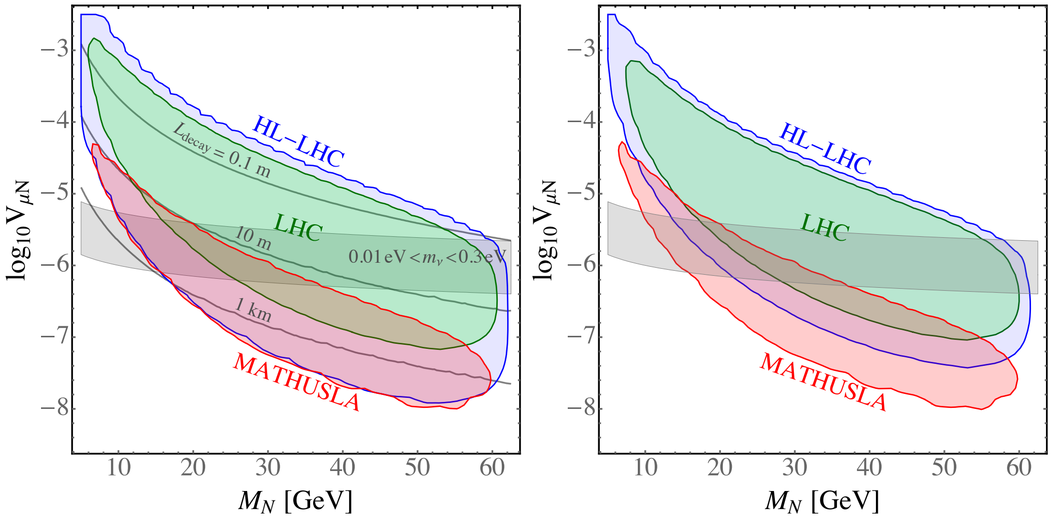

Figure 8.8: Excluded regions in the $(m_N, V_{\mu N})$ parameter space at 95% C.L. assuming no observation of a single displaced vertex for the 100 fb^{-1} LHC (green), the 3000 fb^{-1} HL-LHC (blue) and the MATHUSLA option at HL-LHC (red). The left plot is in the optimistic view assuming no background after selection criteria whereas the right plot is in the pessimistic view where the upper limit on the background rate from the non-observation at 20.5 fb^{-1} is scaled to the different luminosities. The grey band indicates the parameter region where a light neutrino mass in the interesting range is generated, $0.01\text{ eV} < m_\nu = V_{\mu N}^2 m_N < 0.3\text{ eV}$. The grey curves indicate proper decay lengths of the heavy neutrino.

8.4.1 Higgs decays channel

Following the approach discussed above, the results of sensitivities for the SM-like Higgs decays channel $pp \to h_1 \to NN$ at the CMS detector at the 13 TeV LHC and HL-LHC, as well as the MATHUSLA at the HL-LHC are shown at the Fig. 8.8. The left plot illustrate the sensitivities for the optimistic view assuming no background, and the right plot for the pessimistic view with a scaling of the background. In this figure, we only require a single displaced vertex from one of the heavy neutrinos. Assuming no appreciable background, a sensitivity down to $V_{\mu N} \approx 10^{-7}$ for $m_N \approx 55$ GeV is obtained at the 13 TeV LHC with 100 fb^{-1} luminosity. The CMS detector at the HL-LHC can probe even smaller active-sterile neutrino mixing as low as $V_{\mu N} \approx 10^{-8}$ at $m_N \approx 55$ GeV. For MATHUSLA, even though it should be potentially sensitive to even smaller neutrino mixing, it is however cancelled out by its small angular coverage thus similar lower limits to CMS at HL-LHC are obtained. These sensitivities are however conditional to the Higgs mixing $\sin\alpha = 0.3$ we considered.

If future lepton colliders obtained improved limits on the Higgs mixing such as $\sin\alpha \approx 0.06$ [227], the expected number of signal events would be 30 times smaller. The horizontal grey band is the preferred parameter region for a pure Type-I seesaw where $m_\nu = V_{lN}^2 m_N$ with 10^{-2} eV $< m_\nu <$ 0.3 eV as indicated by oscillation and absolute neutrino mass measurements.

In Fig. 8.9 (left) for the lepton colliders, due to their low production cross section, but with higher luminosity than the LHC, the ILC/CEPC still have a similar sensitivity to the LHC as low as $V_{\mu N} \approx 10^{-7}$ for heavy neutrinos with $m_N \approx 55$ GeV. For CEPC, because of its longer and larger detector, the effective event rate is slightly larger. Even though the lepton colliders are considered to be cleaner, this advantage is not realised in the optimistic view as we assume no background for LHC as well.

Taking the pessimistic view in Fig. 8.8 (right), we can still obtain stringent limits on the neutrino mixing as low as $10^{-7.5}$ at the HL-LHC with 450 projected background events. While for CMS at the 100 fb^{-1} LHC, the sensitivity is very similar to the optimistic view as only 15 background events are assumed. Note that we are actually taking an overly pessimistic view as we take the background to be constant at its upper limit for any m_N, since we would get smaller background because the heavy neutrino becomes longer-lived and most SM background should have decayed away already. In both the left and right panel, the sensitivity for MATHUSLA are identical as we assume no background for both panels.

Two displaced vertices Alternatively, we can demand observing two different displaced vertices as our signal. For events requiring muons in the final state, the signatures can contain 2, 3 or 4 muons, i.e. $pp \to h_1 \to NN \to \mu^\pm jj, \mu^\pm jj$ which is the dominant channel, $pp \to h_1 \to NN \to \mu^\pm jj, \mu^-\mu^+\nu_\mu$ and $pp \to h_1 \to NN \to \mu^-\mu^+\nu_\mu, \mu^-\mu^+\nu_\mu$. The effective event rate is further reduced by more than an order of magnitude due to the requirement of two displaced vertices. However this signature can be regarded as more distinct for the discovery of this specific model. As two displaced vertices are rather rare, we only take the optimistic view, therefore no background is taken into account. However, there are background from the LHC

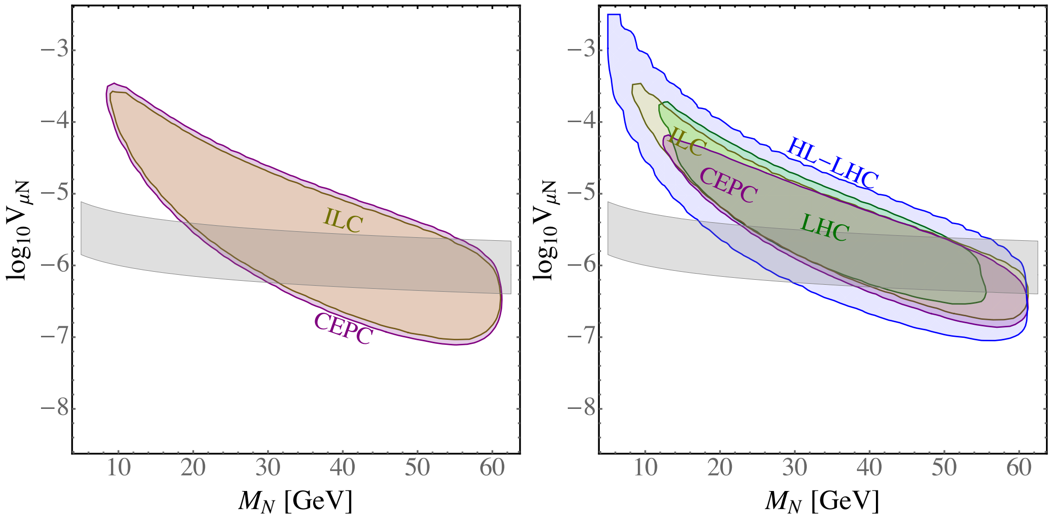

Figure 8.9: Left: Excluded regions in the $(M_N, V_{\mu N})$ parameter space at 95% C.L. assuming no observation of a *single displaced vertex* for the 5000 fb^{-1} ILC (red) and CEPC (blue). The grey band indicates the parameter region where a light neutrino mass in the interesting range is generated, 0.01 eV $< m_\nu = V_{\mu N}^2 m_N <$ 0.3 eV. Right: Excluded regions in the $(M_N, V_{\mu N})$ parameter space at 95% C.L. assuming no observation of *two displaced vertices* for the 100 fb^{-1} LHC (green), 5000 fb^{-1} ILC (red) and CEPC (purple) and 3000 fb^{-1} HL-LHC (light blue).

material interactions, and we are again taking an optimistic view.

In Fig. 8.9 (right), the sensitivity for LHC, HL-LHC, ILC and CEPC is shown assuming no-observation of two separate displaced vertices from the decays of the two heavy neutrinos. Due to the low effective event rate, the excluded parameter space is smaller for all colliders. In this figure, ILC/CEPC excludes larger region to the LHC, as their higher geometric efficiencies win out the low production cross section for two displaced vertices. The HL-LHC still probes the largest parameter space. All of these detectors can reach the Type-I seesaw regime.

As an event with two simultaneous displaced vertices is regarded as a striking signature for this specific model, it may serve as conclusive observational signal for discovery. Once these events are observed, we can narrow down the possible model parameters as well. In Fig. 8.10 (left), the viable parameter space for LHC and ILC if two events with two displaced vertices signature are observed is shown. According to the Poisson distribution, this would require the mean value of signal events μ to be $0.36 < \mu < 6.72$ [132] ($0.05 < \mu < 5.14$ for observing one event).

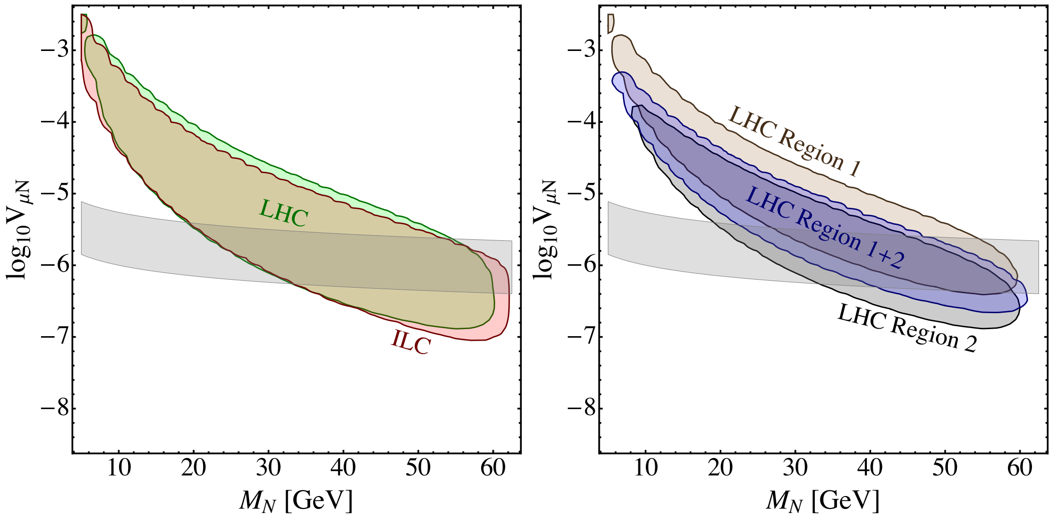

Figure 8.10: Left: Viable parameter space assuming the observation of two events each containing two displaced vertices, at the LHC and the ILC. Right: Viable parameter space assuming the observation of two events in the different regions of the simplified LHC detector, each containing two displaced vertices where: (i) both events are fully in Region 1, (ii) both events are fully in Region 2 or (iii) one event is fully in Region 1 and the other fully in Region 2. In both plots, the Higgs mixing $\sin\alpha$ is not fixed but can vary up to its maximally allowed value, i.e. $\sin\alpha \lessapprox 0.3$.

For a fixed Higgs mixing as we chose elsewhere in the thesis, the possible parameter space should look like a ring for a given number of event with two displaced vertices as the proper decay length should not be too large or small. Instead, we allow the Higgs mixing to vary up to its experimental limit, i.e. $\sin\alpha \lessapprox 0.3$, but the number of the observed displaced vertices events is still fixed. Therefore, we get a band-like shape again. We can narrow down the possible parameter space further if the heavy neutrino mass was measured. Finally, if enough events with two displaced vertices were observed so that the decay length of heavy neutrino can be extracted from the exponential decay profile, we can limit the parameter space even further. An example is shown in Fig. 8.10 (right), with the regions of the CMS detector where we detect the signal events is shown. In the simplified CMS detector, if two signal events each with two displaced vertices are observed where: (i) both events are fully in Region 1, (ii) both events are fully in Region 2 or (iii) one event is fully in Region 1 and the other fully in Region 2. As expected, Region 2 being further away from the IP, is sensitive to smaller $V_{\mu N}$ compared to Region 1. In addition to the purely Region 1 and Region 2, LHC Region 1+2 represents events with the two displaced vertices in different regions.

Summarising the discussions above, with the assumption of large Higgs mixing, the LHC can probe the active-sterile mixing as low as $V_{\mu N} \approx 10^{-7}$, while the future high luminosity run and the proposed MATHUSLA detector can reach $V_{\mu N} \approx 10^{-8}$. Lepton collider, do not benefit from its cleaner background for this distinct signature while the low production cross section of the Higgs makes them only competitive to the current run of LHC. All detectors can reach the preferred region where the light neutrino masses can be generated for $m_N \approx 20-60$ GeV. However, these sensitivities will be reduced if future constraints on the exotic Higgs mixing became more severe.

8.4.2 Z' decay channel

For the Z' decays channel, we consider a light Z' with mass $10-100$ GeV to get appreciable cross section and avoid non-perturbative effects, the heavy neutrino and its decay products are more likely to be boosted and thus travel in more forward directions. Thus, we calculate the sensitivity following the same procedure as above also for forward detectors including LHCb, FASER, MAPP-1, MAPP-2 and CODEX-b in addition to CMS and MATHUSLA. As mentioned in Sec. 8.1, we take $g_{B-L} = 10^{-3}$ and $\frac{m_N}{m_{Z'}} = 0.3$ to increase the event rate.

For the optimistic view with no background assumption, the sensitivity for non observation is shown in the left panel of Fig. 8.11. Of the parameter space under consideration, FASER 2 is only able to probe the largest active-sterile neutrino mixing at low m_N while CODEX-b and MAPP-2 are able to probe lower mixing, and MATHUSLA is sensitive to the smallest neutrino mixing $V_{\mu N} \lesssim 10^{-6}$, reaching the region prefered for the Type-I seesaw mechanism as indicated by the horizontal band where 10^{-2} eV $< m_\nu = V_{\mu N}^2 m_N < 0.3$ eV. For higher masses, LHCb is sensitive for $m_N \gtrapprox 10$ GeV, whereas $m_N \gtrapprox 25$ GeV for CMS at HL-LHC. This is because the $p_T(\mu) > 12$ GeV (see Eqn. (8.8)) and $p_T(\mu) > 26$ GeV (see Eqn. (8.5)) requirements for the corresponding experiments give lower bounds for the mass of the heavy neutrino. For the Higgs decays channel, this is however automatically

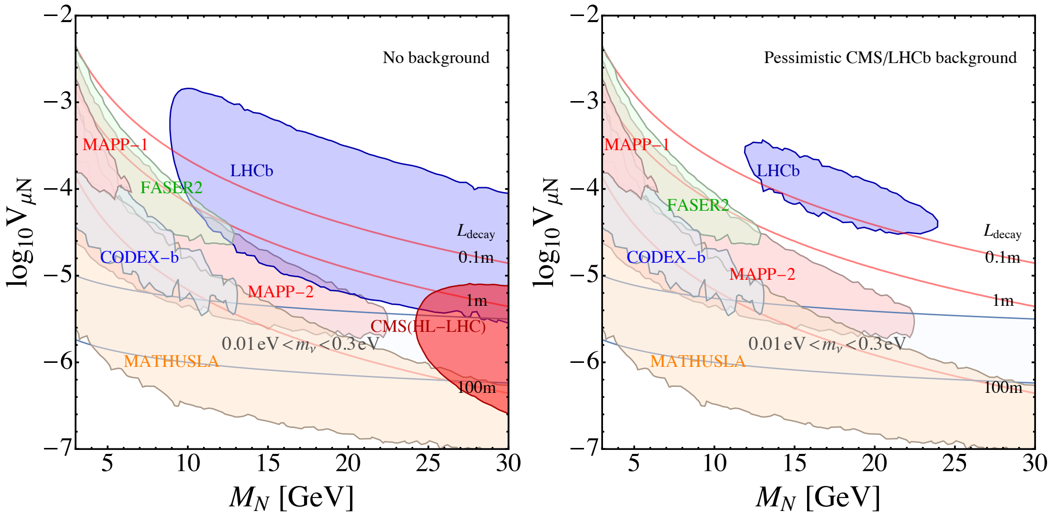

Figure 8.11: Projected sensitivity of displaced vertex detectors in the heavy neutrino mass m_N and neutrino mixing $V_{\mu N}$ parameter plane. The $U(1)_{B-L}$ gauge coupling and the Z' mass are chosen as $g_{B-L} = 10^{-3}$ and $m_{Z'} = 3.33 \times m_N$, respectively. The displaced vertex detectors are CMS (HL-LHC), LHCb, MATHUSLA, FASER 2, MAPP-1, MAPP-2 and CODEX-b as indicated, at 14 TeV and using projected future luminosity as detailed on the text. In the left plot, we assume no background to displaced vertex searches whereas in the right plot, we scale current background limits for CMS and LHCb to the luminosity used. The red curves denote the proper decay length of the heavy neutrino N and the horizontal band indicates the preferred parameter region where the light neutrinos acquire a mass between 10^{-2} eV $< m_\nu = V_{\mu N}^2 m_N < 0.3$ eV in a canonical seesaw mechanism.

satisfied as the SM-like Higgs is quite heavy. Complementary to the other detectors, LHCb and CMS probe larger $V_{\mu N}$. On the other hand, with smaller volume and luminosity, the MAPP-1 detector can only probe a very small region in the top left corner for 3 GeV $< m_N \lessapprox 7$ GeV and $10^{-4} \lessapprox V_{\mu N} \lessapprox 10^{-3}$, while MAPP-2 is sensitive up to $m_N \approx 22$ GeV and it fills the gap between the sensitivity of LHCb and MATHUSLA.

We can also take a pessimistic view and scale the upper limit on the background (mainly from $b-$ quarks, mesons and detector interactions) from the non-observation in current searches. For LHCb, using a Poisson distribution, we interpret the non-observation displaced vertex searches at 2 fb^{-1} [301] to obtain an upper limit on the average rate of 3 events at 95% C.L. [246]. Besides in Sec. 8.4.1, we have already estimated that the number of background events at 3000 fb^{-1} HL-LHC is 450. Therefore, we set as exclusion if $\chi^2 = (N_{tot} - N_B)^2/N_B > 3.84$ at

95% C.L. [246]. The result of this pessimistic view is shown in Fig. 8.11 (right). A much smaller excluded region is obtained for LHCb compared to the optimistic view, while CMS is no longer sensitive within the region of consideration. This can be understood, as the expected number of signal events passing the high p_T cuts for such light heavy neutrinos is too low to be distinguishable from the expected 450 background events.

Different detectors are sensitive to different regions due to several reasons. First, the luminosity for CMS, MATHUSLA and FASER 2 is 10 times larger than the luminosity for LHCb, MAPP-2 and CODEX-b. Second, the detectors have different volumes and are therefore sensitive to different decay lengths of the heavy neutrino, and they have different detector geometric efficiencies ε_{geo}. Among them, even though FASER 2 is placed furthest from the IP, due to its small radius in the transverse direction around the beam line, its geometric efficiency is tiny and it is only accepting highly boosted particles, it is thus only sensitive to heavy neutrinos with meters of proper decay length, i.e. large $V_{\mu N}$ for small m_N. The volume of MAPP-2 is somewhat larger compared to CODEX-b, thus sensitive to larger m_N and $V_{\mu N}$. The MATHUSLA detector is able to probe the lowest mixing angles as small as 10^{-6} for the whole parameter space of the heavy neutrino mass we consider. LHCb and CMS by design are only sensitive to at most meters of displacement, however LHCb is only sensitive to larger neutrino mixing while CMS can still probe a region where the proper decay length of the heavy neutrino can be 100 meters because of its large volume, i.e. large angular coverage, so that it can still probe the tail of the exponential decay distribution.

The complementarity of different experiments to probe heavy neutrinos with different decay length is further illustrated in Fig. 8.12 for FASER 2 and CODEX-b as an example using 10^6 events. We choose m_N equal to 5 GeV at the left panel and 15 GeV in the right panel and $V_{\mu N} = 10^{-4.5}$ for both panels. Accordingly, the Z' mass is fixed at 17 and 50 GeV, respectively. For the events passing the angular acceptance for the geometry of CODEX-b and FASER detectors, we plot the corresponding decay length distributions in lab frame. As for the latter case,

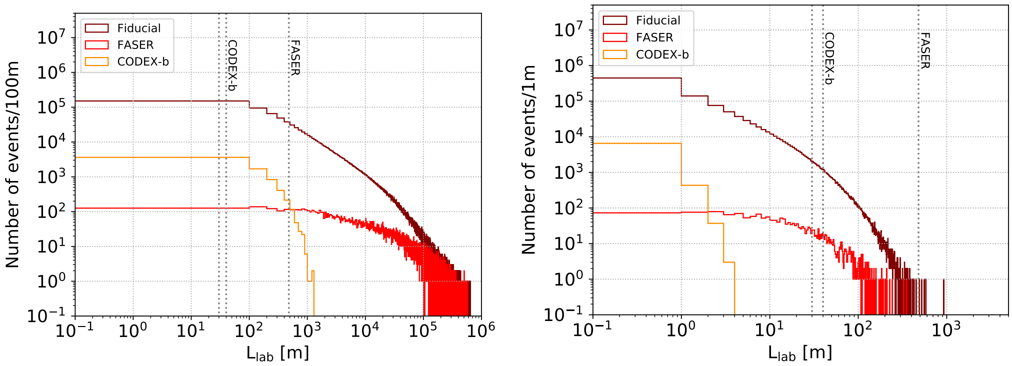

Figure 8.12: Distribution of the heavy neutrino decay length in the lab frame for $m_N = 5$ GeV, $m_{Z'} = 17$ GeV (left) and $m_N = 15$ GeV, $m_{Z'} = 50$ GeV (right). The active-sterile neutrino mixing is set at $V_{\mu N} = 10^{-4.5}$. The three histograms represent the distributions of all events (fiducial) as well as those passing the angular acceptance criteria of FASER and CODEX-b. The vertical lines show the approximate distance from the interaction point at which FASER and CODEX-b are located. For CODEX-b, the two lines shown represents the depth of detector.

the mass difference between the heavy neutrino and Z' is larger and the neutrinos are more boosted. However, the proper decay length becomes smaller with higher m_N, so the overall lab frame decay length is still more than 100 times smaller in the right plot compared to the left plot. It is evident to see that FASER only selects the most highly boosted events so that their decay length is much larger. This is going to be justified in the next paragraph by showing their momentum and angular distribution. Finally, the distance to the IP of the detectors is shown as vertical lines. Therefore, it is obvious to see that both FASER and CODEX-b are able to probe a heavy neutrino with 5 GeV mass. However for 15 GeV, neither CODEX-b nor FASER are sensitive to the chosen neutrino mixing. For this mass, FASER can be sensitive if a smaller mixing angle is chosen as shown in Figure 8.11.

Different detectors select different parts of the distribution in the momentum and angle of the neutrino. This is illustrated in Fig. 8.13. We show the two dimensional distribution for the total spatial momentum P of the neutrino and the angle θ between the beam line and the momentum of the neutrino for a fixed small neutrino mass $m_N = 3$ GeV but two different Z' masses, $m_{Z'} = 10$ GeV (left column) and $m_{Z'} = 50$ GeV (right column). Besides, we show the distribution at the parton level in the

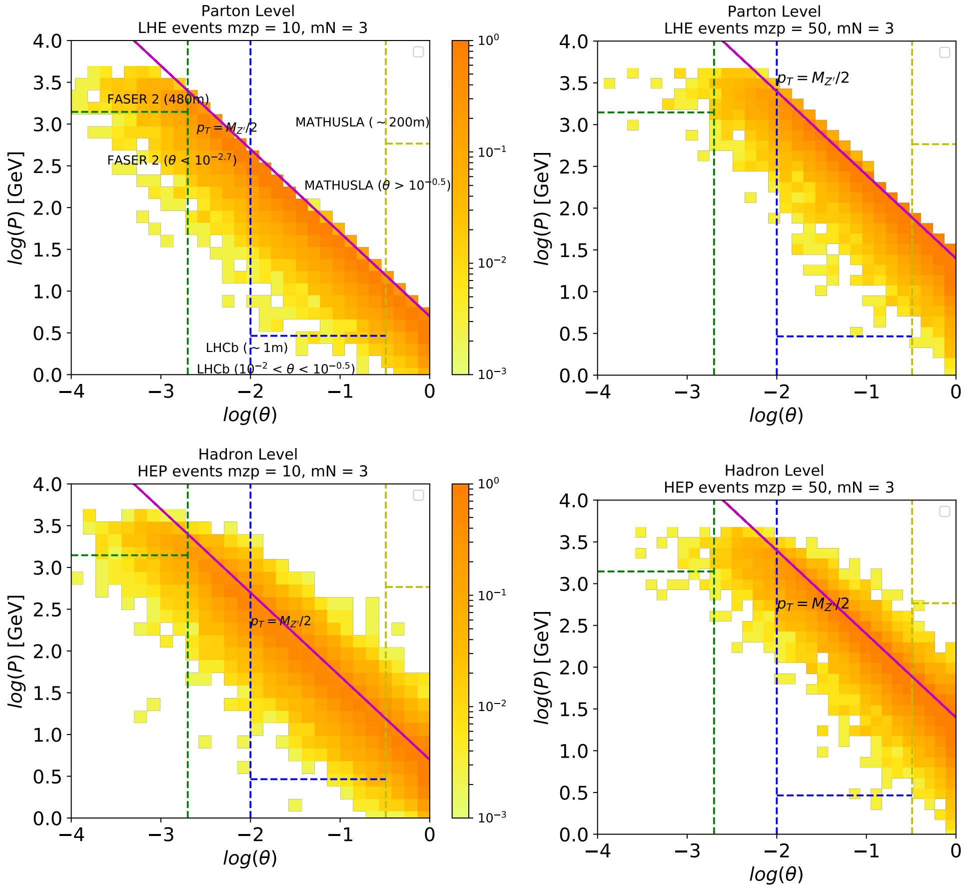

Figure 8.13: Left: The distribution of the momentum and its angle between the beam line θ of the heavy neutrino N, with $m_N = 3$ GeV and $m_{Z'} = 10$ GeV. Right: Same but $m_{Z'} = 50$ GeV. Up: The distribution at parton level. Bottom: The distribution at hadronization/shower level. The solid purple line corresponds to $p_T = p\sin\theta = m_{Z'}/2$. The horizontal lines indicate the decay length in lab frame when V_{lN} is fixed at 10^{-3} for FASER 2 (480m), LHCb ($\sim$1m) and MATHUSLA ($\sim$ 200m) which are taken as representative examples, while the vertical lines show θ range for FASER 2 ($\theta < 10^{-2.7}$), LHCb ($10^{-2.0} < \theta < 10^{-0.5}$) and MATHUSLA ($\theta < 10^{-0.5}$).

top row and the hadronization level in the bottom row. The distribution becomes more even around the line $p_T = m_{Z'}/2$ due to the p_T change from the presence of initial/final state radiation. The dashed horizontal lines indicate the momentum corresponding to the lab frame decay length of 480 m, 1 m, 200 m which is the corresponding distance to the IP for FASER 2, LHCb and MATHUSLA for a neutrino with fixed mass and mixing angle of $V_{\mu N} = 10^{-3}$. This shows the different displacements of the heavy neutrino to which the detectors are sensitive. Likewise, the vertical lines indicate the different angular acceptance of the detectors, $\theta < 10^{-2.7}$

for FASER 2, $10^{-2.0} < \theta < 10^{-0.5}$ for LHCb and $\theta < 10^{-0.5}$ for MATHUSLA. Consequently, FASER 2 only selects the distribution of heavy neutrinos which are highly boosted. Thus, even though it is furthest away from the IP, the proper decay length to which it is sensitive is still smaller than that of other detectors. Besides, comparing the left and right columns, larger difference between the masses of Z' and N also leads to larger average momentum and larger θ, thus larger p_T.

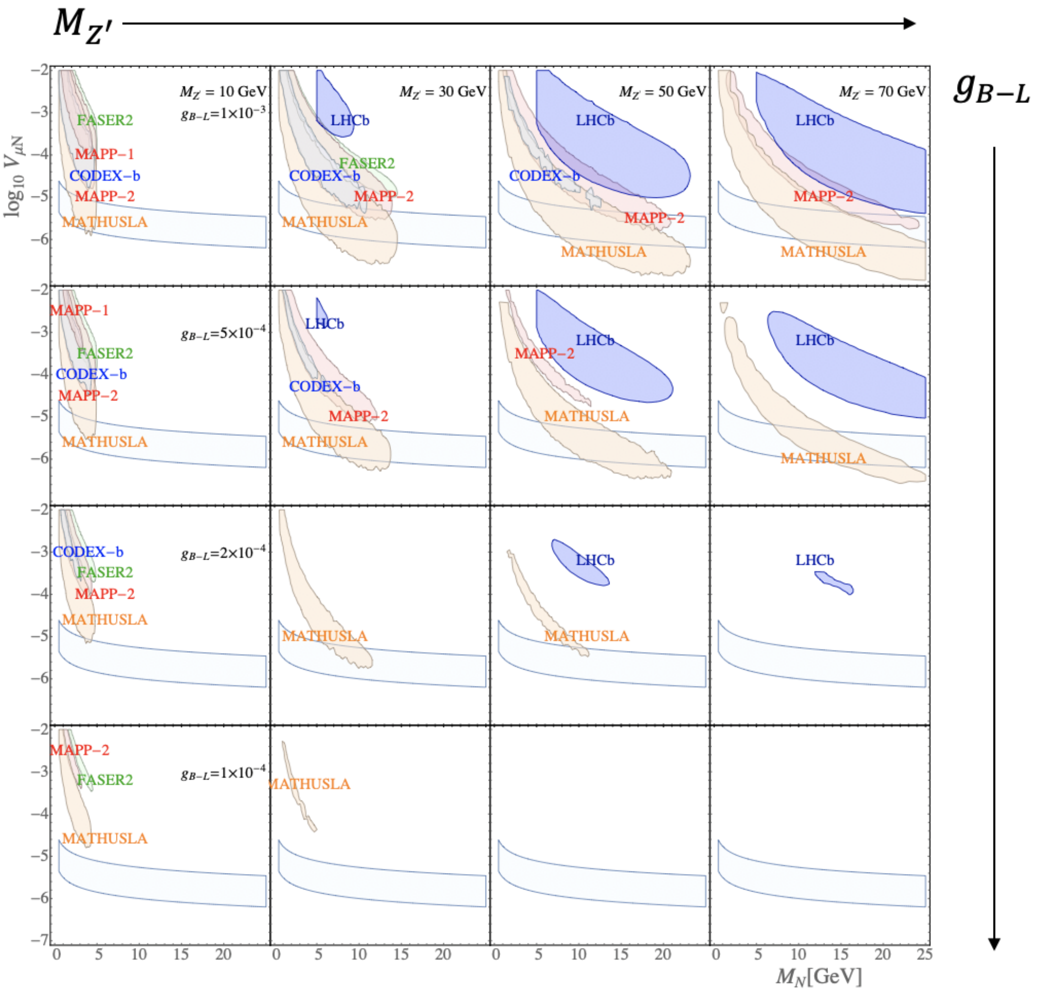

Figure 8.14: Projected sensitivity of lifetime frontier detectors in the heavy neutrino mass m_N and neutrino mixing $V_{\mu N}$ parameter plane as in Fig. 8.11 (left) but for a series of fixed values of $m_{Z'}$ and g_{B-L} as indicated. The background is assumed to be zero for all detectors.

Instead of fixing the mass ratio $\frac{m_N}{m_{Z'}} = 0.3$ as assumed previously, we now allow it to vary. The result is shown in Fig. 8.14. The mass of Z' is fixed at 10 GeV, 30 GeV, 50 GeV and 70 GeV in the first, second, third and fourth column, respectively.

Analogously, from the top to bottom row, g_{B-L} runs from 10^{-3} to 10^{-4}. We thus explore the dependence of the sensitivities on $m_{Z'}$ and g_{B-L} in this figure. We take the optimistic view and assume no background. Due to the $m_{Z'}$, the sensitivities have different ranges in the first to fourth column because of the kinematical threshold for Z' to decay into two heavy neutrinos. Moreover, LHCb fails to show any sensitivity for $m_{Z'} < 30$ GeV due to the $p_T(\mu) > 12$ GeV cut, while it can still probe $V_{\mu N}$ as low as 10^{-5} for higher $m_{Z'}$ and larger g_{B-L}. Besides, it is only sensitive to m_N larger than 4.5 GeV due to the selection cuts mentioned in Sec. 8.2 requiring the invariant mass of the decay products μjj to be over 4.5 GeV. This is shown by the vertical cut-off to the left of the LHCb region. Similarly, we fail to get any sensitivity for all cases for CMS because of the even stronger cut, $p_T(\mu) > 26$ GeV. This is consistent with the sensitivity at $m_N \gtrapprox 25$ GeV thus $m_{Z'} \gtrapprox 83$ GeV in Fig. 8.11 which uses the fixed ratio $\frac{m_N}{m_{Z'}} = 0.3$. We find that the sensitivity for LHCb is better than CMS. This is partly due to the fact that as we take different selection criteria for LHCb and CMS and the $\mu\mu j$ final state required by LHCb has a larger branching ratio compared to the $\mu\mu\nu$ final state for CMS due to hadronic decays of the W; The criteria for LHCb require a softer p_T cut so that the signal cross section for LHCb is much larger than for CMS. The reduction in the luminosity cannot balance the gain in the increase in cross section. Besides, due to its small volume and operational luminosity, MAPP-1 is only sensitive for $m_{Z'} = 10$ GeV and $g_{B-L} > 5 \times 10^{-4}$. FASER 2 can only probe $m_{Z'} \leq 30$ GeV as its geometric efficiency is small.

In summary, with the assumption that they can capture any particle decaying within the detector volume, the proposed detectors at the lifetime frontier MATHUSLA, FASER 2, MAPP-1, MAPP-2 and CODEX-b are able to probe small values of m_N and $V_{\mu N}$. Among them, MAPP-1 will be installed for Run 3 of the LHC. Even though the displacement from the IP of FASER detector is largest, it only selects particles very close to the beam direction. This requires a significant boost which cancels its advantage, making it not as comparable to other detectors to probe long-lived particles including heavy neutrinos. On the other hand, CMS as well as LHCb are only able to probe larger m_N due to the harder selection requirements.

Chapter 9

Conclusions and Future Outlook

The observation of neutrino oscillations and the resulting presence of finite neutrino masses and lepton flavour mixing remain a mystery within the SM. While the discovery of the Higgs, and the measurement of many of its properties, has now well established the mechanism of charged fermion mass generation within the SM, the same cannot be said for neutrinos. Their lightness and the absence of a right-handed state evade our understanding and are one of the most tantalizing indications for physics beyond the SM. Among the most suggestive extensions of the SM in this direction involves the addition of right-handed neutrinos. Being necessarily completely uncharged under the SM forces (i.e. they are sterile), this opens up the possibility of them acquiring a so called Majorana mass. This results in the well known seesaw mechanism (of the first type) [19–21] which provides an elegant explanation for the lightness of the active neutrinos and may even be responsible for the presence of matter in the universe through Leptogenesis [318].

While the seesaw mechanism with heavy sterile neutrinos is very convincing, it suffers from two main problems: (i) The heavy neutrinos are generically expected to be very heavy, $m_N \sim 10^{14}$ GeV, to naturally explain the light neutrino masses, $m_\nu \sim v^2/m_N$, with the electroweak scale $v \approx 100$ GeV. This makes the seesaw mechanism very hard to test. (ii) The presence of Majorana masses for the sterile neutrinos is ad hoc, i.e. they are simply put in by hand. In a way, the problem of light neutrino masses is merely replaced by the problem of heavy neutrino masses. Instead in this thesis, we consider a gauge extension of the SM where the heavy neutrinos are charged under an exotic force, namely an abelian $U(1)_{B-L}$ associated with the baryon – lepton $(B-L)$ quantum number [22]. This results in one of the most minimal extensions of the SM where the heavy Majorana neutrino masses are generated through the spontaneous breaking of the $U(1)_{B-L}$ part of the group above the electroweak scale. This provides a dynamical embedding of the seesaw mechanism which has the phenomenological benefit that the heavy neutrinos are not completely sterile but couple through a heavy Z' vector boson and a SM-singlet scalar χ associated with $U(1)_{B-L}$. While this scenario does not really solve the first problem mentioned above (the $B-L$ breaking should occur at a very high scale $\sim 10^{14}$ GeV to reproduce heavy neutrino masses at this scale), we can consider scenarios where the $B-L$ breaking occurs close to the electroweak scale to produce possible signatures at the LHC. While the mixing V_{lN} between the active and sterile neutrinos will be generically small to maintain the lightness of neutrinos, $V_{lN} \sim \sqrt{m_\nu/m_N} \approx 10^{-6}$ for heavy neutrinos with electroweak scale masses, $m_N \sim 1-100$ GeV, the presence of the $U(1)_{B-L}$ gauge boson and scalar may allow to probe the heavy neutrinos in regimes otherwise inaccessible. In this thesis, we have explored some of the consequenes of the minimal $B-L$ gauge model with the aim to shed light on the mass generation of light neutrinos. Specifically, we have used three approaches in this direction, namely (i) the use of SM measurements and (ii) the analysis of prompt lepton signals at the LHC, as well as (iii) a study of displaced vertices to probe long-lived heavy neutrinos.

SM measurements at the LHC are made in fiducial regions of phase space for a given process. In the $B-L$ model, we have found they are sensitive to both the gauge sector with the Z' mass and the $B-L$ coupling strength g_{B-L}, as well as the scalar sector with the exotic Higgs mass m_{h_2} and the mixing strength $\sin\alpha$. Within the gauge sector, decoupling the exotic Higgs h_2, this method is able to show a competitive sensitivity for a large parameter space to existing studies [31]. Turning on the Higgs mixing, the `CONTUR` framework incorporating the LHC measurements yields a better sensitivity for low mass Z'. Focusing on the scalar sector, this method has proven useful giving sensitive limits in cases with a light Z' and small g_{B-L}

compared to direct exotic Higgs searches [78]. Although dedicated searches will obtain more stringent limits for a specific parameter space, SM measurements are still powerful to generally constrain a much larger parameter space and non-minimal scenarios containing multiple BSM contributions, as it makes use of the data from a large library of different LHC measurements. The studies presented here use only a relatively small fraction of LHC data currently available as fiducial, particle-level measurements in `HEPDATA` [319] and `Rivet` [280]. As more data is collected, and increasingly precise measurements are made available in this manner, the sensitivity will grow further.

The recasting of prompt lepton final state searches is able to probe the gauge sector. The exotic gauge boson Z' can be produced via s-channel Drell-Yan, decays of the SM-like Higgs or via the final state radiation of muons in SM Drell-Yan processes. Among them, the SM-like Higgs decay channel can yield upper limits $g_{B-L} \lessapprox 10^{-5} - 10^{-3}$ for 0.25 GeV $< m_{Z'} <$ 62.5 GeV for $\sin\alpha = 0.3$. This can be more than one magnitude better compared to existing limits [31].

Displaced vertex searches probe the neutrino sector including the mass of the heavy neutrino m_N and its active-sterile mixing $V_{\mu N}$ to the muon. Here, we have focused on coupling to muons and we have studied displaced vertex searches in the outer region of CMS, LHCb and proposed detectors at the lifetime frontier including MATHUSLA, FASER 2, MAPP-1, MAPP-2, and CODEX-b as well as detectors at the proposed future lepton colliders ILC and CEPC. Two channels of the production of long-lived heavy neutrinos are considered, namely the production through SM-like Higgs decays and exotic gauge boson Z' decays. The Higgs channel yields a very competitive sensitivity in the active-sterile mixing $V_{\mu N} \approx 10^{-6}$ for heavy neutrino masses between 20 GeV to 60 GeV at the LHC and lepton colliders. With higher luminosity at the LHC, or equipped with the MATHUSLA detector on the surface, we are able to reach a sensitivity improved by an order of magnitude. In the Z' channel, heavy neutrinos are more likely to decay in the forward direction, therefore detectors in the forward direction are considered. Fixing the heavy neutrino mass as $m_N/m_{Z'} = 0.3$ to make m_N at the order of electroweak scale and the phase space factor for $Z' \to N\ N$ appreciable, we have obtained a similar sensitivity in CMS, LHCb and proposed far detectors for 3 GeV $< m_N <$ 30 GeV. In general, proposed far detectors like MATHUSLA, FASER 2, MAPP-2 and CODEX-b probe smaller m_N and $V_{\mu N}$. This arises due to the absence of kinematic thresholds and a large distance from the IP. Among them, the MATHUSLA detector is able to give the most sensitive limits. FASER 2, although placed furthest, is not as sensitive as it is small and probes only highly boosted decays in the forward direction. In time for Run 3 of the LHC, MAPP-1 and FASER 1 are expected to be installed. Here, MAPP-1 should set initial limits for light $m_N \sim 5$ GeV via the process $pp \to Z' \to NN$.

A key conclusion of this thesis is that for $\sin\alpha = 0.3$ and $g_{B-L} = 10^{-3}$, the sensitivity on the active-sterile mixing $V_{\mu N}$ from heavy neutrino searches via displaced vertices can reach the seesaw region, i.e., $V_{\mu N} \approx 10^{-6}$ for $m_N \sim 1 - 100$ GeV. This is not possible for sterile neutrinos produced via the active-sterile mixing in SM W and Z decays. However, the limits on the Higgs mixing and the $B - L$ coupling are expected to be improved in the future. For example, the proposed lepton collider CEPC can potentially improve the limit on the Higgs mixing as $\sin\alpha \lessapprox 0.06$ [227] and LHC dilepton searches can continue improving the limit on g_{B-L} within the $m_{Z'}$ range of interest. With these updated limits, the cross section of the displaced vertex signal from heavy neutrino decays might not be sufficient to be probed at the LHC.

The LHC continues to collect more data and there is ample opportunity for future work. Additional searches such as mono-jets [320], which are mainly used to probe dark matter, can probe heavy neutrinos as well if they escape detection. Other experiments at the life-time frontier have been proposed such as SHiP [258]. SHiP would be a general-purpose experiment to be installed in a beam dump facility at the CERN Super Proton Synchrotron (SPS) to search for hidden particles including heavy neutrinos. It has a 400 GeV beam which can produce a large number of charm mesons and photons. Together with the high intensity of the SPS, it is expected to be very sensitive in probing heavy neutrinos. It has a detector located about 100 metres away from its IP, thus it is potentially sensitive to displaced vertex signatures from ultra long-lived heavy neutrinos with masses $m_N \lesssim$ few GeV.

In the meantime, experiments such as the Belle-II, can also probe the $B-L$ model. Belle-II is a detector for SuperKEKB, a Super B factory level upgrade of the KEKB collider [321, 322]. It has a very high luminosity, thus it can be sensitive to Z' produced from the meson decays with a narrow mass range $m_{Z'} \lesssim 5$ GeV [322]. The sensitivity on the $B-L$ coupling g_{B-L} is expected to be strongly improved within this range [322]. It may also be sensitive to displaced vertex signatures of the heavy neutrino produced from Z'. However, as the heavy neutrino in this case is light and thus long-lived, it is not expected to be captured in the Belle-II detector.

In the theory side, the hierarchy problem for the SM is not explained by the $B-L$ model alone. If low scale Supersymmetric (SUSY) is introduced, the huge loop corrections to the Higgs mass can be cancelled out by the SUSY partners. Therefore, we can fix the hierarchy problem by the Fine-tunning of the scale $m^2_{h_{\rm SM}}/\Lambda^2_{SUSY}$. The result $B-L$ SUSY SM can potentially explain the dark matter problem, as it contains SUSY partners as dark matter candidates [323–327].

In summary, in this thesis we have aimed to assess the potential of the LHC, its future upgrades and some of the proposed future colliders to be probe the nature of neutrino mass generation in one of the most suggestive scenarios. Namely, the minimal $B-L$ gauge model provides a dynamical mechanism to generate the heavy neutrino masses, and thus the light neutrino masses through a seesaw. In this case, the heavy neutrinos are naturally long-lived and can be probed in detectors at the lifetime frontier, as long as the gauge portals of the model still allow abundant production.

Appendix A

`FEYNRULES` Model for the $B-L$ Gauge Model

`FeynRules` is a `MATHEMATICA`-based package which can implement the particle physics models with their specified list of fields, parameters and Lagrangian, to output a UFO model file which can be fed to high-energy physics event generator tools such as `CALCHEP`, `FEYNARTS`, `MADGRAPH`, `SHERPA` and `WHIZARD` to perform Monte Carlo simulation.

There exists a model file for the $B-L$ gauge model for `FeynRules` versions older than v1.6.2 which cannot output an UFO [44]. Based on this file, we write the FeynRules model file of the $B-L$ gauge model using the syntax for `FeynRules` version v.1.6.2 and above, thus it can output its corresponding UFO model file which can be used to generate events using `MadGraph5_aMC@NLO` and `Herwig`. The new files are published in the `FeynRules` model database at `https://feynrules.irmp.ucl.ac.be/wiki/B-L-SM`.

We here briefly introduce the file of our $B-L$ model [2], as shown in the B-L_4.fr at `https://feynrules.irmp.ucl.ac.be/wiki/B-L-SM`. A standard `FeynRules` model contains sections including model information, gauge groups, index definitions, the model parameters, particle classes and the Lagrangian. Among this, the $B-L$ gauge model contains the gauge groups, particle classes, the model parameters and Lagrangian in addition to the SM. In the following discussions, we will show the additional information of the $B-L$ gauge model explicitly in `FeynRules` syntax as introduced in Ref. [2].

The $B-L$ gauge model contains an additional $U(1)_{B-L}$ gauge factor. In `FeynRules` syntax, it is defined as

```
    U1BL  == {
      Abelian          -> True,
      CouplingConstant -> g1p,
      GaugeBoson       -> Bp,
      Charge           -> BL
    },
```

The model contains additional particles such as an additional scalar singlet χ, and an additional physical state of the Higgs h_2,

```
(* Higgs: unphysical scalars  *)
  S[12] == {
    ClassName       -> Xi,
    Unphysical      -> True,
    SelfConjugate   -> False,
    QuantumNumbers  -> {Y -> 0, BL -> 2},
    Definitions     -> {
        Xi -> (xev - Sa*H1 + Ca*H2 + I phip)/Sqrt[2]
    }
  },
```

where an additional Goldstone phip is set to zero if the unitary gauge is chosen, Sa and Ca are the sine and cosine for the Higgs mixing angle.

The model also contains an additional gauge boson B' and its physical state Z', as defined as

```
  V[5] == {
    ClassName        -> Zp,
    SelfConjugate    -> True,
    Indices          -> {},
```

```
    Mass              -> {MZp, 1500},
    Width             -> {WZp, 80.00},
    ParticleName      -> "Zp",
    PDG               -> 9900032,
    PropagatorLabel   -> "Zp",
    PropagatorType    -> Sine,
    PropagatorArrow   -> None,
    FullName          -> "Zp"
  },
  V[6] == {
    ClassName         -> Bp,
    SelfConjugate     -> True,
    Indices           -> {},
    Definitions       -> {Bp[mu_] -> Zp[mu]},
    Unphysical         -> True
  },
```

the default mass of Z' is set to be 1500 GeV, which can be changed in the run_card.dat of the generated process in the event generator tool.

The additional RH neutrinos ν_{Ri} and heavy physical state N_i besides the left-handed neutrinos ν_L and light physical state ν are defined as nR and nH in the model file,

```
  F[16] == {
    ClassName         -> nH,
    ClassMembers      -> {nH1, nH2, nH3},
    Indices           -> {Index[Generation]},
    FlavorIndex       -> Generation,
    SelfConjugate     -> True,
    QuantumNumbers    -> {LeptonNumber -> 1},
    Mass              -> {
        MnH,{MnH1, 200.00},{MnH2, 200.00},{MnH3, 200.00}},
```

```
  Width             -> 10^(-13),
  PropagatorLabel  -> {"nH","nuh1","nuh2","nuh3"},
  PropagatorType   -> Straight,
  PropagatorArrow  -> Forward,
  PDG              -> {9910012, 9910014, 9910016},
  ParticleName     -> {"nH1","nH2","nH3"},
  FullName         -> {"Heavy neutrino 1",
      "Heavy neutrino 2", "Heavy neutrino 3"}
},
(* Flavour eigenstates of neutrinos: unphysical *)
F[17] == {
  ClassName        -> nF,
  ClassMembers     -> {nF1,nF2,nF3},
  Indices          -> {Index[Generation]},
  FlavorIndex      -> Generation,
  SelfConjugate    -> True,
  Unphysical       -> True,
  Definitions      -> {
      nF[sp_,ff_] -> Can[ff] nL[sp,ff]-San[ff] nH[sp,ff]},
},
F[18] == {
  ClassName        -> nR,
  ClassMembers     -> {nR1,nR2,nR3},
  Indices          -> {Index[Generation]},
  FlavorIndex      -> Generation,
  SelfConjugate    -> True,
  Unphysical       -> True,
  Definitions      -> {
      nR[sp_,ff_] -> San[ff] nL[sp,ff]+Can[ff] nH[sp,ff]},
},
```

```
  (* Lefthanded flavor lepton doublet: unphysical *)
 F[11] == {
   ClassName      -> LL,
   Unphysical     -> True,
   Indices        -> {Index[SU2D], Index[Generation]},
   FlavorIndex    -> SU2D,
   SelfConjugate  -> False,
   QuantumNumbers -> {Y -> -1/2, BL -> -1},
   Definitions    -> {
       LL[sp1_,1,ff_] :>
       Module[{sp2}, ProjM[sp1,sp2] nF[sp2,ff]],
       LL[sp1_,2,ff_] :>
       Module[{sp2}, ProjM[sp1,sp2] l[sp2,ff]] }
 },
  (* Righthanded flavor neutrino singlet: unphysical *)
 F[20] == {
   ClassName        -> VR,
   Unphysical       -> True,
   Indices          -> {Index[Generation]},
   QuantumNumbers   -> {Y -> 0, BL -> -1},
   FlavorIndex      -> Generation,
   SelfConjugate    -> True,
   Definitions      -> {
       VR[sp1_,ff_] :>
       Module[{sp2}, ProjP[sp1,sp2] nR[sp2,ff]]}
 },
```

where San and Can are the sine and cosine for the neutrino mixing angles.

In addition, in all unphysical states of the SM particle classes, their corresponding $B-L$ number is added to the their QuantumNumbers line. The ghosts and Goldstone bosons are set to zero if the unitary gauge is set. Otherwise, the ghosts and Goldstone bosons are defined analogous to the SM.

Six additional parameters m_{h_2}, $\sin\alpha$, $m_{Z'}$, g_{B-L}, m_N and V_{lN} are added to the model parameters section analogous to the SM. Among them, the neutrino mixing V_{lN} are given in the form of the sine and cosine of the neutrino mixing angles. Besides, the extra Yukawa matrixs y^{ν}, y^M are also added as internal parameters ynd and ynm, following the Type-I seesaw relations. It also has additional parameters for the quadratic coupling m_{χ}^2 and quartic couplings $\lambda_{1,2,3}$ of the scalar potential defined as mu2H2, lam1, lam2 and lam3.

The model also contains the extra Lagrangian as shown in Eqn. (3.1). The scalar part contains additional terms as shown in Eqn. (3.4) such as

```
+ DC[Xibar,mu] DC[Xi,mu]
- mu2H2 Xibar Xi
- lam2 Xibar Xi Xibar Xi- lam3 Phibar[ii]Phi[ii] Xibar Xi
```

The gauge part contains extra terms,

```
-1/4 FS[Bp,mu,nu] FS[Bp,mu,nu],
```

The Fermion part contains extra terms,

```
+ VRbar.Ga[mu].DC[VR,mu].
```

The Yukawa part contains extra terms for the neutrino masses as shown in Eqn. (3.6),

```
    -ynd[ff1] LLbar[sp,ii,ff1].VR[sp,ff1]Phibar[ii]
    -ynm[ff1] nRbar[sp,ff1].VR[sp,ff1]Xi.
```

Finally, the $B-L$ gauge model introduces additional gauge-fixing terms in the Lagrangian. The additional ghost Lagrangian of the model in the Feynman gauge is given in Eqn. (2.44) of the Ref. [149], and is defined in the model file

```
LGhBp := - ghBpbar.del[del[ghBp, mu],mu];
LGhphi = -2*g1p MZp (xev-Sa*H1+Ca*H2) ghZpbar.ghZp.
```

If the gauge is set to the unitary gauge, as only gluonic ghosts exists, the above additional ghost terms vanish.

Appendix B

Renormalisation Group Equations

Here we briefly list the RGEs of the gauged $B-L$ model at one-loop level as given in Ref. [47]. In the gauge sector, the RGEs for the gauge couplings constants g_1 (associated with $U(1)_Y$), g ($SU(2)_L$), g_s ($SU(3)$) and g_{B-L} ($U(1)_{B-L}$) are expressed as

$$16\pi^2 \frac{d}{dt} g_1 = \frac{41}{6} {g_1}^3, \tag{B.1}$$

$$16\pi^2 \frac{d}{dt} g = -\frac{19}{6} g^3, \tag{B.2}$$

$$16\pi^2 \frac{d}{dt} g_s = -7 g_s^3, \tag{B.3}$$

$$16\pi^2 \frac{d}{dt} g_{B-L} = 12 {g_{B-L}}^3 + \frac{32}{3} g_{B-L} \tilde{g} + \frac{41}{6} g_{B-L} \tilde{g}^2, \tag{B.4}$$

$$16\pi^2 \frac{d}{dt} \tilde{g} = \frac{41}{6} \tilde{g}(\tilde{g}^2 + 2g_1^2) + \frac{32}{3} g_{B-L}(\tilde{g}^2 + g_1^2) + 12 {g_{B-L}}^2 \tilde{g}. \tag{B.5}$$

Here $\tilde{g}$ is the $U(1)_Y - U(1)_{B-L}$ mixing which we omit in this work.

In the scalar sector, the RGEs for the couplings λ_1, λ_2, λ_3, are given by

$$16\pi^2 \frac{d}{dt}\lambda_1 = 24\lambda_1^2 + \lambda_3^2 - 6Y_t^4 + \frac{9}{8}g^4 + \frac{3}{8}g_1^4 + \frac{3}{4}g^2 g_1^2 + \frac{3}{4}g^2 \tilde{g}^2 + \frac{3}{4}g_1^2 \tilde{g}^2, \\ + \frac{3}{8}\tilde{g}^4 + 12\lambda_1 Y_t^2 - 9\lambda_1 g^2 - 3\lambda_1 g_1^2 - 3\lambda_1 \tilde{g}^2, \tag{B.6}$$

$$8\pi^2 \frac{d}{dt}\lambda_2 = 10\lambda_2^2 + \lambda_3^2 - \frac{1}{2}\text{Tr}[(y^M)^4] + 48{g_{B-L}}^4 + 4\lambda_2 \text{Tr}[(y^M)^2] - 24\lambda_2 {g_{B-L}}^2, \tag{B.7}$$

$$8\pi^2 \frac{d}{dt}\lambda_3 = \lambda_3 \left(6\lambda_1 + 4\lambda_2 + 2\lambda_3 + 3Y_t^2 - \frac{3}{4}(3g - g_1^2 - \tilde{g}^2) + 2\text{Tr}[(y^M)^2] - 12{g_{B-L}}^2\right) \\ + 6\tilde{g}^2 {g_{B-L}}^2. \tag{B.8}$$

Finally, for the Yukawa couplings, only the RGEs of the large top quark Yukawa coupling Y_t and the (potentially large) Majorana Yukawa coupling y_{ij}^M are considered for simplicity, as other couplings are small thus not likely to affect the perturbativity condition. They are given by

$$16\pi^2 \frac{d}{dt}Y_t = Y_t[\frac{9}{2}Y_t^2 - 8g_s^2 - \frac{9}{4}g^2 - \frac{17}{12}g_1^2 - \frac{17}{12}\tilde{g}^2 - \frac{2}{3}g_{B-L} - \frac{5}{3}\tilde{g}g_{B-L}], \tag{B.9}$$

$$16\pi^2 \frac{d}{dt}y_i^M = y_i^M[4(y_i^M)^2 + 2Tr[(y^M)^2] - 6g_{B-L}]. \tag{B.10}$$

As before, we assume diagonal Majorana neutrino Yukawa couplings $y_{ij}^M = y_i^M \delta_{ij}$.

Bibliography

[1] Jonathan M. Butterworth, David Grellscheid, Michael Krämer, Björn Sarrazin, and David Yallup. Constraining new physics with collider measurements of Standard Model signatures. *JHEP*, 03:078, 2017.

[2] Adam Alloul, Neil D. Christensen, Céline Degrande, Claude Duhr, and Benjamin Fuks. FeynRules 2.0 - A complete toolbox for tree-level phenomenology. *Comput. Phys. Commun.*, 185:2250–2300, 2014.

[3] Celine Degrande, Claude Duhr, Benjamin Fuks, David Grellscheid, Olivier Mattelaer, and Thomas Reiter. UFO - The Universal FeynRules Output. *Comput. Phys. Commun.*, 183:1201–1214, 2012.

[4] R. Davis. A review of the Homestake solar neutrino experiment. *Prog. Part. Nucl. Phys.*, 32:13–32, 1994.

[5] B. T. Cleveland, Timothy Daily, Raymond Davis, Jr., James R. Distel, Kenneth Lande, C. K. Lee, Paul S. Wildenhain, and Jack Ullman. Measurement of the solar electron neutrino flux with the Homestake chlorine detector. *Astrophys. J.*, 496:505–526, 1998.

[6] J. N. Abdurashitov et al. Measurement of the solar neutrino capture rate with gallium metal. *Phys. Rev.*, C60:055801, 1999.

[7] Carla Maria Cattadori. Update of solar neutrino interaction rate measurements from GNO at LNGS. *Nucl. Phys. Proc. Suppl.*, 110:311–314, 2002.

[8] W. Hampel et al. GALLEX solar neutrino observations: Results for GALLEX IV. *Phys. Lett.*, B447:127–133, 1999.

[9] M. Altmann et al. GNO solar neutrino observations: Results for GNO I. *Phys. Lett.*, B490:16–26, 2000.

[10] S. Fukuda et al. Determination of solar neutrino oscillation parameters using 1496 days of Super-Kamiokande I data. *Phys. Lett.*, B539:179–187, 2002.

[11] Q. R. Ahmad et al. Direct evidence for neutrino flavor transformation from neutral current interactions in the Sudbury Neutrino Observatory. *Phys. Rev. Lett.*, 89:011301, 2002.

[12] Q. R. Ahmad et al. Measurement of day and night neutrino energy spectra at SNO and constraints on neutrino mixing parameters. *Phys. Rev. Lett.*, 89:011302, 2002.

[13] S. N. Ahmed et al. Measurement of the total active B-8 solar neutrino flux at the Sudbury Neutrino Observatory with enhanced neutral current sensitivity. *Phys. Rev. Lett.*, 92:181301, 2004.

[14] Y. Fukuda et al. Evidence for oscillation of atmospheric neutrinos. *Phys. Rev. Lett.*, 81:1562–1567, 1998.

[15] A. Surdo. Atmospheric neutrino oscillations in the MACRO experiment. *Nucl. Phys. Proc. Suppl.*, 110:342–345, 2002.

[16] Mayly C. Sanchez et al. Measurement of the L/E distributions of atmospheric neutrinos in Soudan 2 and their interpretation as neutrino oscillations. *Phys. Rev.*, D68:113004, 2003.

[17] K. Eguchi et al. First results from KamLAND: Evidence for reactor anti-neutrino disappearance. *Phys. Rev. Lett.*, 90:021802, 2003.

[18] M. H. Ahn et al. Indications of neutrino oscillation in a 250 km long baseline experiment. *Phys. Rev. Lett.*, 90:041801, 2003.

[19] Murray Gell-Mann, Pierre Ramond, and Richard Slansky. Complex Spinors and Unified Theories. *Conf. Proc.*, C790927:315–321, 1979.

[20] Osamu Sawada and Akio Sugamoto, editors. *Proceedings: Workshop on the Unified Theories and the Baryon Number in the Universe*, Tsukuba, Japan, 1979. Natl.Lab.High Energy Phys., Natl.Lab.High Energy Phys.

[21] Rabindra N. Mohapatra and Goran Senjanovic. Neutrino Mass and Spontaneous Parity Nonconservation. *Phys. Rev. Lett.*, 44:912, 1980. [,231(1979)].

[22] Rabindra N. Mohapatra and R. E. Marshak. Local B-L Symmetry of Electroweak Interactions, Majorana Neutrinos and Neutron Oscillations. *Phys. Rev. Lett.*, 44:1316–1319, 1980. [Erratum: Phys. Rev. Lett.44,1643(1980)].

[23] Arindam Das, Nobuchika Okada, and Nathan Papapietro. Electroweak vacuum stability in classically conformal B-L extension of the Standard Model. *Eur. Phys. J.*, C77(2):122, 2017.

[24] Arindam Das, Satsuki Oda, Nobuchika Okada, and Dai-suke Takahashi. Classically conformal U(1)' extended standard model, electroweak vacuum stability, and LHC Run-2 bounds. *Phys. Rev.*, D93(11):115038, 2016.

[25] Claudio Coriano, Luigi Delle Rose, and Carlo Marzo. Vacuum Stability in U(1)-Prime Extensions of the Standard Model with TeV Scale Right Handed Neutrinos. *Phys. Lett.*, B738:13–19, 2014.

[26] Claudio Coriano, Luigi Delle Rose, and Carlo Marzo. Constraints on abelian extensions of the Standard Model from two-loop vacuum stability and $U(1)_{B-L}$. *JHEP*, 02:135, 2016.

[27] Elena Accomando, Claudio Coriano, Luigi Delle Rose, Juri Fiaschi, Carlo Marzo, and Stefano Moretti. Z, Higgses and heavy neutrinos in U(1) models: from the LHC to the GUT scale. *JHEP*, 07:086, 2016.

[28] Elena Accomando, Luigi Delle Rose, Stefano Moretti, Emmanuel Olaiya, and Claire H. Shepherd-Themistocleous. Novel SM-like Higgs decay into displaced heavy neutrino pairs in U(1) models. *JHEP*, 04:081, 2017.

[29] Elena Accomando, Luigi Delle Rose, Stefano Moretti, Emmanuel Olaiya, and Claire H. Shepherd-Themistocleous. Extra Higgs boson and Z as portals to signatures of heavy neutrinos at the LHC. *JHEP*, 02:109, 2018.

[30] Michael Klasen, Florian Lyonnet, and Farinaldo S. Queiroz. NLO+NLL collider bounds, Dirac fermion and scalar dark matter in the B–L model. *Eur. Phys. J.*, C77(5):348, 2017.

[31] Philip Ilten, Yotam Soreq, Mike Williams, and Wei Xue. Serendipity in dark photon searches. *JHEP*, 06:004, 2018.

[32] Manfred Lindner, Farinaldo S. Queiroz, Werner Rodejohann, and Xun-Jie Xu. Neutrino-electron scattering: general constraints on Z and dark photon models. *JHEP*, 05:098, 2018.

[33] Elena Accomando, Juri Fiaschi, Stefano Moretti, and Claire H. Shepherd-Themistocleous. Constraining Z' widths from p_T measurements in Drell-Yan processes. *Phys. Rev.*, D96(7):075019, 2017.

[34] S. Khalil and S. Moretti. Heavy neutrinos, Z' and Higgs bosons at the LHC: new particles from an old symmetry. *J. Mod. Phys.*, 4(1):7–10, 2013.

[35] Lorenzo Basso, Stefano Moretti, and Giovanni Marco Pruna. The Higgs sector of the minimal $B-L$ model at future Linear Colliders. *Eur. Phys. J.*, C71:1724, 2011.

[36] Lorenzo Basso, Alexander Belyaev, Stefano Moretti, Giovanni Marco Pruna, and Claire H. Shepherd-Themistocleous. Z'_{B-L} discovery potential at the LHC for $\sqrt{s} = 7$ TeV. *PoS*, ICHEP2010:381, 2010.

[37] Lorenzo Basso, Stefano Moretti, and Giovanni Marco Pruna. Phenomenology of the minimal $B-L$ extension of the Standard Model: the Higgs sector. *Phys. Rev.*, D83:055014, 2011.

[38] L. Basso, A. Belyaev, S. Moretti, and G. M. Pruna. Higgs phenomenology in the minimal $B-L$ extension of the Standard Model at LHC. *J. Phys. Conf. Ser.*, 259:012062, 2010.

[39] Lorenzo Basso, Stefano Moretti, and Giovanni Marco Pruna. Constraining the g'_1 coupling in the minimal $B-L$ Model. *J. Phys.*, G39:025004, 2012.

[40] Lorenzo Basso, Stefano Moretti, and Giovanni Marco Pruna. A Renormalisation Group Equation Study of the Scalar Sector of the Minimal B-L Extension of the Standard Model. *Phys. Rev.*, D82:055018, 2010.

[41] Lorenzo Basso, Alexander Belyaev, Stefano Moretti, Giovanni Marco Pruna, and Claire H. Shepherd-Themistocleous. Z' discovery potential at the LHC in the minimal $B-L$ extension of the Standard Model. *Eur. Phys. J.*, C71:1613, 2011.

[42] L. Basso, A. Belyaev, S. Moretti, and G. M. Pruna. The Z' boson of the minimal B-L model at future Linear Colliders in e+e- –> mu+mu-. *Nuovo Cim.*, C33N2:171–174, 2010.

[43] Lorenzo Basso, Alexander Belyaev, Stefano Moretti, and Giovanni Marco Pruna. Probing the Z-prime sector of the minimal B-L model at future Linear Colliders in the e+ e- —> mu+ mu- process. *JHEP*, 10:006, 2009.

[44] Lorenzo Basso, Alexander Belyaev, Stefano Moretti, and Claire H. Shepherd-Themistocleous. Phenomenology of the minimal B-L extension of the Standard model: Z' and neutrinos. *Phys. Rev.*, D80:055030, 2009.

[45] Tania Robens and Tim Stefaniak. Status of the Higgs Singlet Extension of the Standard Model after LHC Run 1. *Eur. Phys. J.*, C75:104, 2015.

[46] D. López-Val and T. Robens. r and the W-boson mass in the singlet extension of the standard model. *Phys. Rev.*, D90:114018, 2014.

[47] Joydeep Chakrabortty, Partha Konar, and Tanmoy Mondal. Constraining a class of B-L extended models from vacuum stability and perturbativity. *Phys. Rev.*, D89(5):056014, 2014.

[48] T. Aaltonen et al. Search for High-Mass e^+ e- Resonances in $p\bar{p}$ Collisions at $\sqrt{s}$ = 1.96-TeV. *Phys. Rev. Lett.*, 102:031801, 2009.

[49] T. Aaltonen et al. A Search for high-mass resonances decaying to dimuons at CDF. *Phys. Rev. Lett.*, 102:091805, 2009.

[50] Marcela Carena, Alejandro Daleo, Bogdan A. Dobrescu, and Timothy M. P. Tait. Z' gauge bosons at the Tevatron. *Phys. Rev.*, D70:093009, 2004.

[51] G. Cacciapaglia, C. Csaki, G. Marandella, and A. Strumia. The Minimal Set of Electroweak Precision Parameters. *Phys. Rev.*, D74:033011, 2006.

[52] P. L. Anthony et al. Observation of parity nonconservation in Moller scattering. *Phys. Rev. Lett.*, 92:181602, 2004.

[53] the SLD Electroweak. A Combination of preliminary electroweak measurements and constraints on the standard model. 2003.

[54] Serguei Chatrchyan et al. Search for narrow resonances in dilepton mass spectra in pp collisions at $\sqrt{s} = 7$ TeV. *Phys. Lett.*, B714:158–179, 2012.

[55] Vardan Khachatryan et al. Search for physics beyond the standard model in dilepton mass spectra in proton-proton collisions at $\sqrt{s} = 8$ TeV. *JHEP*, 04:025, 2015.

[56] Morad Aaboud et al. Search for new high-mass phenomena in the dilepton final state using 36 fb^{-1} of proton-proton collision data at $\sqrt{s} = 13$ TeV with the ATLAS detector. *JHEP*, 10:182, 2017.

[57] Albert M Sirunyan et al. Search for high-mass resonances in dilepton final states in proton-proton collisions at $\sqrt{s} = 13$ TeV. *JHEP*, 06:120, 2018.

[58] Georges Aad et al. Search for high-mass dilepton resonances using 139 fb^{-1} of pp collision data collected at $\sqrt{s}$ =13 TeV with the ATLAS detector. *Phys. Lett.*, B796:68–87, 2019.

[59] Albert M Sirunyan et al. Combination of CMS searches for heavy resonances decaying to pairs of bosons or leptons. *Phys. Lett.*, B798:134952, 2019.

[60] Bernard Aubert et al. Search for Dimuon Decays of a Light Scalar Boson in Radiative Transitions Upsilon $\rightarrow$ gamma A0. *Phys. Rev. Lett.*, 103:081803, 2009.

[61] J. P. Lees et al. Search for a Dark Photon in e^+e^- Collisions at BaBar. *Phys. Rev. Lett.*, 113(20):201801, 2014.

[62] J. R. Batley et al. Search for the dark photon in π^0 decays. *Phys. Lett.*, B746:178–185, 2015.

[63] H. Merkel et al. Search at the Mainz Microtron for Light Massive Gauge Bosons Relevant for the Muon g-2 Anomaly. *Phys. Rev. Lett.*, 112(22):221802, 2014.

[64] S. Abrahamyan et al. Search for a New Gauge Boson in Electron-Nucleus Fixed-Target Scattering by the APEX Experiment. *Phys. Rev. Lett.*, 107:191804, 2011.

[65] D. Banerjee et al. Search for invisible decays of sub-GeV dark photons in missing-energy events at the CERN SPS. *Phys. Rev. Lett.*, 118(1):011802, 2017.

[66] D. Banerjee et al. Search for vector mediator of Dark Matter production in invisible decay mode. *Phys. Rev.*, D97(7):072002, 2018.

[67] F. Archilli et al. Search for a vector gauge boson in ϕ meson decays with the KLOE detector. *Phys. Lett.*, B706:251–255, 2012.

[68] A. Anastasi et al. Limit on the production of a low-mass vector boson in $e^+e^- \to U\gamma$, $U \to e^+e^-$ with the KLOE experiment. *Phys. Lett.*, B750:633–637, 2015.

[69] Martin Bauer, Patrick Foldenauer, and Joerg Jaeckel. Hunting All the Hidden Photons. *JHEP*, 07:094, 2018.

[70] P. Vilain et al. Measurement of differential cross-sections for muon-neutrino electron scattering. *Phys. Lett.*, B302:351–355, 1993.

[71] Properties of the Higgs-like boson in the decay H to ZZ to 4l in pp collisions at sqrt s =7 and 8 TeV. Technical Report CMS-PAS-HIG-13-002, CERN, Geneva, 2013.

[72] Evidence for a particle decaying to W+W- in the fully leptonic final state in a standard model Higgs boson search in pp collisions at the LHC. Technical Report CMS-PAS-HIG-13-003, CERN, Geneva, 2013.

[73] Vardan Khachatryan et al. Search for a Higgs boson in the mass range from 145 to 1000 GeV decaying to a pair of W or Z bosons. *JHEP*, 10:144, 2015.

[74] Search for a new scalar resonance decaying to a pair of Z bosons in proton-proton collisions at $\sqrt{s}$ = 13 TeV. Technical Report CMS-PAS-HIG-17-012, CERN, Geneva, 2017.

[75] Philip Bechtle, Sven Heinemeyer, Oscar Stal, Tim Stefaniak, and Georg Weiglein. Applying Exclusion Likelihoods from LHC Searches to Extended Higgs Sectors. *Eur. Phys. J.*, C75(9):421, 2015.

[76] Tania Robens and Tim Stefaniak. LHC Benchmark Scenarios for the Real Higgs Singlet Extension of the Standard Model. *Eur. Phys. J.*, C76(5):268, 2016.

[77] Guillaume Chalons, David Lopez-Val, Tania Robens, and Tim Stefaniak. The Higgs singlet extension at LHC Run 2. *PoS*, ICHEP2016:1180, 2016.

[78] Agnieszka Ilnicka, Tania Robens, and Tim Stefaniak. Constraining Extended Scalar Sectors at the LHC and beyond. *Mod. Phys. Lett.*, A33(10n11):1830007, 2018.

[79] Jochen Meyer. Search for additional Higgs bosons. *Nuovo Cim.*, C40(6):203, 2018.

[80] Serguei Chatrchyan et al. Search for heavy Majorana neutrinos in $\mu^{\pm}\mu^{\pm}+$ jets and $e^{\pm}e^{\pm}+$ jets events in pp collisions at $\sqrt{s} = 7$ TeV. *Phys. Lett.*, B717:109–128, 2012.

[81] Search for Majorana neutrino production in pp collisions at sqrt(s)=7 TeV in dimuon final states with the ATLAS detector. Technical Report ATLAS-CONF-2012-139, CERN, Geneva, Sep 2012.

[82] Vardan Khachatryan et al. Search for heavy Majorana neutrinos in $\mu^{\pm}\mu^{\pm}+$ jets events in proton-proton collisions at $\sqrt{s}$ = 8 TeV. *Phys. Lett.*, B748:144–166, 2015.

[83] Albert M Sirunyan et al. Search for heavy neutral leptons in events with three charged leptons in proton-proton collisions at $\sqrt{s} = 13$ TeV. *Phys. Rev. Lett.*, 120(22):221801, 2018.

[84] Georges Aad et al. Search for heavy neutral leptons in decays of W bosons produced in 13 TeV pp collisions using prompt and displaced signatures with the ATLAS detector. *JHEP*, 10:265, 2019.

[85] Vardan Khachatryan et al. Search for long-lived particles that decay into final states containing two electrons or two muons in proton-proton collisions at $\sqrt{s} = 8$ TeV. *Phys. Rev.*, D91(5):052012, 2015.

[86] Search for long-lived particles decaying to final states that include dileptons. Technical Report CMS-PAS-EXO-12-037, CERN, Geneva, 2014.

[87] Search for long-lived particles that decay into final states containing two muons, reconstructed using only the CMS muon chambers. Technical Report CMS-PAS-EXO-14-012, CERN, Geneva, 2015.

[88] Albert M Sirunyan et al. Search for heavy Majorana neutrinos in same-sign dilepton channels in proton-proton collisions at $\sqrt{s} = 13$ TeV. *JHEP*, 01:122, 2019.

[89] Albert M Sirunyan et al. Search for Evidence of the Type-III Seesaw Mechanism in Multilepton Final States in Proton-Proton Collisions at $\sqrt{s} = 13$ TeV. *Phys. Rev. Lett.*, 119(22):221802, 2017.

[90] Frank F. Deppisch, Wei Liu, and Manimala Mitra. Long-lived Heavy Neutrinos from Higgs Decays. *JHEP*, 08:181, 2018.

[91] Frank Deppisch, Suchita Kulkarni, and Wei Liu. Heavy neutrino production via Z' at the lifetime frontier. *Phys. Rev.*, D100(3):035005, 2019.

[92] E. Fermi. An attempt of a theory of beta radiation. 1. *Z. Phys.*, 88:161–177, 1934.

[93] Gerard ’t Hooft and M. J. G. Veltman. Regularization and Renormalization of Gauge Fields. *Nucl. Phys.*, B44:189–213, 1972.

[94] Chen-Ning Yang and Robert L. Mills. Conservation of Isotopic Spin and Isotopic Gauge Invariance. *Phys. Rev.*, 96:191–195, 1954. [,150(1954)].

[95] Philip W. Anderson. Plasmons, Gauge Invariance, and Mass. *Phys. Rev.*, 130:439–442, 1963. [,153(1963)].

[96] Peter W. Higgs. Broken Symmetries and the Masses of Gauge Bosons. *Phys. Rev. Lett.*, 13:508–509, 1964. [,160(1964)].

[97] F. Englert and R. Brout. Broken Symmetry and the Mass of Gauge Vector Mesons. *Phys. Rev. Lett.*, 13:321–323, 1964. [,157(1964)].

[98] G. S. Guralnik, C. R. Hagen, and T. W. B. Kibble. Global Conservation Laws and Massless Particles. *Phys. Rev. Lett.*, 13:585–587, 1964. [,162(1964)].

[99] Alexander A. Migdal and Alexander M. Polyakov. SPONTANEOUS BREAKDOWN OF STRONG INTERACTION SYMMETRY AND THE ABSENCE OF MASSLESS PARTICLES. *Sov. Phys. JETP*, 24:91–98, 1967. [Zh. Eksp. Teor. Fiz.51,135(1966)].

[100] S. L. Glashow. Partial Symmetries of Weak Interactions. *Nucl. Phys.*, 22:579–588, 1961.

[101] Steven Weinberg. A Model of Leptons. *Phys. Rev. Lett.*, 19:1264–1266, 1967.

[102] Abdus Salam. Weak and Electromagnetic Interactions. *Conf. Proc.*, C680519:367–377, 1968.

[103] Richard P. Feynman. Very high-energy collisions of hadrons. *Phys. Rev. Lett.*, 23:1415–1417, 1969. [,494(1969)].

[104] J. D. Bjorken and Emmanuel A. Paschos. Inelastic Electron Proton and gamma Proton Scattering, and the Structure of the Nucleon. *Phys. Rev.*, 185:1975–1982, 1969.

[105] David J. Gross and Frank Wilczek. Ultraviolet Behavior of Nonabelian Gauge Theories. *Phys. Rev. Lett.*, 30:1343–1346, 1973. [,271(1973)].

[106] H. David Politzer. Reliable Perturbative Results for Strong Interactions? *Phys. Rev. Lett.*, 30:1346–1349, 1973. [,274(1973)].

[107] C. S. Wu, E. Ambler, R. W. Hayward, D. D. Hoppes, and R. P. Hudson. Experimental Test of Parity Conservation in Beta Decay. *Phys. Rev.*, 105:1413–1414, 1957.

[108] Makoto Kobayashi and Toshihide Maskawa. CP Violation in the Renormalizable Theory of Weak Interaction. *Prog. Theor. Phys.*, 49:652–657, 1973.

[109] Lincoln Wolfenstein. Parametrization of the Kobayashi-Maskawa Matrix. *Phys. Rev. Lett.*, 51:1945, 1983.

[110] Georges Aad et al. Observation of a new particle in the search for the Standard Model Higgs boson with the ATLAS detector at the LHC. *Phys. Lett.*, B716:1–29, 2012.

[111] Serguei Chatrchyan et al. Observation of a New Boson at a Mass of 125 GeV with the CMS Experiment at the LHC. *Phys. Lett.*, B716:30–61, 2012.

[112] Steven Weinberg. Implications of Dynamical Symmetry Breaking. *Phys. Rev.*, D13:974–996, 1976. [Addendum: Phys. Rev.D19,1277(1979)].

[113] W. J. G. de Blok, Stacy S. McGaugh, Albert Bosma, and Vera C. Rubin. Mass density profiles of LSB galaxies. *Astrophys. J.*, 552:L23–L26, 2001.

[114] Gianfranco Bertone, Dan Hooper, and Joseph Silk. Particle dark matter: Evidence, candidates and constraints. *Phys. Rept.*, 405:279–390, 2005.

[115] Adam G. Riess et al. Observational evidence from supernovae for an accelerating universe and a cosmological constant. *Astron. J.*, 116:1009–1038, 1998.

[116] Sean M. Carroll. The Cosmological constant. *Living Rev. Rel.*, 4:1, 2001.

[117] P. A. R. Ade et al. Planck 2013 results. I. Overview of products and scientific results. *Astron. Astrophys.*, 571:A1, 2014.

[118] R. Adam et al. Planck 2015 results. I. Overview of products and scientific results. *Astron. Astrophys.*, 594:A1, 2016.

[119] Alexandre Dolgov and Joseph Silk. Baryon isocurvature fluctuations at small scales and baryonic dark matter. *Phys. Rev.*, D47:4244–4255, 1993.

[120] A. D. Sakharov. Violation of CP Invariance, C asymmetry, and baryon asymmetry of the universe. *Pisma Zh. Eksp. Teor. Fiz.*, 5:32–35, 1967. [Usp. Fiz. Nauk161,no.5,61(1991)].

[121] Glennys R. Farrar and M. E. Shaposhnikov. Baryon asymmetry of the universe in the minimal Standard Model. *Phys. Rev. Lett.*, 70:2833–2836, 1993. [Erratum: Phys. Rev. Lett.71,210(1993)].

[122] A. Osipowicz et al. KATRIN: A Next generation tritium beta decay experiment with sub-eV sensitivity for the electron neutrino mass. Letter of intent. 2001.

[123] Stefano Dell'Oro, Simone Marcocci, Matteo Viel, and Francesco Vissani. Neutrinoless double beta decay: 2015 review. *Adv. High Energy Phys.*, 2016:2162659, 2016.

[124] P. A. R. Ade et al. Planck 2015 results. XIII. Cosmological parameters. *Astron. Astrophys.*, 594:A13, 2016.

[125] Ch. Kraus et al. Final results from phase II of the Mainz neutrino mass search in tritium beta decay. *Eur. Phys. J.*, C40:447–468, 2005.

[126] V. N. Aseev et al. An upper limit on electron antineutrino mass from Troitsk experiment. *Phys. Rev.*, D84:112003, 2011.

[127] N. Aghanim et al. Planck 2018 results. VI. Cosmological parameters. 2018.

[128] M. Doi, T. Kotani, H. Nishiura, K. Okuda, and E. Takasugi. CP Violation in Majorana Neutrinos. *Phys. Lett.*, 102B:323–326, 1981.

[129] Zhi-zhong Xing. Texture zeros and Majorana phases of the neutrino mass matrix. *Phys. Lett.*, B530:159–166, 2002.

[130] L. Wolfenstein. Neutrino Oscillations in Matter. *Phys. Rev.*, D17:2369–2374, 1978. [,294(1977)].

[131] S. Adrian-Martinez et al. Letter of intent for KM3NeT 2.0. *J. Phys.*, G43(8):084001, 2016.

[132] M. Tanabashi et al. Review of Particle Physics. *Phys. Rev.*, D98(3):030001, 2018.

[133] M. Aker et al. Improved Upper Limit on the Neutrino Mass from a Direct Kinematic Method by KATRIN. *Phys. Rev. Lett.*, 123(22):221802, 2019.

[134] Stefano Dell'Oro, Simone Marcocci, and Francesco Vissani. New expectations and uncertainties on neutrinoless double beta decay. *Phys. Rev.*, D90(3):033005, 2014.

[135] F. Couchot, S. Henrot-Versillé, O. Perdereau, S. Plaszczynski, B. Rouillé d'Orfeuil, M. Spinelli, and M. Tristram. Cosmological constraints on the neutrino mass including systematic uncertainties. *Astron. Astrophys.*, 606:A104, 2017.

[136] Peter Minkowski. $\mu \to e\gamma$ at a Rate of One Out of 10^9 Muon Decays? *Phys. Lett.*, 67B:421–428, 1977.

[137] Tsutomu Yanagida. Horizontal gauge symmetry and masses of neutrinos. *Conf. Proc.*, C7902131:95–99, 1979.

[138] J. Schechter and J. W. F. Valle. Neutrino Masses in SU(2) x U(1) Theories. *Phys. Rev.*, D22:2227, 1980.

[139] Ivica Picek and Branimir Radovcic. Novel TeV-scale seesaw mechanism with Dirac mediators. *Phys. Lett.*, B687:338–341, 2010.

[140] Kresimir Kumericki, Ivica Picek, and Branimir Radovcic. TeV-scale Seesaw with Quintuplet Fermions. *Phys. Rev.*, D86:013006, 2012.

[141] Alexander Belyaev, Neil D. Christensen, and Alexander Pukhov. CalcHEP 3.4 for collider physics within and beyond the Standard Model. *Comput. Phys. Commun.*, 184:1729–1769, 2013.

[142] Thomas Hahn. Generating Feynman diagrams and amplitudes with FeynArts 3. *Comput. Phys. Commun.*, 140:418–431, 2001.

[143] T. Gleisberg, Stefan. Hoeche, F. Krauss, M. Schonherr, S. Schumann, F. Siegert, and J. Winter. Event generation with SHERPA 1.1. *JHEP*, 02:007, 2009.

[144] Wolfgang Kilian, Thorsten Ohl, and Jurgen Reuter. WHIZARD: Simulating Multi-Particle Processes at LHC and ILC. *Eur. Phys. J.*, C71:1742, 2011.

[145] Johan Alwall, Michel Herquet, Fabio Maltoni, Olivier Mattelaer, and Tim Stelzer. MadGraph 5 : Going Beyond. *JHEP*, 06:128, 2011.

[146] J. Alwall, R. Frederix, S. Frixione, V. Hirschi, F. Maltoni, O. Mattelaer, H. S. Shao, T. Stelzer, P. Torrielli, and M. Zaro. The automated computation of tree-level and next-to-leading order differential cross sections, and their matching to parton shower simulations. *JHEP*, 07:079, 2014.

[147] Johannes Bellm et al. Herwig 7.0/Herwig++ 3.0 release note. *Eur. Phys. J.*, C76(4):196, 2016.

[148] Wei Liu and Lorenzo Basso. The B-L model. `https://feynrules.irmp.ucl.ac.be/wiki/B-L-SM/`, 2018.

[149] Giovanni Marco Pruna. *Phenomenology of the minimal $B-L$ Model: the Higgs sector at the Large Hadron Collider and future Linear Colliders*. PhD thesis, Southampton U., 2011.

[150] F. del Aguila, M. Masip, and M. Perez-Victoria. Physical parameters and renormalization of U(1)-a x U(1)-b models. *Nucl. Phys.*, B456:531–549, 1995.

[151] We-Fu Chang, John N. Ng, and Jackson M. S. Wu. A Very Narrow Shadow Extra Z-boson at Colliders. *Phys. Rev.*, D74:095005, 2006. [Erratum: Phys. Rev.D79,039902(2009)].

[152] Daniel Feldman, Zuowei Liu, and Pran Nath. The Stueckelberg Z-prime Extension with Kinetic Mixing and Milli-Charged Dark Matter From the Hidden Sector. *Phys. Rev.*, D75:115001, 2007.

[153] Jason Kumar and James D. Wells. CERN LHC and ILC probes of hidden-sector gauge bosons. *Phys. Rev.*, D74:115017, 2006.

[154] Yoichiro Nambu. Quasiparticles and Gauge Invariance in the Theory of Superconductivity. *Phys. Rev.*, 117:648–663, 1960. [,132(1960)].

[155] J. Goldstone. Field Theories with Superconductor Solutions. *Nuovo Cim.*, 19:154–164, 1961.

[156] S. Amrith, J. M. Butterworth, F. F. Deppisch, W. Liu, A. Varma, and D. Yallup. LHC constraints on a *BL* gauge model using Contur. *JHEP*, 05:154, 2019.

[157] M. Awramik, M. Czakon, A. Freitas, and G. Weiglein. Precise prediction for the W boson mass in the standard model. *Phys. Rev.*, D69:053006, 2004.

[158] S. Heinemeyer, S. Kraml, W. Porod, and G. Weiglein. Physics impact of a precise determination of the top quark mass at an e^+e^- linear collider. *JHEP*, 09:075, 2003.

[159] J. Alcaraz et al. A Combination of preliminary electroweak measurements and constraints on the standard model. 2006.

[160] T. Aaltonen et al. Precise measurement of the W-boson mass with the CDF II detector. *Phys. Rev. Lett.*, 108:151803, 2012.

[161] Victor Mukhamedovich Abazov et al. Measurement of the W boson mass with the D0 detector. *Phys. Rev.*, D89(1):012005, 2014.

[162] S. Schael et al. Search for neutral MSSM Higgs bosons at LEP. *Eur. Phys. J.*, C47:547–587, 2006.

[163] Lyndon Evans and Philip Bryant. LHC Machine. *JINST*, 3:S08001, 2008.

[164] S. Chatrchyan et al. The CMS Experiment at the CERN LHC. *JINST*, 3:S08004, 2008.

[165] G. Aad et al. The ATLAS Experiment at the CERN Large Hadron Collider. *JINST*, 3:S08003, 2008.

[166] A. Augusto Alves, Jr. et al. The LHCb Detector at the LHC. *JINST*, 3:S08005, 2008.

[167] K. Aamodt et al. The ALICE experiment at the CERN LHC. *JINST*, 3:S08002, 2008.

[168] G. Anelli et al. The TOTEM experiment at the CERN Large Hadron Collider. *JINST*, 3:S08007, 2008.

[169] J. L. Pinfold. The MoEDAL Experiment at the LHC – a New Light on the Terascale Frontier. *J. Phys. Conf. Ser.*, 631(1):012014, 2015.

[170] O. Adriani et al. The LHCf detector at the CERN Large Hadron Collider. *JINST*, 3:S08006, 2008.

[171] G. L. Bayatian et al. *CMS Physics: Technical Design Report Volume 1: Detector Performance and Software*. Technical Design Report CMS. CERN, Geneva, 2006.

[172] A. Airapetian et al. *ATLAS detector and physics performance: Technical Design Report, 1*. Technical Design Report ATLAS. CERN, Geneva, 1999.

[173] R. Antunes-Nobrega et al. *LHCb reoptimized detector design and performance: Technical Design Report*. Technical Design Report LHCb. CERN, Geneva, 2003.

[174] Gavin P. Salam. Towards Jetography. *Eur. Phys. J.*, C67:637–686, 2010.

[175] Georges Aad et al. Topological cell clustering in the ATLAS calorimeters and its performance in LHC Run 1. *Eur. Phys. J.*, C77:490, 2017.

[176] Nazar Bartosik. Diagram showing the common principle of identification of jets initiated by b-hadron decays. `http://bartosik.pp.ua/hep_sketches/btagging`.

[177] Stefan Antusch, Eros Cazzato, and Oliver Fischer. Sterile neutrino searches via displaced vertices at LHCb. *Phys. Lett.*, B774:114–118, 2017.

[178] Search for light vector resonances decaying to a quark pair produced in association with a jet in proton-proton collisions at $\sqrt{s} = 13$ TeV. Technical Report CMS-PAS-EXO-17-001, CERN, Geneva, 2017.

[179] Albert M Sirunyan et al. Search for high mass dijet resonances with a new background prediction method in proton-proton collisions at $\sqrt{s} = 13$ TeV. 2019.

[180] Morad Aaboud et al. Search for low-mass resonances decaying into two jets and produced in association with a photon using pp collisions at $\sqrt{s} = 13$ TeV with the ATLAS detector. *Phys. Lett.*, B795:56–75, 2019.

[181] Search for a narrow resonance in high-mass dilepton final states in proton-proton collisions using 140 fb^{-1} of data at $\sqrt{s} = 13$ TeV. Technical Report CMS-PAS-EXO-19-019, CERN, Geneva, 2019.

[182] CMS collaboration. Search for a narrow resonance decaying to a pair of muons in proton-proton collisions at 13 TeV. Technical Report CMS-PAS-EXO-19-018, CERN, Geneva, 2019.

[183] Frank F. Deppisch, P. S. Bhupal Dev, and Apostolos Pilaftsis. Neutrinos and Collider Physics. *New J. Phys.*, 17(7):075019, 2015.

[184] D. de Florian et al. Handbook of LHC Higgs Cross Sections: 4. Deciphering the Nature of the Higgs Sector. 2016.

[185] Takanori Fujiwara, Taichiro Kugo, Haruhiko Terao, Shozo Uehara, and Koichi Yamawaki. Nonabelian Anomaly and Vector Mesons as Dynamical Gauge Bosons of Hidden Local Symmetries. *Prog. Theor. Phys.*, 73:926, 1985.

[186] Frank F. Deppisch, Suchita Kulkarni, and Wei Liu. Searching for a light Z through Higgs production at the LHC. *Phys. Rev.*, D100(11):115023, 2019.

[187] Alain Blondell, Panos Charitos, and Richard Jacobsson. Hunting for right-handed neutrinos: the new game in town | ep department newsletter, 2019.

[188] Anupama Atre, Tao Han, Silvia Pascoli, and Bin Zhang. The Search for Heavy Majorana Neutrinos. *JHEP*, 05:030, 2009.

[189] Patrick D. Bolton, Frank F. Deppisch, and P. S. Bhupal Dev. Neutrinoless double beta decay versus other probes of heavy sterile neutrinos. 2019.

[190] Lorenzo Basso. *Phenomenology of the minimal B-L extension of the Standard Model at the LHC*. PhD thesis, Southampton U., 2011.

[191] Jim Alexander et al. Dark Sectors 2016 Workshop: Community Report. 2016.

[192] Roel Aaij et al. Search for Dark Photons Produced in 13 TeV pp Collisions. *Phys. Rev. Lett.*, 120(6):061801, 2018.

[193] A. Anastasi et al. Limit on the production of a new vector boson in $\mathrm{e}^+\mathrm{e}^- \to \mathrm{U}\gamma$, $\mathrm{U} \to \pi^+\pi^-$ with the KLOE experiment. *Phys. Lett.*, B757:356–361, 2016.

[194] Roni Harnik, Joachim Kopp, and Pedro A. N. Machado. Exploring nu Signals in Dark Matter Detectors. *JCAP*, 1207:026, 2012.

[195] G. Bellini et al. Precision measurement of the 7Be solar neutrino interaction rate in Borexino. *Phys. Rev. Lett.*, 107:141302, 2011.

[196] M. Deniz et al. Measurement of Nu(e)-bar -Electron Scattering Cross-Section with a CsI(Tl) Scintillating Crystal Array at the Kuo-Sheng Nuclear Power Reactor. *Phys. Rev.*, D81:072001, 2010.

[197] Claudia Frugiuele, Elina Fuchs, Gilad Perez, and Matthias Schlaffer. Constraining New Physics Models with Isotope Shift Spectroscopy. *Phys. Rev.*, D96(1):015011, 2017.

[198] Eric D. Carlson. LIMITS ON A NEW U(1) COUPLING. *Nucl. Phys.*, B286:378–398, 1987.

[199] Bernard Aubert et al. The BaBar detector. *Nucl. Instrum. Meth.*, A479:1–116, 2002.

[200] J. P. Lees et al. Search for Invisible Decays of a Dark Photon Produced in e^+e^- Collisions at BaBar. *Phys. Rev. Lett.*, 119(13):131804, 2017.

[201] F. Bossi, E. De Lucia, J. Lee-Franzini, S. Miscetti, and M. Palutan. Precision Kaon and Hadron Physics with KLOE. *Riv. Nuovo Cim.*, 31:531–623, 2008.

[202] J. Abdallah et al. Photon events with missing energy in e+ e- collisions at $\mathrm{s}^{1/2}$ = 130-GeV to 209-GeV. *Eur. Phys. J.*, C38:395–411, 2005.

[203] J. Abdallah et al. Search for one large extra dimension with the DELPHI detector at LEP. *Eur. Phys. J.*, C60:17–23, 2009.

[204] Patrick J. Fox, Roni Harnik, Joachim Kopp, and Yuhsin Tsai. LEP Shines Light on Dark Matter. *Phys. Rev.*, D84:014028, 2011.

[205] Albert M Sirunyan et al. Search for an $L_\mu - L_\tau$ gauge boson using Z$\to 4\mu$ events in proton-proton collisions at $\sqrt{s} =$ 13 TeV. *Phys. Lett.*, B792:345–368, 2019.

[206] Albert M Sirunyan et al. A search for pair production of new light bosons decaying into muons in proton-proton collisions at 13 TeV. *Submitted to: Phys. Lett.*, 2018.

[207] Morad Aaboud et al. Search for Higgs boson decays to beyond-the-Standard-Model light bosons in four-lepton events with the ATLAS detector at $\sqrt{s} = 13$ TeV. *JHEP*, 06:166, 2018.

[208] Philip Bechtle, Sven Heinemeyer, Oscar Stål, Tim Stefaniak, and Georg Weiglein. *HiggsSignals*: Confronting arbitrary Higgs sectors with measurements at the Tevatron and the LHC. *Eur. Phys. J.*, C74(2):2711, 2014.

[209] Measurements of the Higgs boson production cross section via Vector Boson Fusion and associated WH production in the $WW^* \to \ell\nu\ell\nu$ decay mode with

the ATLAS detector at $\sqrt{s} = 13$ TeV. Technical Report ATLAS-CONF-2016-112, CERN, Geneva, Nov 2016.

[210] Study of the Higgs boson properties and search for high-mass scalar resonances in the $H \rightarrow ZZ^* \rightarrow 4\ell$ decay channel at $\sqrt{s} = 13$ TeV with the ATLAS detector. Technical Report ATLAS-CONF-2016-079, CERN, Geneva, Aug 2016.

[211] Search for the Standard Model Higgs boson produced in association with a vector boson and decaying to a $b\bar{b}$ pair in pp collisions at 13 TeV using the ATLAS detector. Technical Report ATLAS-CONF-2016-091, CERN, Geneva, Aug 2016.

[212] Search for the Standard Model Higgs boson produced in association with top quarks and decaying into $b\bar{b}$ in pp collisions at $\sqrt{s} = 13$ TeV with the ATLAS detector. Technical Report ATLAS-CONF-2016-080, CERN, Geneva, Aug 2016.

[213] Measurement of fiducial, differential and production cross sections in the $H \rightarrow \gamma\gamma$ decay channel with 13.3 fb^{-1} of 13 TeV proton-proton collision data with the ATLAS detector. Technical Report ATLAS-CONF-2016-067, CERN, Geneva, Aug 2016.

[214] Search for the Associated Production of a Higgs Boson and a Top Quark Pair in Multilepton Final States with the ATLAS Detector. Technical Report ATLAS-CONF-2016-058, CERN, Geneva, Aug 2016.

[215] Albert M Sirunyan et al. Measurements of properties of the Higgs boson decaying into the four-lepton final state in pp collisions at $\sqrt{s} = 13$ TeV. *JHEP*, 11:047, 2017.

[216] Updated measurements of Higgs boson production in the diphoton decay channel at $\sqrt{s} = 13$ TeV in pp collisions at CMS. Technical Report CMS-PAS-HIG-16-020, CERN, Geneva, 2016.

[217] Philip Bechtle, Oliver Brein, Sven Heinemeyer, Oscar Stål, Tim Stefaniak, Georg Weiglein, and Karina E. Williams. HiggsBounds − 4: Improved Tests of Extended Higgs Sectors against Exclusion Bounds from LEP, the Tevatron and the LHC. *Eur. Phys. J.*, C74(3):2693, 2014.

[218] Guido Altarelli and Riccardo Barbieri. Vacuum polarization effects of new physics on electroweak processes. *Phys. Lett.*, B253:161–167, 1991.

[219] D. C. Kennedy, B. W. Lynn, C. J. C. Im, and R. G. Stuart. Electroweak Cross-Sections and Asymmetries at the Z0. *Nucl. Phys.*, B321:83–107, 1989.

[220] M. Kuroda, G. Moultaka, and D. Schildknecht. Direct one loop renormalization of SU(2)-L x U(1)-Y four fermion processes and running coupling constants. *Nucl. Phys.*, B350:25–72, 1991.

[221] Michael E. Peskin and Tatsu Takeuchi. Estimation of oblique electroweak corrections. *Phys. Rev.*, D46:381–409, 1992.

[222] I. Maksymyk, C. P. Burgess, and David London. Beyond S, T and U. *Phys. Rev.*, D50:529–535, 1994.

[223] Michael E. Peskin and Tatsu Takeuchi. A New constraint on a strongly interacting Higgs sector. *Phys. Rev. Lett.*, 65:964–967, 1990.

[224] Roel Aaij et al. Search for Higgs-like bosons decaying into long-lived exotic particles. *Eur. Phys. J.*, C76(12):664, 2016.

[225] M. Cepeda et al. Report from Working Group 2. *CERN Yellow Rep. Monogr.*, 7:221–584, 2019.

[226] Mingyi Dong and Gang Li. CEPC Conceptual Design Report: Volume 2 - Physics & Detector. 2018.

[227] Jiayin Gu, Honglei Li, Zhen Liu, Shufang Su, and Wei Su. Learning from Higgs Physics at Future Higgs Factories. *JHEP*, 12:153, 2017.

[228] O. Adriani et al. Search for isosinglet neutral heavy leptons in Z0 decays. *Phys. Lett.*, B295:371–382, 1992.

[229] P. Abreu et al. Search for neutral heavy leptons produced in Z decays. *Z. Phys.*, C74:57–71, 1997. [Erratum: Z. Phys.C75,580(1997)].

[230] Alain Blondel, E. Graverini, N. Serra, and M. Shaposhnikov. Search for Heavy Right Handed Neutrinos at the FCC-ee. *Nucl. Part. Phys. Proc.*, 273-275:1883–1890, 2016.

[231] A. Abada, V. De Romeri, S. Monteil, J. Orloff, and A. M. Teixeira. Indirect searches for sterile neutrinos at a high-luminosity Z-factory. *JHEP*, 04:051, 2015.

[232] A. Abulencia et al. Inclusive Search for New Physics with Like-Sign Dilepton Events in $p\bar{p}$ Collisions at $\sqrt{s}$ = 1.96-TeV. *Phys. Rev. Lett.*, 98:221803, 2007.

[233] Enrico Nardi, Esteban Roulet, and Daniele Tommasini. Limits on neutrino mixing with new heavy particles. *Phys. Lett.*, B327:319–326, 1994.

[234] Enrico Nardi, Esteban Roulet, and Daniele Tommasini. New neutral gauge bosons and new heavy fermions in the light of the new LEP data. *Phys. Lett.*, B344:225–232, 1995.

[235] Sven Bergmann and Alex Kagan. Z - induced FCNCs and their effects on neutrino oscillations. *Nucl. Phys.*, B538:368–386, 1999.

[236] S. Antusch, C. Biggio, E. Fernandez-Martinez, M. B. Gavela, and J. Lopez-Pavon. Unitarity of the Leptonic Mixing Matrix. *JHEP*, 10:084, 2006.

[237] A. Abada, C. Biggio, F. Bonnet, M. B. Gavela, and T. Hambye. Low energy effects of neutrino masses. *JHEP*, 12:061, 2007.

[238] Stefan Antusch and Oliver Fischer. Non-unitarity of the leptonic mixing matrix: Present bounds and future sensitivities. *JHEP*, 10:094, 2014.

[239] A. Abada, D. Das, A. M. Teixeira, A. Vicente, and C. Weiland. Tree-level lepton universality violation in the presence of sterile neutrinos: impact for R_K and R_π. *JHEP*, 02:048, 2013.

[240] A. Abada, A. M. Teixeira, A. Vicente, and C. Weiland. Sterile neutrinos in leptonic and semileptonic decays. *JHEP*, 02:091, 2014.

[241] Takehiko Asaka, Shintaro Eijima, and Kazuhiro Takeda. Lepton Universality in the νMSM. *Phys. Lett.*, B742:303–309, 2015.

[242] R. E. Shrock. New Tests For, and Bounds On, Neutrino Masses and Lepton Mixing. *Phys. Lett.*, 96B:159–164, 1980.

[243] Robert E. Shrock. General Theory of Weak Leptonic and Semileptonic Decays. 1. Leptonic Pseudoscalar Meson Decays, with Associated Tests For, and Bounds on, Neutrino Masses and Lepton Mixing. *Phys. Rev.*, D24:1232, 1981.

[244] Louis Lello and Daniel Boyanovsky. Searching for sterile neutrinos from π and K decays. *Phys. Rev.*, D87:073017, 2013.

[245] D. Liventsev et al. Search for heavy neutrinos at Belle. *Phys. Rev.*, D87(7):071102, 2013. [Erratum: Phys. Rev.D95,no.9,099903(2017)].

[246] K. A. Olive et al. Review of Particle Physics. *Chin. Phys.*, C38:090001, 2014.

[247] G. Bernardi et al. FURTHER LIMITS ON HEAVY NEUTRINO COUPLINGS. *Phys. Lett.*, B203:332–334, 1988.

[248] J. Badier et al. Direct Photon Production From Pions and Protons at 200-GeV/*c*. *Z. Phys.*, C31:341, 1986.

[249] F. Bergsma et al. A Search for Decays of Heavy Neutrinos in the Mass Range 0.5-GeV to 2.8-GeV. *Phys. Lett.*, 166B:473–478, 1986.

[250] P. Vilain et al. Search for heavy isosinglet neutrinos. *Phys. Lett.*, B343:453–458, 1995. [Phys. Lett.B351,387(1995)].

[251] J. Orloff, Alexandre N. Rozanov, and C. Santoni. Limits on the mixing of tau neutrino to heavy neutrinos. *Phys. Lett.*, B550:8–15, 2002.

[252] S. A. Baranov et al. Search for heavy neutrinos at the IHEP-JINR neutrino detector. *Phys. Lett.*, B302:336–340, 1993.

[253] Amanda M. Cooper-Sarkar et al. Search for Heavy Neutrino Decays in the BEBC Beam Dump Experiment. *Phys. Lett.*, 160B:207–211, 1985.

[254] E. Gallas et al. Search for neutral weakly interacting massive particles in the Fermilab Tevatron wide band neutrino beam. *Phys. Rev.*, D52:6–14, 1995.

[255] A. Vaitaitis et al. Search for neutral heavy leptons in a high-energy neutrino beam. *Phys. Rev. Lett.*, 83:4943–4946, 1999.

[256] P. Astier et al. Search for heavy neutrinos mixing with tau neutrinos. *Phys. Lett.*, B506:27–38, 2001.

[257] R. Acciarri et al. Long-Baseline Neutrino Facility (LBNF) and Deep Underground Neutrino Experiment (DUNE). 2015.

[258] M. Anelli et al. A facility to Search for Hidden Particles (SHiP) at the CERN SPS. 2015.

[259] M. Daum, B. Jost, R. M. Marshall, R. C. Minehart, W. A. Stephens, and K. O. H. Ziock. Search for Admixtures of Massive Neutrinos in the Decay $\pi^+ \to \mu^+$ Neutrino. *Phys. Rev.*, D36:2624, 1987.

[260] A. Aguilar-Arevalo et al. Search for heavy neutrinos in $\pi \to \mu\nu$ decay. *Phys. Lett.*, B798:134980, 2019.

[261] R. S. Hayano et al. HEAVY NEUTRINO SEARCH USING K(mu2) DECAY. *Phys. Rev. Lett.*, 49:1305, 1982.

[262] T. Yamazaki et al. Search for Heavy Neutrinos in Kaon Decay. page I.262, 1984. [Conf. Proc.C840719,262(1984)].

[263] Robert E. Shrock. General Theory of Weak Processes Involving Neutrinos. 2. Pure Leptonic Decays. *Phys. Rev.*, D24:1275, 1981.

[264] Pilar Coloma, Pilar Hernández, Víctor Muñoz, and Ian M. Shoemaker. New constraints on Heavy Neutral Leptons from Super-Kamiokande data. 2019.

[265] A. V. Artamonov et al. Search for heavy neutrinos in $K^+ \to \mu^+ \nu_H$ decays. *Phys. Rev.*, D91(5):052001, 2015. [Erratum: Phys. Rev.D91,no.5,059903(2015)].

[266] C. Lazzeroni and E. Goudzovski. Talks at Kaon-2019. 2019.

[267] K. Abe et al. Search for heavy neutrinos with the T2K near detector ND280. *Phys. Rev.*, D100(5):052006, 2019.

[268] P. Abratenko et al. Search for heavy neutral leptons decaying into muon-pion pairs in the MicroBooNE detector. 2019.

[269] M. G. Aartsen et al. Searches for Sterile Neutrinos with the IceCube Detector. *Phys. Rev. Lett.*, 117(7):071801, 2016.

[270] M. G. Aartsen et al. Search for sterile neutrino mixing using three years of IceCube DeepCore data. *Phys. Rev.*, D95(11):112002, 2017.

[271] P. Adamson et al. Search for sterile neutrinos in MINOS and MINOS+ using a two-detector fit. *Phys. Rev. Lett.*, 122(9):091803, 2019.

[272] K. Abe et al. Limits on sterile neutrino mixing using atmospheric neutrinos in Super-Kamiokande. *Phys. Rev.*, D91:052019, 2015.

[273] P. Adamson et al. Search for active-sterile neutrino mixing using neutral-current interactions in NOvA. *Phys. Rev.*, D96(7):072006, 2017.

[274] F. Dydak et al. A Search for Muon-neutrino Oscillations in the Delta m^2 Range 0.3-eV^2 to 90-eV^2. *Phys. Lett.*, 134B:281, 1984.

[275] I. E. Stockdale et al. Limits on Muon Neutrino Oscillations in the Mass Range 55-eV^2 < Delta m^2 < 800-eV^2. *Phys. Rev. Lett.*, 52:1384, 1984.

[276] Carlos A. Argüelles, Vedran Brdar, and Joachim Kopp. Production of keV Sterile Neutrinos in Supernovae: New Constraints and Gamma Ray Observables. *Phys. Rev.*, D99(4):043012, 2019.

[277] Kenny C. Y. Ng, Brandon M. Roach, Kerstin Perez, John F. Beacom, Shunsaku Horiuchi, Roman Krivonos, and Daniel R. Wik. New Constraints on Sterile Neutrino Dark Matter from *NuSTAR* M31 Observations. *Phys. Rev.*, D99:083005, 2019.

[278] Brandon M. Roach, Kenny C. Y. Ng, Kerstin Perez, John F. Beacom, Shunsaku Horiuchi, Roman Krivonos, and Daniel R. Wik. NuSTAR Tests of Sterile-Neutrino Dark Matter: New Galactic Bulge Observations and Combined Impact. 2019.

[279] Elena Accomando, Diego Becciolini, Alexander Belyaev, Stefano Moretti, and Claire Shepherd-Themistocleous. Z' at the LHC: Interference and Finite Width Effects in Drell-Yan. *JHEP*, 10:153, 2013.

[280] Andy Buckley, Jonathan Butterworth, Leif Lonnblad, David Grellscheid, Hendrik Hoeth, James Monk, Holger Schulz, and Frank Siegert. Rivet user manual. *Comput. Phys. Commun.*, 184:2803–2819, 2013.

[281] Glen Cowan, Kyle Cranmer, Eilam Gross, and Ofer Vitells. Asymptotic formulae for likelihood-based tests of new physics. *Eur. Phys. J.*, C71:1554, 2011. [Erratum: Eur. Phys. J.C73,2501(2013)].

[282] Alexander L. Read. Presentation of search results: The CL(s) technique. *J. Phys.*, G28:2693–2704, 2002. [,11(2002)].

[283] Georges Aad et al. Measurement of the low-mass Drell-Yan differential cross section at $\sqrt{s}$ = 7 TeV using the ATLAS detector. *JHEP*, 06:112, 2014.

[284] Georges Aad et al. Measurement of the transverse momentum and ϕ^*_η distributions of Drell-Yan lepton pairs in proton-proton collisions at $\sqrt{s} = 8$ TeV with the ATLAS detector. *Eur. Phys. J.*, C76(5):291, 2016.

[285] Georges Aad et al. Measurement of the double-differential high-mass Drell-Yan cross section in pp collisions at $\sqrt{s} = 8$ TeV with the ATLAS detector. *JHEP*, 08:009, 2016.

[286] Morad Aaboud et al. Search for triboson $W^{\pm}W^{\pm}W^{\mp}$ production in pp collisions at $\sqrt{s} = 8$ TeV with the ATLAS detector. *Eur. Phys. J.*, C77(3):141, 2017.

[287] Vardan Khachatryan et al. Measurements of jet multiplicity and differential production cross sections of $Z+$ jets events in proton-proton collisions at $\sqrt{s} = 7$ TeV. *Phys. Rev.*, D91(5):052008, 2015.

[288] Georges Aad et al. Measurement of ZZ production in pp collisions at $\sqrt{s} = 7$ TeV and limits on anomalous ZZZ and $ZZ\gamma$ couplings with the ATLAS detector. *JHEP*, 03:128, 2013.

[289] Morad Aaboud et al. $ZZ \to \ell^+\ell^-\ell'^+\ell'^-$ cross-section measurements and search for anomalous triple gauge couplings in 13 TeV pp collisions with the ATLAS detector. *Phys. Rev.*, D97(3):032005, 2018.

[290] Georges Aad et al. Fiducial and differential cross sections of Higgs boson production measured in the four-lepton decay channel in pp collisions at $\sqrt{s}$=8 TeV with the ATLAS detector. *Phys. Lett.*, B738:234–253, 2014.

[291] Georges Aad et al. Measurements of four-lepton production in pp collisions at $\sqrt{s} = 8$ TeV with the ATLAS detector. *Phys. Lett.*, B753:552–572, 2016.

[292] Georges Aad et al. Measurements of $Z\gamma$ and $Z\gamma\gamma$ production in pp collisions at $\sqrt{s} = 8$ TeV with the ATLAS detector. *Phys. Rev.*, D93(11):112002, 2016.

[293] Georges Aad et al. Measurement of the electroweak production of dijets in association with a Z-boson and distributions sensitive to vector boson fusion

in proton-proton collisions at $\sqrt{s} = 8$ TeV using the ATLAS detector. *JHEP*, 04:031, 2014.

[294] Morad Aaboud et al. Measurement of the k_{t} splitting scales in $Z \to \ell\ell$ events in pp collisions at $\sqrt{s} = 8$ TeV with the ATLAS detector. *JHEP*, 08:026, 2017.

[295] Georges Aad et al. Measurement of total and differential W^+W^- production cross sections in proton-proton collisions at $\sqrt{s} = 8$ TeV with the ATLAS detector and limits on anomalous triple-gauge-boson couplings. *JHEP*, 09:029, 2016.

[296] V. Khachatryan et al. Measurements of the associated production of a Z boson and b jets in pp collisions at $\sqrt{s} = 8\,\mathrm{TeV}$. *Eur. Phys. J.*, C77(11):751, 2017.

[297] Roel Aaij et al. Study of forward Z + jet production in pp collisions at $\sqrt{s} = 7$ TeV. *JHEP*, 01:033, 2014.

[298] Torbjörn Sjöstrand, Stefan Ask, Jesper R. Christiansen, Richard Corke, Nishita Desai, Philip Ilten, Stephen Mrenna, Stefan Prestel, Christine O. Rasmussen, and Peter Z. Skands. An Introduction to PYTHIA 8.2. *Comput. Phys. Commun.*, 191:159–177, 2015.

[299] F. Meloni. Track and vertex reconstruction in the ATLAS experiment. *Nucl. Instrum. Meth.*, A718:334–335, 2013.

[300] Javier Duarte. Fast Reconstruction and Data Scouting. In *4th International Workshop Connecting The Dots 2018 (CTD2018) Seattle, Washington, USA, March 20-22, 2018*, 2018.

[301] Roel Aaij et al. Search for massive long-lived particles decaying semileptonically in the LHCb detector. *Eur. Phys. J.*, C77(4):224, 2017.

[302] John Paul Chou, David Curtin, and H. J. Lubatti. New Detectors to Explore the Lifetime Frontier. *Phys. Lett.*, B767:29–36, 2017.

[303] Akitaka Ariga et al. FASER's physics reach for long-lived particles. *Phys. Rev.*, D99(9):095011, 2019.

[304] Henso Abreu et al. Detecting and Studying High-Energy Collider Neutrinos with FASER at the LHC. 2019.

[305] James Lewis Pinfold. The MoEDAL Experiment at the LHC—A Progress Report. *Universe*, 5(2):47, 2019.

[306] Vladimir V. Gligorov, Simon Knapen, Michele Papucci, and Dean J. Robinson. Searching for Long-lived Particles: A Compact Detector for Exotics at LHCb. *Phys. Rev.*, D97(1):015023, 2018.

[307] Halina Abramowicz et al. The International Linear Collider Technical Design Report - Volume 4: Detectors. 2013.

[308] H. Aihara, P. Burrows, M. Oreglia, E. L. Berger, V. Guarino, J. Repond, H. Weerts, L. Xia, J. Zhang, Q. Zhang, et al. SiD Letter of Intent. 2009.

[309] Muhammd Ahmad et al. CEPC-SPPC Preliminary Conceptual Design Report. 1. Physics and Detector. 2015.

[310] Eder Izaguirre and Brian Shuve. Multilepton and Lepton Jet Probes of Sub-Weak-Scale Right-Handed Neutrinos. *Phys. Rev.*, D91(9):093010, 2015.

[311] Georges Aad et al. Search for long-lived, heavy particles in final states with a muon and multi-track displaced vertex in proton-proton collisions at $\sqrt{s} = 7$ TeV with the ATLAS detector. *Phys. Lett.*, B719:280–298, 2013.

[312] David Curtin et al. Long-Lived Particles at the Energy Frontier: The MATHUSLA Physics Case. 2018.

[313] Cristiano Alpigiani et al. A Letter of Intent for MATHUSLA: A Dedicated Displaced Vertex Detector above ATLAS or CMS. 2018.

[314] James Lewis Pinfold (private communication).

[315] Michael Staelens. Recent Results and Future Plans of the MoEDAL Experiment. In *Meeting of the Division of Particles and Fields of the American Physical Society (DPF2019) Boston, Massachusetts, July 29-August 2, 2019*, 2019.

[316] Asher Berlin and Felix Kling. Inelastic Dark Matter at the LHC Lifetime Frontier: ATLAS, CMS, LHCb, CODEX-b, FASER, and MATHUSLA. *Phys. Rev.*, D99(1):015021, 2019.

[317] A. D. Martin, W. J. Stirling, R. S. Thorne, and G. Watt. Parton distributions for the LHC. *Eur. Phys. J.*, C63:189–285, 2009.

[318] M. A. Luty. Baryogenesis via leptogenesis. *Phys. Rev.*, D45:455–465, 1992.

[319] Eamonn Maguire, Lukas Heinrich, and Graeme Watt. HEPData: a repository for high energy physics data. *J. Phys. Conf. Ser.*, 898(10):102006, 2017.

[320] Morad Aaboud et al. Search for dark matter and other new phenomena in events with an energetic jet and large missing transverse momentum using the ATLAS detector. *JHEP*, 01:126, 2018.

[321] T. Abe et al. Belle II Technical Design Report. 2010.

[322] W. Altmannshofer et al. The Belle II Physics Book. 2018.

[323] Luigi Delle Rose, Shaaban Khalil, Simon J. D. King, Suchita Kulkarni, Carlo Marzo, Stefano Moretti, and Cem S. Un. Sneutrino Dark Matter in the BLSSM. *JHEP*, 07:100, 2018.

[324] Luigi Delle Rose, Shaaban Khalil, Simon J. D. King, Carlo Marzo, Stefano Moretti, and Cem S. Un. Supersymmetric Gauged B-L Model of Dark Matter and Fine Tuning. *PoS*, EPS-HEP2017:067, 2017.

[325] Luigi Delle Rose, Shaaban Khalil, Simon J. D. King, Carlo Marzo, Stefano Moretti, and Cem S. Un. Naturalness and Dark Matter Properties of the BLSSM. *PoS*, DIS2017:301, 2018.

[326] Luigi Delle Rose, Shaaban Khalil, Simon J. D. King, Carlo Marzo, Stefano Moretti, and Cem S. Un. Naturalness and dark matter in the supersymmetric B-L extension of the standard model. *Phys. Rev.*, D96(5):055004, 2017.

[327] Luigi Delle Rose, Shaaban Khalil, Simon J. D. King, Suchita Kulkarni, Carlo Marzo, Stefano Moretti, and Cem S. Un. Prospects for Sneutrino Dark Matter in the BLSSM. In *32nd Rencontres de Physique de La Vall'Aoste (La Thuile 2018) La Thuile, Aosta, Italy, February 25-March 3, 2018*, 2018.